Measurements of Identified Hadrons in p+Au Collisions at 200 GeV

By

Weizhuang Peng

Dissertation

Submitted to the Faculty of the

Graduate School of Vanderbilt University

in partial fulfillment of the requirements

for the degree of

DOCTOR OF PHILOSOPHY

in

Physics and Astronomy

December 12, 2020

Nashville, Tennessee

Approved:
Julia Velkovska, Ph.D.
Senta Greene, Ph.D.
William Holmes, Ph.D.
Paul Sheldon, Ph.D.

To my beloved parents,

Yu Peng and Cuijuan Ma.

And all my dear friends.

Acknowledgment

This dissertation would not be possible without the help of many people.

First and foremost, I would like to express my deepest gratitude to my advisor, Dr. Julia Velkovska, for her guidance, mentorship and support over the years. Besides the help that she provided for my research, I also learned lots of other useful things form her such as how to make a good presentation. I would also like to thank the members of my committee, Dr. Vicki Green, Dr. Paul Sheldon and Dr. William Holmes.

I am also very grateful for the help provided by my colleagues at Vanderbilt University: Dr. Qiao Xu, Dr. Shengli Huang, Dr. Shengquan Tuo, Dr. Hong Ni, and Dr. Sourav Tarafdar. Dr. Qiao Xu lead me step by step into the analysis part during the first and second year of my graduate program. Ohter colleagues also helped me a lot during my research and answered many questions related to research and programming.

I also received a lot of help from a lot of senior people form the PHENIX Collaboration, such as Dr. Ron Blemont, Dr. Javier Orjuela-Koop and so on.

Besides the people who help me in my research, I would also like to thanks to all my friends who helped me in the daily life and who encouraged me while I am upset.

TABLE OF CONTENTS

LIST OF TABLES

LIST OF FIGURES

Chapter 1

Introduction

1.1 Standard Model and Quantum Chromodynamics

The Standard Model of particle physics is the theory that describes three of the four known fundamental forces: the electromagnetic force, the weak, and the strong interaction, excluding the gravitational force. There are 17 named particles in Standard Model. These particles are either building blocks of matter, called fermions, or mediators of the interactions, called bosons. These particles are shown in Fig. 1.1. Fermions have half-integer spin and follow the Pauli exclusion principle, that is no two particle can occupy the same quantum state at the same time; bosons have integer spins and do not have this restriction. There are six types of quarks (up, down, charm, strange, top and bottom), which can not exist independently in nature, and six types of leptons (electron, muon, tau and their corresponding neutrinos). The word "quark" originally appeared in the novel "Finnegans Wake" written by the Irish author James Joyce (1882–1941), where a drunken seagull asks for "three quarks for Muster Mark" [17]. Quarks and anti-quarks can form bound states called mesons, and triplets of quarks can bind to make baryons. Collectively, baryons and mesons are called hadrons, and these are the particles that participate in the strong interaction. One striking thing though is that the two or three valance quarks only account for a small fraction of the total mass of the hadrons. The vast majority of the mass comes from the quantum fluctuations of quark anti-quark pairs, the gluons, and the energy associated with quarks moving around at close to the speed of light [2]. A detailed understanding of these phenomena is stills to be discovered.

Chen Ning Yang and Robert Mills first proposed the idea of non-abelian groups to explain the strong interaction in 1954 [18]. Then in 1961, Sheldon Weinberg combined the electromagnetic and weak interactions into electroweak interaction [19]. The modern form of the standard model was formed when Steven Weinberg and Abdus Salam introduced the Higgs mechanism into the

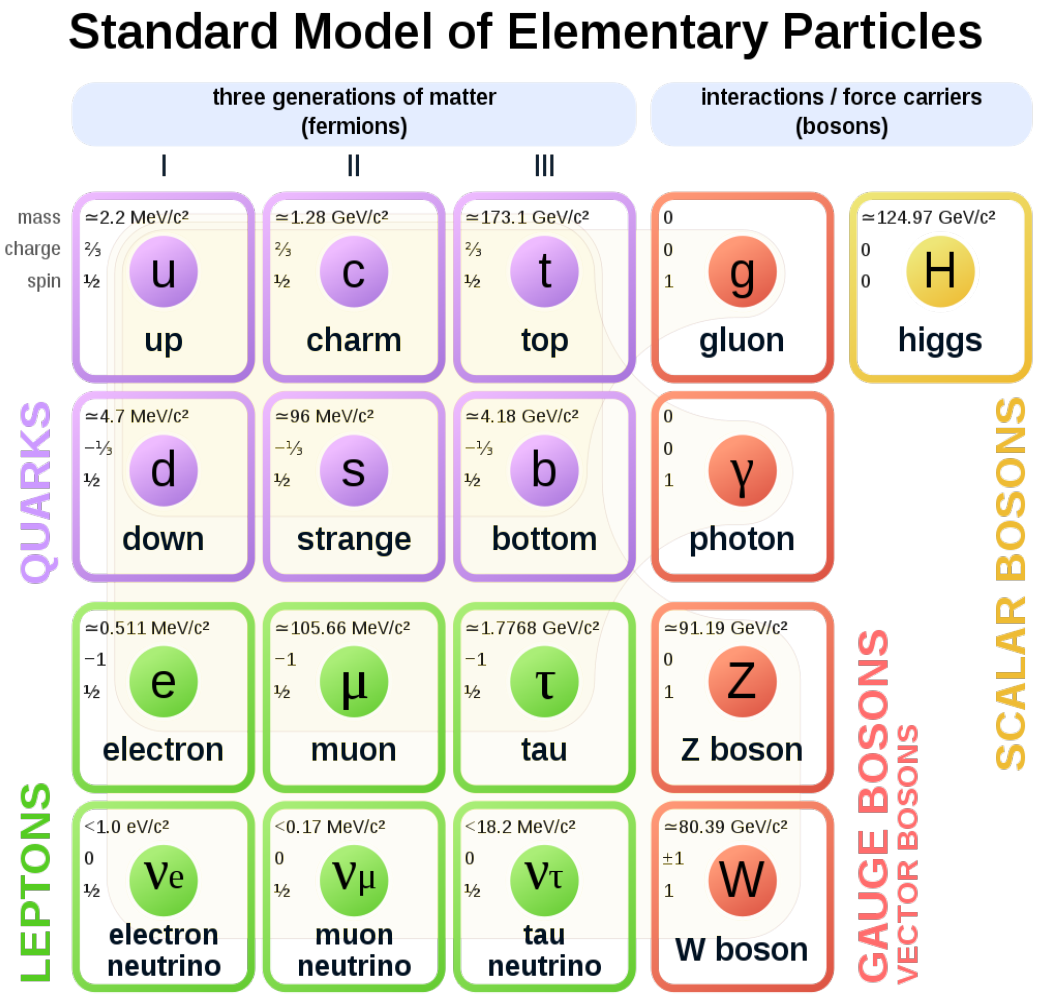

Figure 1.1: Standard Model of Fundamental Particles [1].

electroweak interaction in 1967 [20].

Quantum Chromodynamics (QCD) is the fundamental theory describing the strong interaction between quarks and gluons. QCD is a type of quantum field theory called a non-abelian gauge theory, with symmetry group SU(3). In comparison to the electromagnetic force, color is analogous to the electric charge, and gluons are the force carriers, similar to photons. One big difference between photons and gluons is that the photons interact with particles that carry charge, but they do not carry charges themselves, while the gluons carry color. So, the gluons can interact with gluons and this has great consequences. The two main properties of QCD are color confinement and asymptotic freedom. In QCD, there are three colors, and color confinement states that color-charged particles can not exist in isolation. All hadrons are "white" or color-neutral. The quarks are confined in hadrons. If we try to separate two quarks, the energy needed to move them away from each other increases with the distance between them, and when the energy is large enough it will be advantageous to create a new quark and anti-quark pair. Thus, no single quark of anti-quark can be observed. Even though color confinement has never been proven analytically, it has been shown in various experiments and in lattice QCD calculations. Asymptotic freedom refers to the fact that the strength of interaction between quarks and gluons decreases with increasing energy or decreasing distance, which is contrary to the electromagnetic force and gravity. At large energies when the quarks and gluons scatter off each other with large momentum transfer in processes called hard-scattering, the coupling between them is small making them almost "free". When the coupling is small, the process can be described with perturbative QCD. However, most of the quark-gluon interactions involve small momentum transfer and then the coupling in large; it is this property that keeps the quarks confined into hadrons. In 1973, the asymptotic freedom of QCD was discovered independently by David Gross, Frank Wilczek and David Politzer. They shared the Physics Nobel Prize in 2004.

The quarks and gluons can be de-confined at high temperature, as the hadrons are melted into a quark-gluon plasma (QGP). Figure 1.2 [2, 21] shows our current understanding of the phase diagram of QCD as a function of temperature and baryon chemical potential, which is a measure

of the excess of quarks over anti-quarks. QGP occupies the top part of the diagram, where the temperature is high. QGP is thought to have existed in the first few microseconds after the Big Bang; as the Universe expanded and cooled, the quarks and gluons are confined into protons and neutrons. The red dots in the diagram indicate the temperature, T, and baryon chemical potential, μ_B, inferred from measurements of the abundances of hadrons of different types produced in high-energy heavy ion collisions. The yellow band gives an estimate of these quantities from the comparison of data and thermal models of particle production at high energies. According to lattice-QCD calculation, in the case of no doping ($\mu_B = 0$), when the QGP cools the transition is a rapid and smooth crossover; however, as the doping increases, the transition maybe become a sharp first-order phase transition. There is a line of first-order phase transitions, which ends at a critical point, which is a second-order phase transition with co-existing bubbles of QGP and bubbles of hadrons [2]. Performing lattice QCD calculations is difficult at finite μ_B, so the location of the critical point and if it exists is hard to predict theoretically. This is something for the experiment to discover, and this is where relativistic heavy ion collisions come into play.

We can explore the QCD phase diagram if we accelerate heavy nuclei up to about the 99% of the speed of light and collide them head on. Then we can create some matter which temperate is greater than the critical temperature of about 150 MeV, so that the protons and neutrons will melt into quarks and gluons. The QGP formation has been proven by many experimental results from RHIC and LHC. At the highest RHIC energy and at LHC energy, the matter created at mid-rapidity has almost equal amount of matter and anti-matter, as shown in the white line in Fig. 1.2. But this is a tiny part of the QCD phase diagram, to explore more regions of the phase diagram, we need to increase the baryon doping, which means to make the matter produced with more quarks than anti-quarks. One way to achieve this is to lower the energy of the collisions. RHIC is presently conducting a beam energy scan aimed at the discovery of a critical point in the QCD phase diagram.

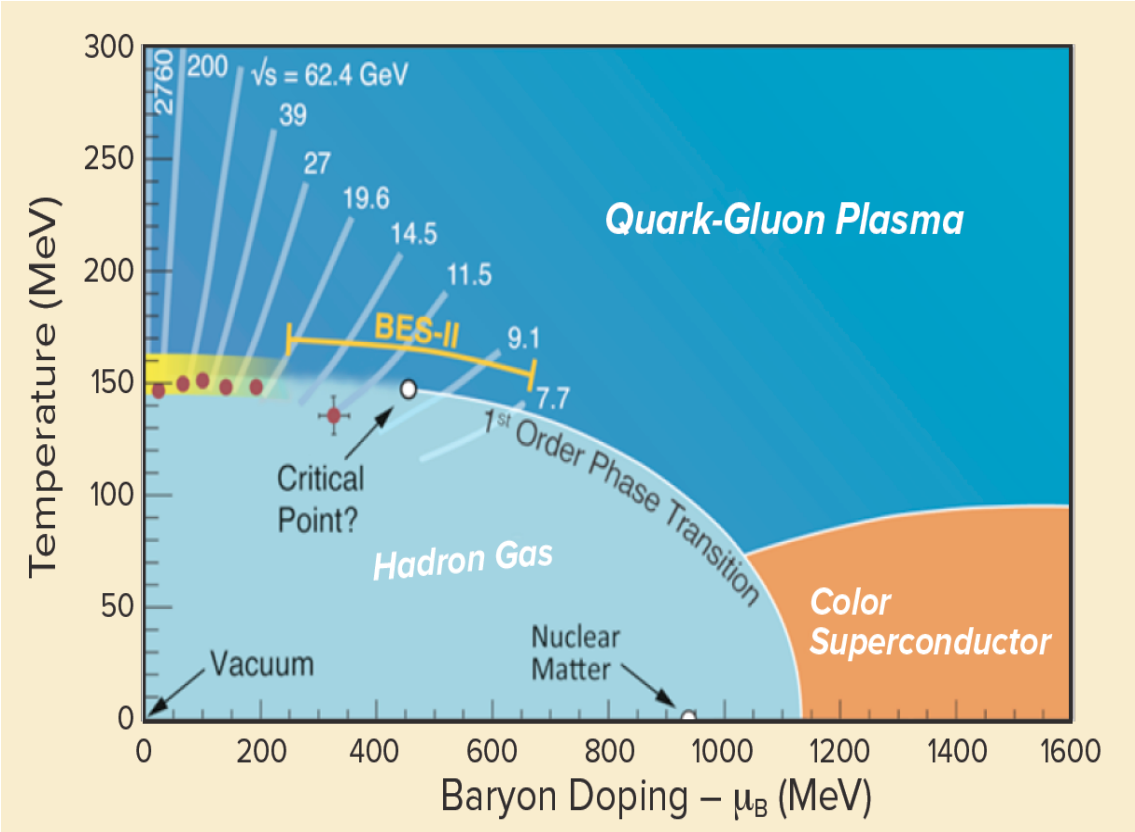

Figure 1.2: The phase diagram of QCD as a function of temperature and baryon doping, a measure of the excess of quarks over anti-quarks [2].

1.2 Heavy Ion Collisions

As mentioned above, relativistic heavy ion collisions is a good way to explore the QCD phase diagram. Currently, there are two main large colliders in the world. One is the Large Hadron Collider (LHC), located in France and Switzerland. The other one is the Relativistic Heavy Ion Collider (RHIC), located on Long Island, New York. The collision energy of RHIC can be up to 200 GeV per nucleon in the center-of-mass, and the highest energy for Pb+Pb collisions at the LHC is 5.5 TeV per nucleon in the center-of-mass, an orer of magnitude higher than that for RHIC. However, RHIC has the advantage of more versatile choices of nuclei. RHIC is able to collide lots of different systems, from proton-proton collision, to proton-gold collision, deuteron-gold, ^{3}He-gold, copper-gold, and gold-gold collisions. The versatility of RHIC has made it possible to engineer the shape and size of the QGP droplets produced in the collisions [22].

According to lattice-QCD calculations [23], the energy density needed to form QGP is around 1 GeV/fm^3; based on experimental data [24] the energy density reached in he most central Au+Au collisions at RHIC around 15 GeV/fm^3, which is much higher than the critical energy density, so we expect that the quarks and gluons are deconfined and QGP is formed in heavy ion collisions at RHIC. It is less well established if QGO can also be formed in small systems, such as high energy proton-gold (pAu) collisions, or if nuclear matter remains "cold" despite of the high energy.

Figure 1.3 [3] shows the time evolution of a relativistic heavy ion collision. Before the collision, the two nuclei are accelerated to almost the speed of light, so in the longitudinal direction the nuclei seems contracted. The contraction factors are around 100 and 2500 at highest RHIC and LHC energies [21]. When the two thin discs collide, they will form a very dense and high temperature state of matter, and if the temperature is above the critical temperature T_c, QGP will be formed. It has been shown that this new state of matter acts like fluid with very low specific viscosity [25]. Then, the QGP expands and flows like a fluid, until the temperature drops under T_c, when hadrons are formed. The hadrons will still interact with each other inelastically and may change identity until the temperature drops under a temperature called chemical freeze-out temperature T_{ch}, so this process is called chemical freeze out. After that, the hadrons may still

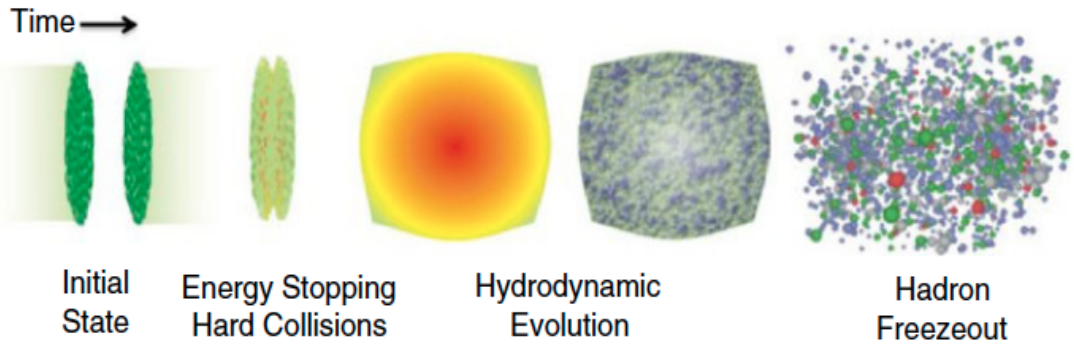

Figure 1.3: The time evolution of a relativistic heavy ion collision [3].

interact with each other elastically and change momentum until the temperature drops under the kinetic freeze out temperature T_k. After all interactions cease, the hadrons will fly freely into the detectors. The distribution of these hadrons in phase space will reflect the evolution of the system from its initial state when the energy density is formed, through the QGP formation, expansion, hadronization, and the interactions in the hadron gas.

1.3 Signatures of Quark Gluon Plasma

In the last section, we discussed that relativistic heavy ion collisions can form QGP, but how can we make sure that QGP is really formed? After so many years of study, many observables have been shown to indicate the formation of a new state of matter, most likely - QGP. Such signatures include jet quenching, collective flow, and quarkonium suppression.

1.3.1 Jet Quenching

In the earliest time of the collision, some partons will scatter off each other with very large momentum transfer. This is likely to happen before the formation of QGP. The partons will move through the deconfined medium, interact and lose energy. Then they will form jets of hadrons, but these hadrons will appear with smaller momenta compared to the case when no medium is formed. One way to measure this is through the variable nuclear modification factor, R_{AA}. It is defined as follows:

$$R_{AA}(p_T) = \frac{(1/N_{evt})d^2N^{A+A}/dp_T dy}{(< N_{binary} > /\sigma_{inel}^{N+N})d^2\sigma^{N+N}/dp_T dy} \tag{1.1}$$

Where N_{binary} is the number of binary nucleon-nucleon collisions in a nucleus-nucleus collision. This variable will show how the spectra of the hadrons produced in a nucleus-nucleus collision are modified in comparison to those produced in a a simple nucleon-nucleon collision, which is not expected to produce QGP. If no nuclear modification happens, we will expect R_{AA} to be unity; if it diverges from unity, we will know that the nucleus-nucleus collision is not a simple superposition of proton-proton collisions.

Figure 1.4 [4] shows the first measurement of PHENIX of R_{AA} in Au+Au collisions at $\sqrt{s_{NN}}$ = 130 GeV. We can see the R_{AA} of both the charged hadrons and the neutral pions are below unity, which means they suffer a large suppression compared to the baseline case. This can be attributed to energy loss that the partons experience in the medium produced in the collisions before forming the jet of hadrons.

1.3.2 Collective Flow

In off-center collisions, the initial geometry of the overlap zone of the two nuclei is not azimuthally symmetric. If QGP is formed, this initial spatial anisotropy will generate pressure gradients, and this will result in azimuthally anisotropic collective flow of this matter. In the radial direction, the fluid will expand with a common velocity. If all particle originate from the fluid and move with a common velocity, then in the end the heavier hadrons will appear at higher momentum. In addition, if hadrons are formed by recombination of quarks that have a thermal distribution, then the baryons and mesons will have different behaviour since mesons have two quark and hadrons have three quark and they will appear at different momenta. These effects can be observed by measuring the identified particle transverse momentum distributions, e.g. - for pions and protons, and by measuring their elliptic flow as a function of transverse momentum.

Figure 1.5 [5] shows the PHENIX measurement of the invariant yield of pions, kaons and protons as a function of transverse momentum in Au+Au collision at $\sqrt{s_{NN}}$ = 200 GeV. From

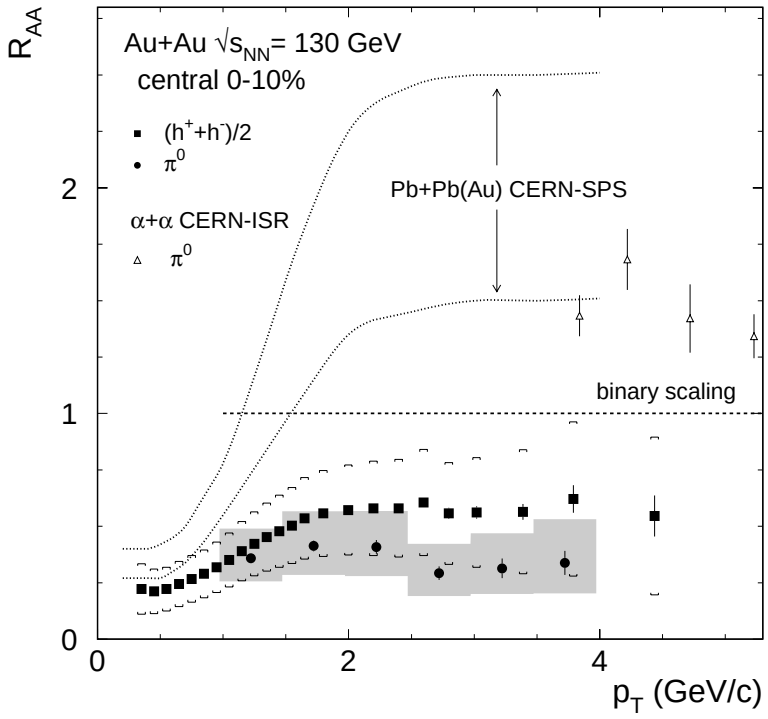

Figure 1.4: The ratio R_{AA} for charged hadrons and neutral pions in central Au+Au collisions in PHENIX experiment [4].

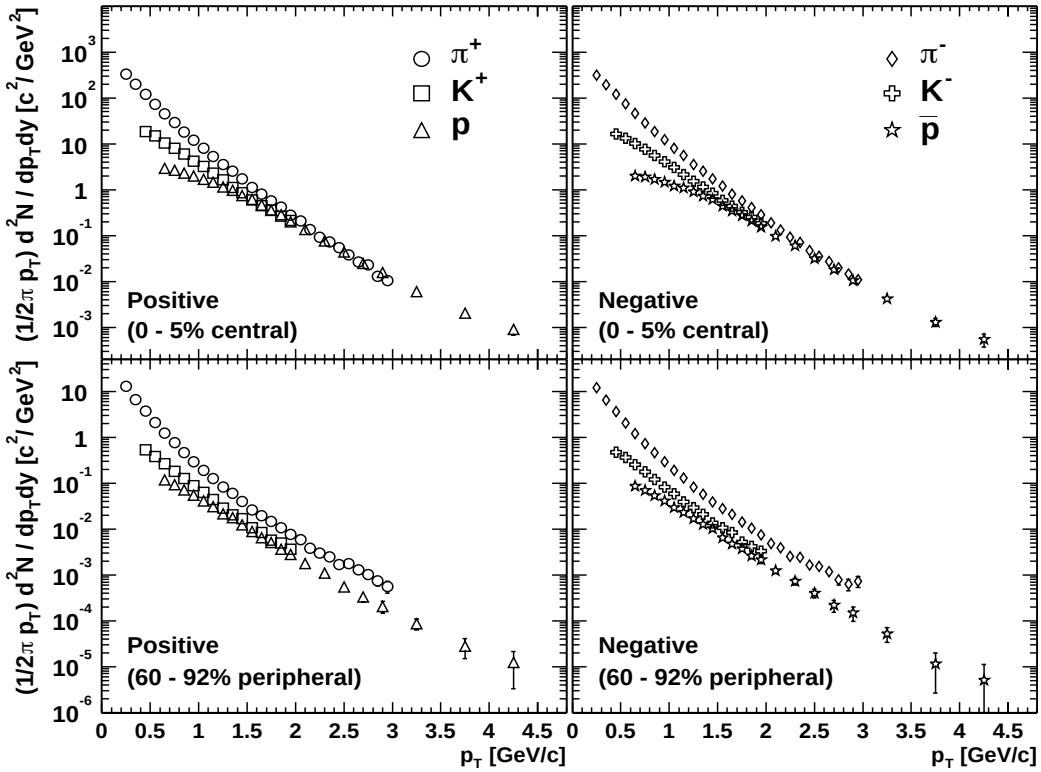

Figure 1.5: The invariant yield for pions and protons in Au+Au collision at $\sqrt{s_{NN}}$ = 200 GeV [5].

this figure, we can see there that is a clear mass dependence in the shape of spectra at low p_T. The proton spectra show a shoulder-arm shape, the kaon spectra fall exponentially, while the pion spectra have a concave shape. Up to 1.5 - 2 GeV, the spectra can be reproduced by hydrodynamic models. These models assume local thermal equilibrium and that the created matter is a liquid with a common flow velocity. The success of the hydrodynamic models can to some extend indicate the formation of QGP.

The elliptic flow is defined as the second order Fourier coefficient in the azimuthal distribution of the produced particles following the equation :

$$\frac{dN}{d\phi} \propto 1 + 2v_2 cos2(\phi - \Phi_{RP}) \tag{1.2}$$

Here, Φ_{RP} is the reaction plane angle. Figure 1.6 [6] shows the pion, kaon, and proton v_2

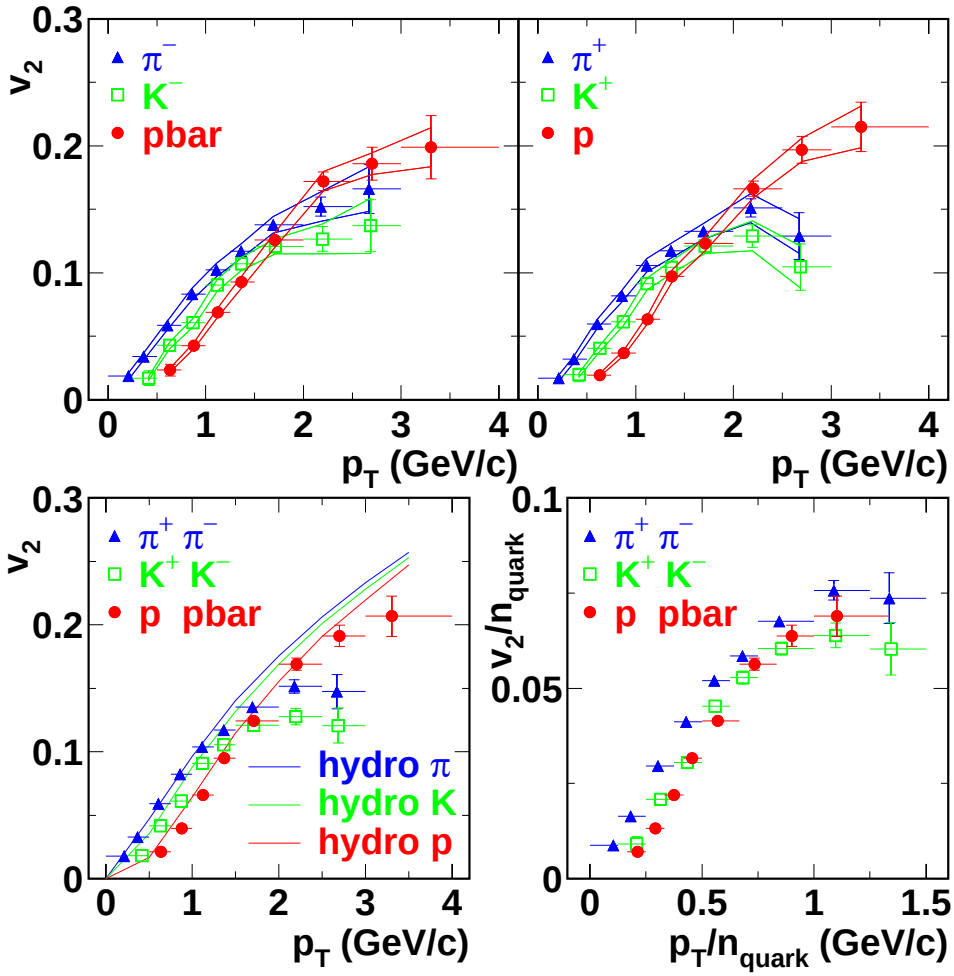

Figure 1.6: Transverse momentum dependence of v_2 for identified particles, pions, kaons and protons and their quark-number scaling [6].

as a function of transverse momentum. We can see that at low p_T, the pion v_2 is higher than that of the protons, and the order is reversed at around 1.5 GeV. This is kind of contradictory to what hydrodynamic models would predict, e.i. - that the pion v_2 would always be higher than that of proton. However, this change in hierarchy is captured in models invoking the quark coalescence mechanism of hadron formation, which indicates that the flow of hadrons has already been established at the quark matter phase.

1.3.3 J/ψ Production In Heavy Ion Collisions

The J/ψ meson is a charm and anti-charm pair. In heavy ion collisions, the production of J/ψ would be suppressed compared to pp collisions, since the attraction between the c and $\bar{c}$ pair would be weakened when immersed in QGP medium, similar to the Debay screening of electric charges in an electromagnetic plasma. In addition, at very high energies, due to the enhanced production of heavier quarks, a new production mechanism is thought to be at work [26] : the c and $\bar{c}$ from another pair could recombine to form a new c$\bar{c}$ pair. The measurements at LHC provide an opportunity to disentangle these two types of J/ψ production. The observation of either or both of the mentioned phenomena could imply the existence of deconfined QCD state. Figure 1.7 shows the inclusive J/ψ R_{AA} as a function of N_{part} measured at ALICE and PHENIX [7]. At N_{part} greater than 100, the suppression of J/ψ in ALICE is smaller than that in PHENIX data, which indicates the significant regeneration of J/ψ at LHC energies.

1.4 Motivation for This Thesis

1.4.1 Collectivity in Small Systems

Previously, it was thought that in small collision systems such as pAu and pPb collisions, could not produce matter that is hot enough with large enough volume such that it can undergo a phase transition to form QGP. However, since several years ago, some signatures of QGP found in large nucleus-nucleus collisions were also found in small collisions systems. In heavy ion collisions, two-particle angular correlations are often used to study the underlying particle production mechanism and the collective effects resulting from the high particle density formed in the collision. There are long-range (large pseudorapidity difference $\Delta|\eta|$) correlations in Pb+Pb collisions that are successfully interpreted as the consequence of the hydrodynamic flow of the produced strongly interacting medium [27]. However, in recently years, this kind of two-particle long-range correlations have also been found in high-multiplicity p+Pb, and even p+p collisions in CMS, ALICE, ATLAS [28, 8, 29], and in p+Au, d+Au,and ^{3}He+Au collisions in PHENIX [9, 30, 31].

Figure 1.8 shows the two-particle correlation at 5.02 TeV p+Pb collisions for low-multiplicity

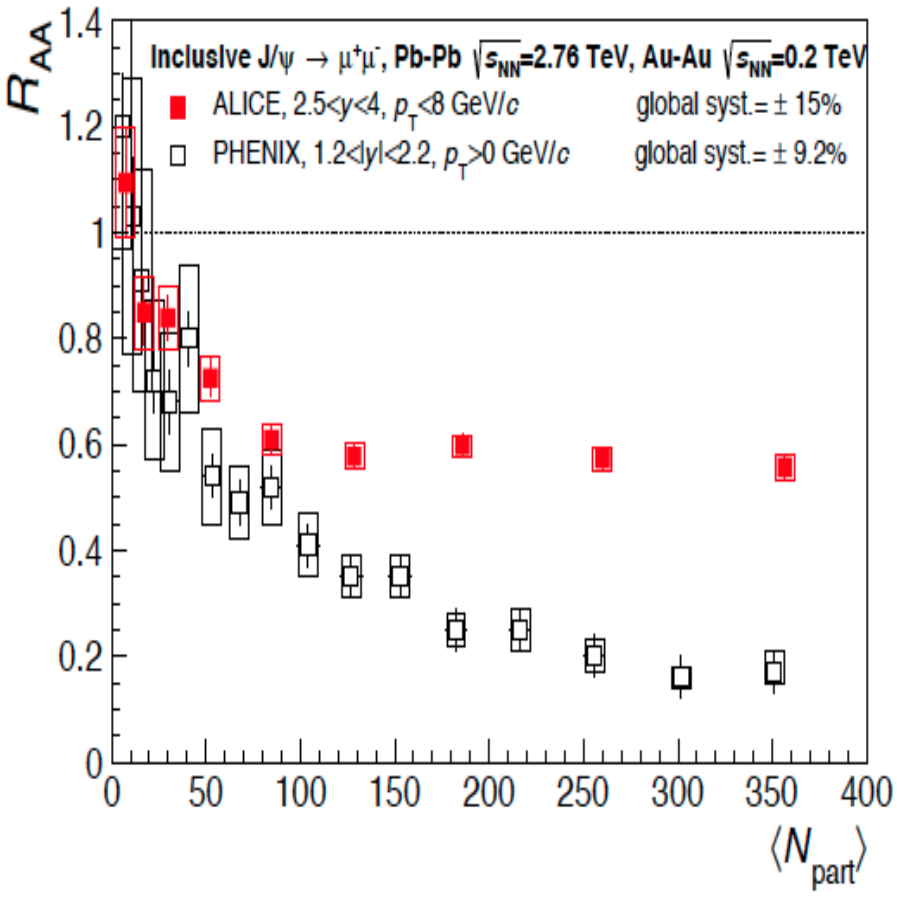

Figure 1.7: The inclusive J/ψ R_{AA} as a function of N_{part} measured at ALICE and PHENIX [7].

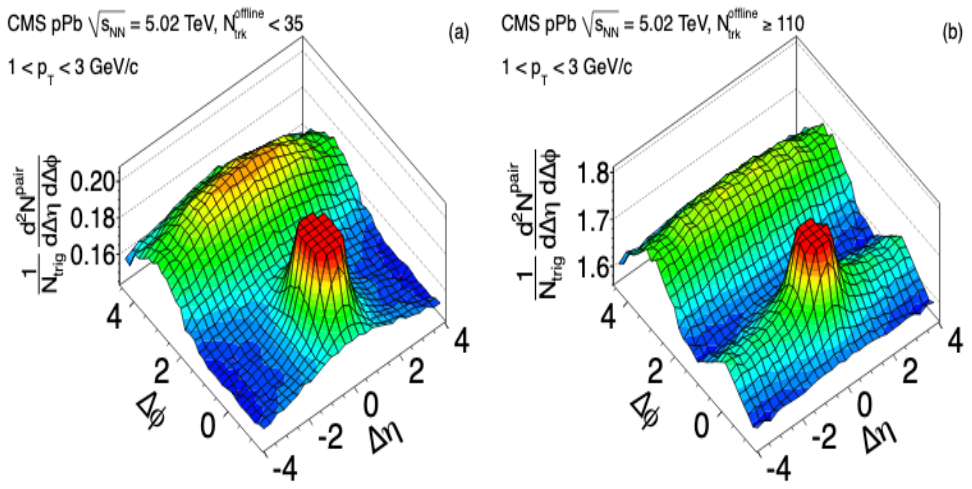

Figure 1.8: Two particle correlation at 5.02 TeV pPb collisions of charged particles with $1 < p_T < 3$ GeV for low multiplicity (a) and high multiplicity (b) events [8].

and high-multiplicity collisions. For low multiplicity, the correlations are peaked near $(\Delta\phi, \Delta\eta) = (0, 0)$, which originates from the particles coming from the same jet; the elongated structure at $\Delta\phi = \pi$ comes from particle pairs from back-to-back jets. In the high multiplicity case, the correlation extends to much larger pseudorapidity range. This structure, dubbed "the ridge", is very similar to that observed in Pb+Pb collisions.

The second order flow coefficient, v_2, can be extracted from the long-range part of the two-particle correlations effectively avoiding the correlations from the jets, which do not represent a global collective behavior. Figure 1.9 [9] shows the charged hadron as a function of transverse momentum in PHENIX and ATLAS. The dashed blue line shows the theoretical results from hydrodynamic calculation; and we found that they are in good agreement with the data.

As mentioned before, the common flow velocity will make the elliptic flow show a mass dependence, causing the mass-ordering of v_2 for pions and protons in Au+Au collisions. Prior to the work done here, this kind of signature has also been observed in d+Au and p+Pb systems [32]. Figure 1.10 shows the identified v_2 for pions and protons in d+Au and p+Pb collisions, we see very similar pattern seen in Au+Au collisions. So, it would be very interesting to see if the identified particle second-order Fourier coefficient behaves in the same way in p+Au collisions.

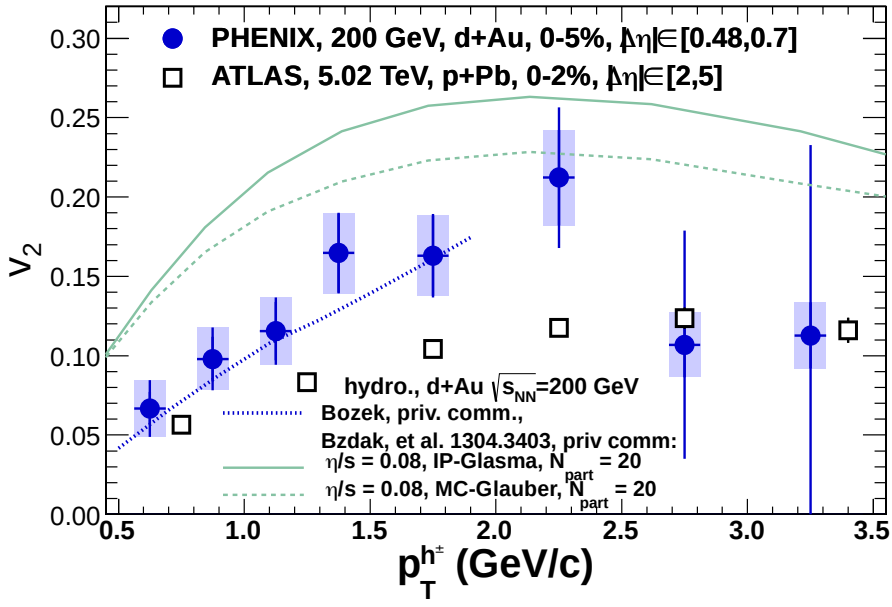

Figure 1.9: Charged hadron second-order anisotropy as a function of transverse momentum in PHENIX and ATLAS. [9].

This will have help with establishing if these flow patterns have the same origin in small and large systems, and if QGP can be the explanation in both. This is one of the goals of this thesis.

1.4.2 Theory Models for Heavy Ion Collisions

Various models are proposed to describe different stages of the evolution of the produced hot dense matter, including viscous hydrodynamics models, such as the Super hybrid mOdel simulatioN for relativistic heavy-Ion Collisions (SONIC) [33], and some models that do not implement hydrodynamics, such as the A Multi-Phase Transport Model (AMPT) [34]. Different models use different mechanisms to describe each stage. We take the SONIC and AMPT model as an example to explain the difference between two different kinds of implementation of several stages. Table 1.1 shows the different implementation of the several stages for hydro models and parton transport models. The main difference between SONIC and AMPT is at the medium expansion and hadronization stage. In SONIC model, the medium expansion is modeled using the viscous relativistic hydrodynamics by the equation of state; on the other hand, in AMPT model, this stage is described by the interactions of partons, whose distribution is described by

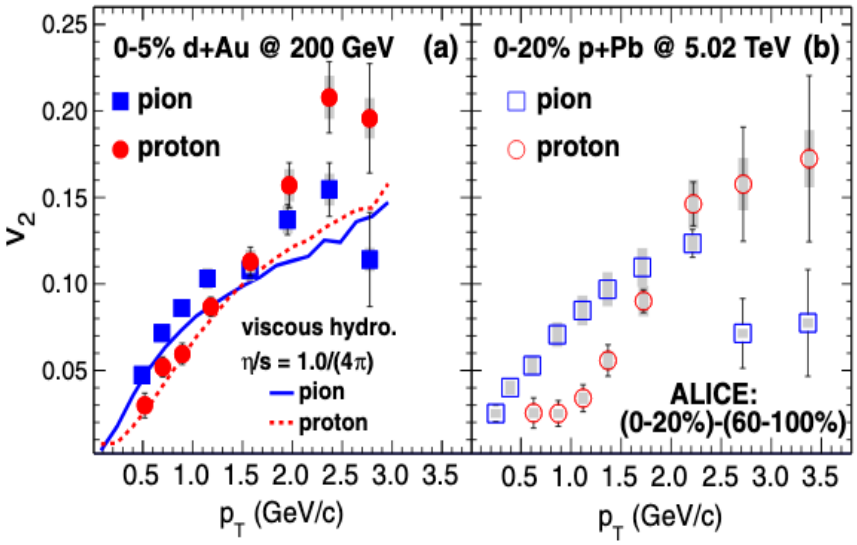

Figure 1.10: Measured $v_2(p_T)$ for identified pions and protons in d+Au and in p+Pb collisions [9].

the Wigner distribution. Another difference is during the hadronization stage. This stage is about how partons turn into hadrons. In the SONIC model, for the late-stage hadron interactions,the hadronic cascade code B3D [35] is used. Using the hyper-surface information to boost to the rest frame of each cell, the cascade is initialized with particles in the rest frame drawn from a Boltzmann distribution at a temperature T_{SW} with modifications of the momentum distribution to include deformations from viscous stress tensors [36]. In AMPT model, the hadronization is modeled by a simple quark coalescence model: combining two nearest partons into a meson and three nearest quarks (antiquarks) into a baryon‘[34].

So, the comparison of the p+Au identified particle spectra and elliptic flow measurements with different kinds of theory models will help us learn more about the different mechanism of particle production and the type of matter produced in different collision systems. This is another motivation for this thesis.

Besides that, the identified particle yields are one of the most basic observable that is necessary for constraining theoretical models. In a recent paper [10], J. Scott Moreland calibrated a Bayesian model using the p-Pb and Pb-Pb data points measured from CERN. The main idea of

Table 1.1: Different theory models of the stages in heavy ion collisions

Stages	Hydrodynamics (SONIC)	Parton Transport (AMPT)
Initial conditions	MC Glauber	MC Glauber
Particle production	NA	String melting
Expansion	Viscous hydrodynamics	Parton scattering
Hadronization	Cooper-Frye	Quark recombination
Final stage	Hadron cascade	Hadron cascade

this paper test if it is possible to to use a single set of parameters to model two systems: pPb and PbPb at the same time. That can answer the question of whether QGP can be formed in the small systems and if it can have the same properties regardless of the size. Since the measurements are the same center-of-mass energy, the only parameter that changes is the system size and nuclear structure.

The experimental data that can be used to calibrate the model are shown in figure 1.11. We can see that the identified particle yields play an important role. Other experimental data include the mean transverse momentum, which can be derived from the spectra, the charged-particle multiplicity and flow cumulants.

Figure 1.12 shows the prior distribution of the the model parameters, including the shear viscosity over entropy density η/s. The parameters are all set to be flat before observing any data and the ranges are set intentionally wide to avoid clipping the calibrated posterior.

After the calibration by Bayesian model, the posterior distribution of the model parameters is shown in figure 1.13. Since there are too many parameters, they project the results to one or two dimensions for a clear view.

In PHENIX, there are also several different collision systems with the same energy: pAl, pAu, dAu, ^{3}HeAu and AuAu. And the spectra for dAu and AuAu have been published several years ago. The measurement of the pAu spectra will give more data points for the model to use to calibrate the parameters.

- Charged-particle multiplicity $dN_{\mathrm{ch}}/d\eta$.
- Identified particle yields dN/dy of pions, kaons, and protons.
- Transverse energy production $dE_T/d\eta$.
- Charged particle mean transverse momentum $\langle p_T \rangle$ $(0.15 < p_T < 10$ GeV).
- Identified particle mean transverse momentum $\langle p_T \rangle$ of pions, kaons, and protons.
- Mean transverse momentum fluctuations $\delta p_T/\langle p_T \rangle$ (charged particles, $0.15 < p_T < 2.0$ GeV).
- Two-particle flow cumulants $v_n\{2\}$ for $n = 2, 3, 4$ (charged particles, $0.2 < p_T < 5.0$ GeV for ALICE, and $0.3 < p_T < 3.0$ GeV for CMS).
- Four-particle flow cumulant $v_2\{4\}$ (charged particles, $0.2 < p_T < 5.0$ GeV).
- Symmetric cumulants SC$(4, 2)$ and SC$(3, 2)$.

Figure 1.11: Experimental data used to calibrate the model [10].

TABLE I Input parameter ranges for the physics model.

Parameter	Description	Range
Norm	Normalization factor	9–28
p	Entropy deposition parameter	-1 to $+1$
σ_{fluct}	Nucleon fluctuation std. dev.	0–2
w	Nucleon width parameter	0.4–1.2 fm
n_c	Number of nucleon constituents	1–9
χ_{struct}	Nucleon structure parameter	0–1
d_{min}	Minimum inter-nucleon distance	0–1.7 fm
τ_{fs}	Free-streaming time	0.1–1.5 fm/c
η/s min	Minimum value of η/s (at T_c)	0–0.2
η/s slope	Slope of η/s above T_c	0–8 GeV^{-1}
η/s crv	Curvature of η/s above T_c	-1 to $+1$
ζ/s max	Maximum value of ζ/s	0–0.1
ζ/s width	Width of ζ/s peak	0–0.1 GeV
ζ/s T_0	Temperature of ζ/s maximum	150–200 MeV
T_{switch}	Switching/particlization temp.	135–165 MeV

Figure 1.12: Input parameter ranges for the model [10].

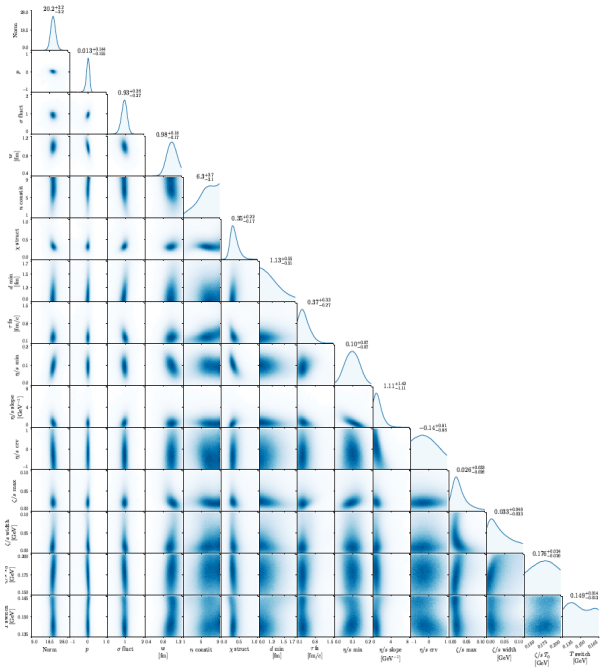

Figure 1.13: Bayesian posterior distribution of the input parameters [10].

Chapter 2

RHIC and PHENIX detector

2.1 The Relativistic Heavy Ion Collider

The Relativistic Heavy Ion Collider (RHIC) is the first collider in the world that can collide heavy ions. RHIC is located at Brookhaven National Lab in Long Island, New York. Compared to fixed target experiments, colliders can achieve a much higher center-of-mass collision energy.

Figure 2.1 [11] shows a simplified version of the RHIC layout and the acceleration scenario for Au nuclei. The ions are created at the pulsed sputter ion source and then sent to the Tandem Van de Graaff accelerator for an initial acceleration. When leaving the Tandem, the energy of the ions is 1 MeV/u and the charge state is +32. Then the ions enter the Booster synchrotron, where they are accelerated further to 95 MeV/u and stripped to a charge state at +77. After exiting the Booster, they enter the Alternating Gradient Synchrotron and are accelerated to 8.86 GeV/u and become fully stripped to a bare nucleus. Finally they enter the RHIC storage ring.

There are four interaction points at the RHIC ring : PHENIX, STAR, BRAHMS and PHOBOS. BRAHMS and PHOBOS have completed their mission in 2005. In 2016, PHENIX also completed taking data, and presently a new detector sPHENIX is being coustructed at the PHENIX interaction point.

Even though compared to the Large Hadron Collider, the center-of-mass energy of RHIC is an order of magnitude lower, it has more choices of collision energy and collision species. Since the magnets are separate for the two rings, RHIC can practically accelerate and collide any nucleus sepcies with any other. Figure 2.2 [12] shows the summary of the various collision energies and collision species that RHIC has collided from 2000 to 2017.

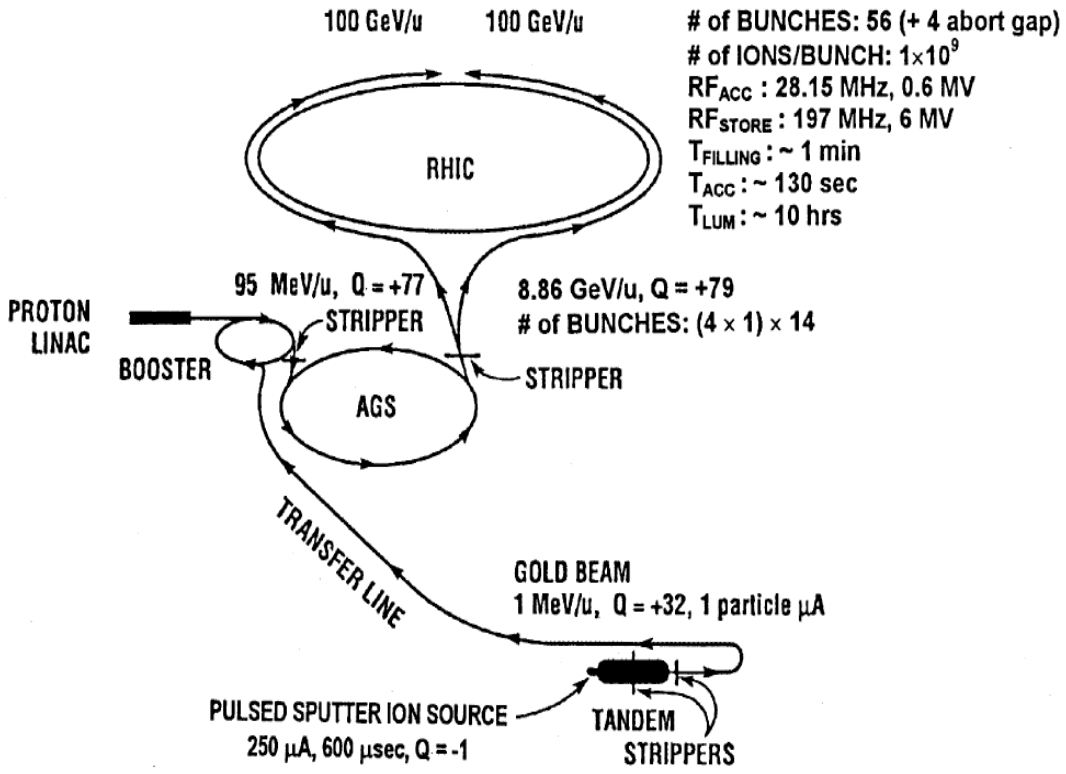

Figure 2.1: The simplified version of RHIC layout and the acceleration scenario for Au nuclei [11].

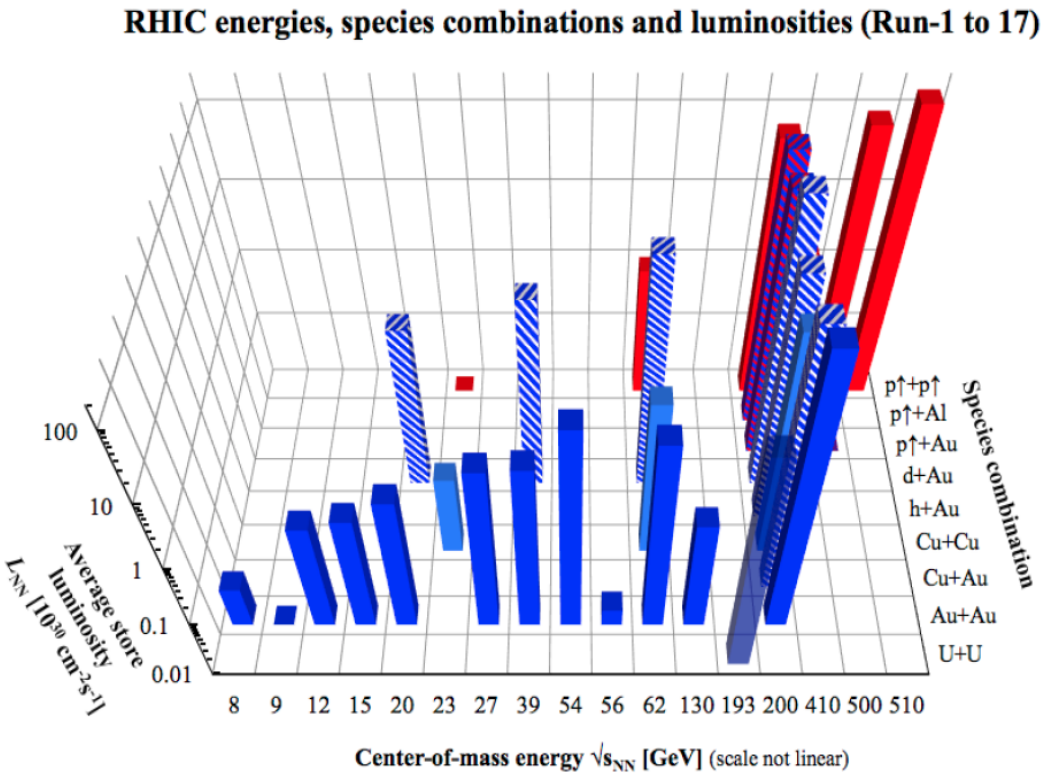

Figure 2.2: Summary of the RHIC collision energy and collision species.

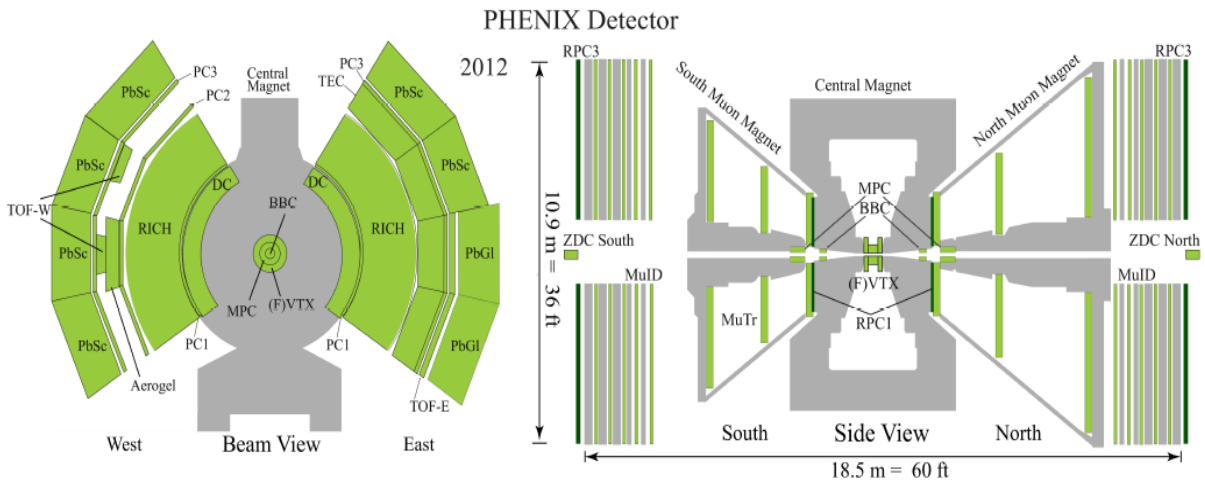

Figure 2.3: PHENIX detector configuration [12].

2.2 The PHENIX Detector

PHENIX, the Pioneering High Energy Nuclear Interaction eXperiment, is one of the four RHIC experiments. The design of PHENIX is mainly focused on the search for and characterization of new states of matter using electromagnetic probes and high transverse momentum phenomena [37]. There are several instrumented spectrometers and several global detectors in PHENIX. Figure 2.3 shows the PHENIX detector configuration from the beam view and the side view. In the following section, we will briefly describe some of them that are relevant for the measurements presented in this thesis.

2.2.1 Magnet System

From the right-hand side of Fig. 2.3 we can see there are three main magnet systems, the Central Maget, the North Muon Magent and the South Muon Magnet. The Central Magnet is around 9 meters tall and weighs about 500 tons [38]. This magnet provides a magnetic field around the interaction vertex and it is parallel to the beam axis, which is used for momentum analysis for charged particles. The magnetic field integral is around 0.78 T-m at 90 degrees. The Muon Magnet stands around 10.5 meters tall and weighs around 400 tons. It used two cylindrical coils to produce a radial magnetic field for the analysis of the trajectories of muons. The field

integral for the Muon Magnet at 15 degrees is around 0.75 T-m.

2.2.2 Global Detectors

The global detectors are used to determine quantities that relate to the collision itself and not to individual partiles produced in the collisions. PHENIX has Zero-Degree Calorimeters (ZDC), Beam-Beam Counters (BBC), that are essential to determine the collision centrality. Several different detectors can be used to determine the reaction plane orientation. These include the BBCs, and the Forward Silicon Vertex Detector (FVTX).

The ZDC are small transverse area hadron calorimeters located downstream of the beam pipelines. They measure the spectator neutrons, the neutrons that do not participate the collision, from the collision within a 2 mrad cone about the beam direction. They located around 18 meters away from the interaction point and the horizontal acceptance is +/- 5 cms. The measured spectator neutrons can be used for event-by-event characterization in conjuction with the BBC. Also coincidence signals from detectors on either side of the interaction region are used for luminosity monitoring.

Figure 2.4 shows the BBC detector; there are two of them, one on the north side , the other on the south side. They are located 1.4 meters away from the interaction vertex and the beam pipes goes through it. Each BBC has 64 elements; each element consists of quartz Cherenkov radiator and meshed dynode PMT. BBC can be used to determine the time zero of a collision, which can be used for the time of flight and particle identification. It is also used for centrality determination.

2.2.3 Central Spectrometers

There are two parts in the central arm spectrometers, the East side and West side. Each of them covers 90 degrees in azimuth and the pseudorapidity range is -0.35 to 0.35. The central arm is very good at particle tracking and particle identification. The particle identification for hadrons is done with the Pad Chambers (PC), Drift Chambers (DC) and the Time of Flight (TOF). The identification of photons and electrons is mainly done with the Ring-Imaging Cherenkov (RICH)

Figure 2.4: PHENIX BBC detector [13]

counter, the Lead Scintillator (PbSc) and the Lead Glass Calorimeters (PbGl).

The Drift Chamber is a multi-wire jet-type of drift chamber. It is located between 2.02 meter and 2.48 meter in radial distance from the interaction point. There are two Drift Chamber, one in the East arm and one in the West arm. Each of them has a 90 degree coverage in azimuth angle and in the beam direction the length is 1.8 meters. Figure 2.5 shows small slices of the Drift Chamber. From inner to outer, there are 6 layers of wires: X1, U1, V1, X2, U2, V2 [14]. The X wire nets are parallel to the beam pipe and are used to measure the azimuth ϕ angle coordinate of the track. The U/V wire nets have small angles with respect to the beam pipe and are used to measure the z-axis of the track. The purpose of Drift Chamber is to provide precise momentum measurement for charged particles and give initial information for the track projection to the outer detectors in PHENIX. The angular resolution for DC is around 1 mrad.

The Pad Chambers are multi-wire proportional chambers [39]. There are three layers of PC in the West arm, and two layers of PC in the East arm. The first layer of PC is just between Drift Chamber and the RICH in both arms. The second layer of PC only exist in West arm and is located after the RICH. The third layer of PC sits after the Time of Flight detector in both arms. PC1 combined with DC can be used to provide the 3-dimensional momentum vector. PC2 and PC3 can be used to reject particle tracks that do not originated from the vertex, which means

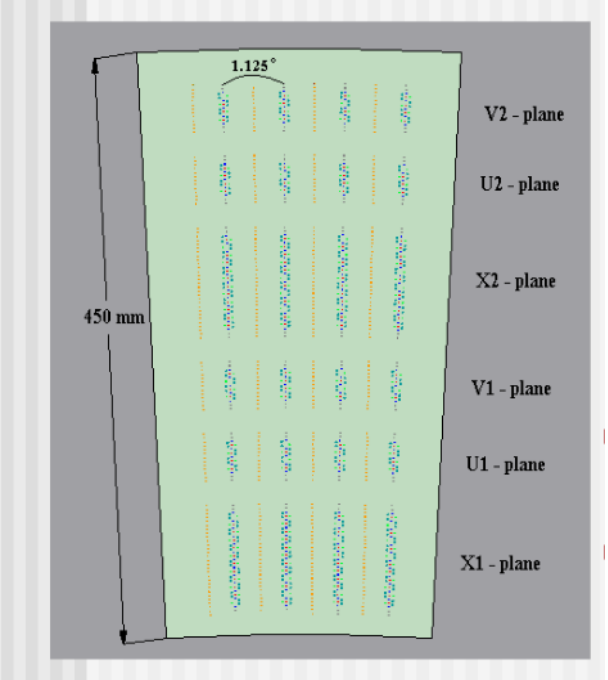

Figure 2.5: PHENIX Drift Chamber small slices [14].

secondary particles that are either produced by interactions with the detector material, or decayed particle.

The Time of Flight (TOF) detector measures the travel time and the travel length of the particles, combined with the momentum of the particle, we can calculate the mass of the particle using the following formula :

$$m^2 = ((\frac{cT_{tof}}{L})^2 - 1)p^2 \tag{2.1}$$

PHENIX has two separate time-of-flight detectors, the TOF-East and TOF-West. The techniques used in these two detectors are different. For the East arm, there are 2 sectors and 10 panels, as shown in figure 2.6. Each panel has 96 plastic scintillators, often called slats, the basic readout unit in TOF-East. Each slat has two photo-multiplier tubes (PMT) on the each end. TOF-East is located 5 meters from the interaction point in radial direction. The coverage of TOF-East is $\pi/4$ in azimuth direction and -0.35 to 0.35 for rapidity range. The timing resolution of TOF-East is about 120 ps. It can separate pions and kaons up to 2.4 GeV/c, kaons and protons up to 4

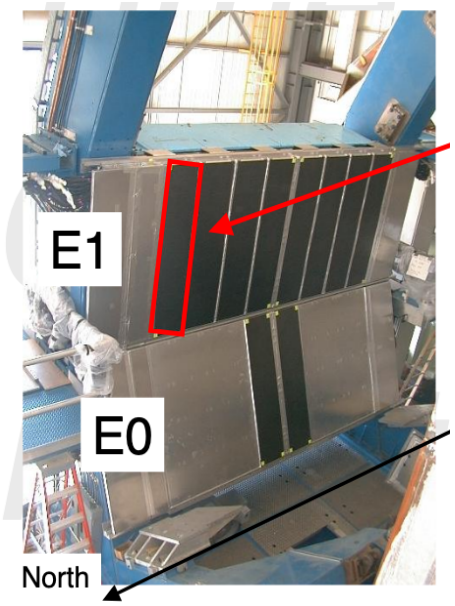

Figure 2.6: PHENIX TOF-East detector [15].

GeV/c. Figure 2.7 shows a the particle identification plot obtained using the TOF-E detector.

The TOF-West detector uses a different technique. It is based on Multi-Gap Resistive Plate Chamber (MRPC) technology, which improved the timing resolution to 79 ps and expanded the PHENIX PID functionality up to 9 GeV [40] in conjuction with the Aerogel Cherenkov detector. There are 4 boxes for the TOF-West, two in Sector 1 and two in Sector 2. Each box contains two rows and two layers of MRPC, 32 MRPCs per box. Each MRPC have 4 readout copper strips, read-out from both ends, making a total of 1024 TOF-West detector read-out channels.

The Silicon Vertex Tracker (VTX) detector is placed at the center of PHENIX. Its coverage is: $|\eta| < 1.2$, $\Delta\phi \sim 2\pi$. It has four layers, 2 inner layers of Pixel detector and 2 outer layers of Stripixel detector. The VTX can measure the Distance of Closest Approach (DCA) of a reconstructed track to the event vertex. In this analysis, we used the DCA distribution to remove the decayed anti-protons from lambdas, which is used to calculate the fraction of anti-protons that come from decay.

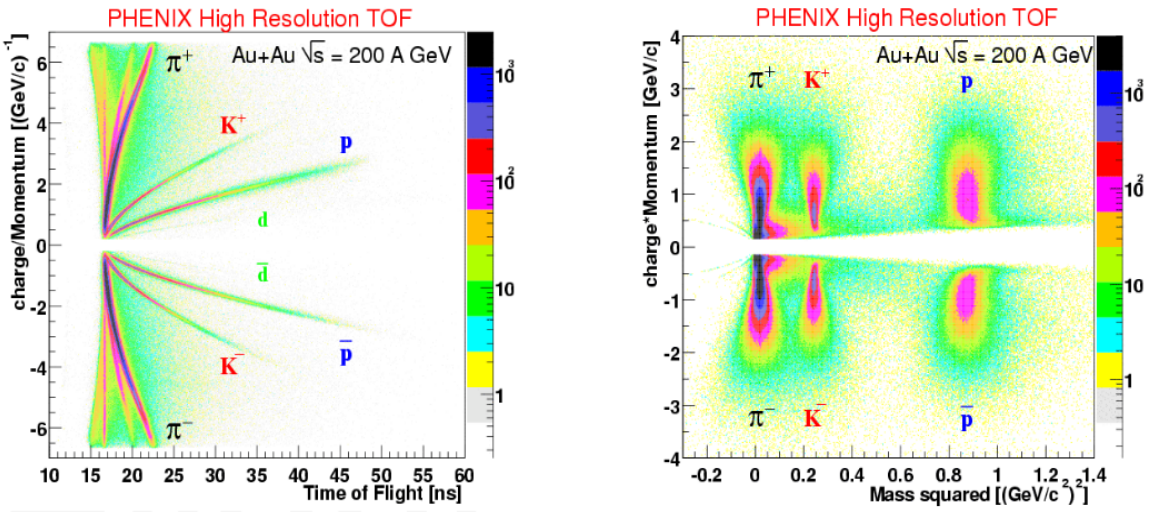

Figure 2.7: PHENIX TOF-East Particle identification [15].

Chapter 3

Analysis Details

3.1 Centrality Categorization

The impact parameter for each collision has a big influence on the results of the collision, but there is no way to measure this quantity in experiment. However, we can use another quantity derived from Monte Carlo Simulation to describe how close the collision is, which is called the centrality. The smaller the number, the smaller the impact parameter is. In this analysis, we used the following division shown in table 3.1. Also shown in this table is the N_{coll} : the number of binary nucleon-nucleon collisions, N_{part} : the number of nucleons participating in the collision, and the bias factor.

3.2 Data Selection

This thesis used the proton-gold collision data set and the proton-proton collision data set collected by PHENIX in year 2015. When the data were taken, to select the collision events of interested, PHENIX implemented many kinds of triggers to select which event to store. The two main triggers used in this analysis are the minimum bias trigger (MB), and the high-multiplicity trigger (HM). The minimum bias trigger requires that the event has at least one photomultiplier in BBC fired on each side of the detector, both North and South. In this way, around $84 \pm 4\%$ of the total inelastic p+Au collision cross section events are captured [12]. The high-multiplicity

Table 3.1: Centrality Categorization

Centrality	N_{coll}	N_{part}	bias factor
0-5%	9.7 ± 0.6	10.7 ± 0.6	0.86 ± 0.01
0-20%	8.2 ± 0.5	9.2 ± 0.5	0.90 ± 0.01
20-40%	6.1 ± 0.4	7.1 ± 0.4	0.98 ± 0.01
40-60%	4.4 ± 0.3	5.4 ± 0.3	1.02 ± 0.01
60-84%	2.6 ± 0.2	3.6 ± 0.2	1.00 ± 0.06
0-100%	4.7 ± 0.3	5.7 ± 0.3	0.858 ± 0.014

trigger is based on the minimum bias trigger, but further requires that there are more than 35 photomultipliers fired in the Au-going beam direction. These kind of events roughly corresponding to the 5% most central events in p+Au collisions.

Besides the selection on the trigger, we also have many other selection criteria regarding the particle trajectories (called "tracks") that we want to analyze, and these will be explained one-by-one in detail next.

3.2.1 Run Selection

At RHIC, initially of the order of 100 bunches of ions are injected in the rings; as times goes on, the beam luminosity will decrease, and the beam will be dupmed and new beams will be re-inhected. This period is called a fill. During the fill, the experiment will take data in chunks called "Runs" that are aimed to have approximately the same number of events recorded and have the same detector conditions. Depending on the luminosity, this can take from an hour to several hours. For the p+Au collisions, there are around 347 runs available for analysis as recorded in the PHENIX database. However, since the detector was not very stable, we limited the number of runs in the analysis to those that have similar detector performance. To select the good runs, we ploted the number of positive pions over negative pions for each of these runs and discarded the runs in which the ratio is too large or too small.

Figure 3.1 shows the negative pion over positive pion ratio measured in East arm for each run, we can see the ratio clearly separates into two parts, where apparently some detector element became non-functional. We only use the first part of the data, since the ratio is close to what we observed in the pp runs. We fit the first part with a straight line, the fitted value is 0.9152. Then we only select the runs whose ratio is between 95% and 105% of the fitted value. The cut is shown in red lines. Using this method, we selected 115 runs from the pAu dataset.

For this analysis, we only used East arm data. The reason is that there are some problems in West arm. Figure 3.2 shows the negative pion over positive pion ratio in West arm, we can see the ratio is much larger than one. The reason for this is that a large part of the drift chamber in front

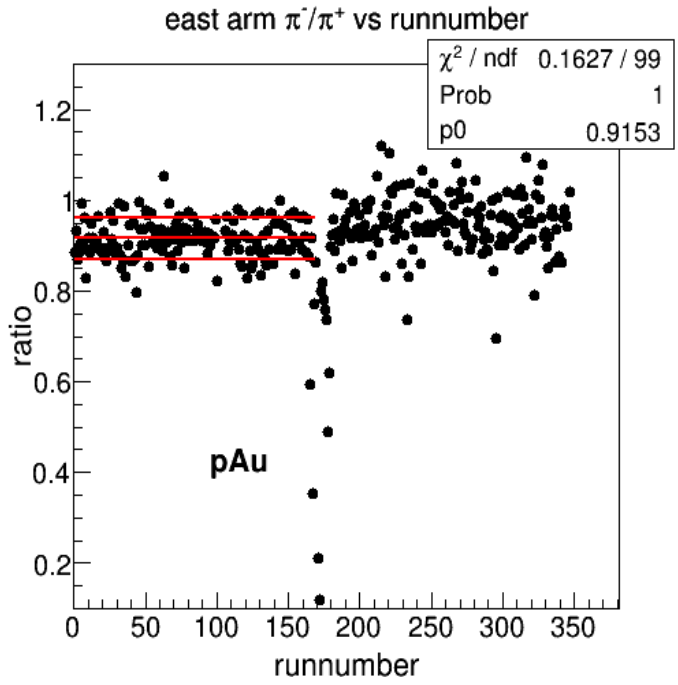

Figure 3.1: The ratio of the number of π^- over π^+ measured in the East arm versus run number (relabeled starting from 0)

of the time of flight detector in the West arm is broken and that mostly affects the acceptance for the positive particles. A large fraction of the positive particles were not detected. The details can be seen in the discussin of the fiducial map.

3.2.2 Event Selection

Except for the minimum bias trigger mentioned before, I also used some other cuts to select events. I only choose the events whose collision vertex is within 10 cm of the nominal origin of the coordinate system. The reason for this is that the VTX detector that is used in parts of the analysis to reject secondary particles only covers this region.

3.2.3 Track Selection

The track reconstruction in the Drift Chamber is based on a combinatorial Hough transform. The DC can determine the track momentum and the coordinates in the transverse plane, but since the X1 ad X2 DC wires are oriented along the z-axis, they can not provide z-information. This

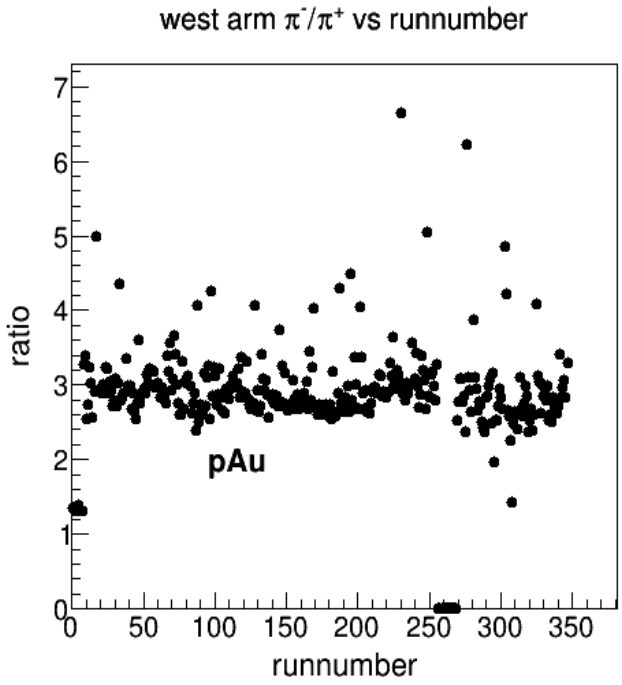

Figure 3.2: The ratio of the number of π^- over π^+ measured in west arm versus run numbers (relabeled

Table 3.2: Track quality bit information

Bit Position	Numerical Position	Condition
0	1	X1 Used
1	2	X2 used
2	4	UV found
3	8	UV unique
4	16	PC1 found
5	32	PC1 unique

can be obtained from the crossed wires U and V, or from PC1. There is some redundancy, in the detector design which is good, because the U and V wires were more delicate and difficult to operate. Primarily. PC1 is used to determine the z-position where the track hits PC1. We require the z-position is less than 75 cm, since the detector's performance will drop close to the boundary. Another variable we want to use for selection is called track quality. It is a 6-digit binary number. The digit will be 1 if the condition is satisfied and 0 otherwise. The digit information and the corresponding condition is listed in Table 3.2.

The best track quality is 63, the second best quality is 31, which corresponds to a matching

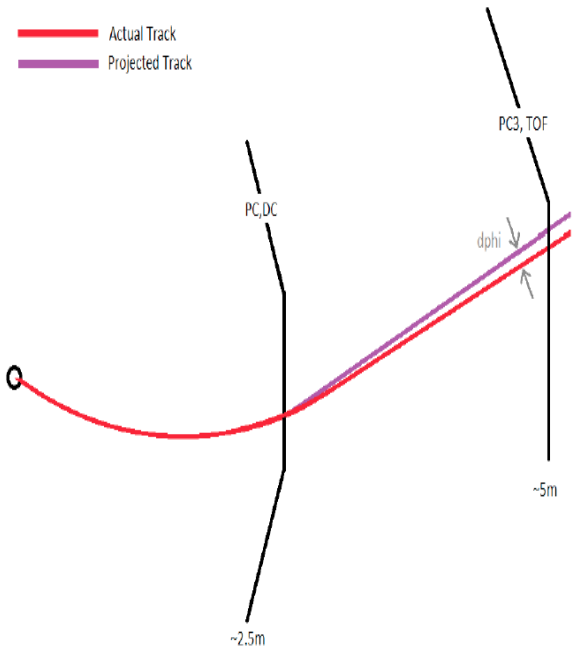

Figure 3.3: The difference between the actual hit position in PC3/TOF and the projected ones from DC

hit found in PC1, and tracks reconstructed in both X1 and X2 sections of the DC, and having unique UV wire assignment. So, we will only use the tracks whose track quality is either 31 or 63.

3.2.3.1 PC3 Matching

Besides requiring the track quality to be 31 or 63, we also used PC3 matching and TOF matching method to select tracks. As shown in Fig. 3.3, the tracks detected by Drift Chamber is projected to PC3 and TOF; and compared to the actual hits points in PC3 and TOF. The difference in azimuth direction is called dphi; the difference in beam direction is called dz. The distribution of dphi and dz are roughly Gaussian and we only select the tracks that are within two standard deviations of the dphi and dz distribution in both PC3 and TOF detector. In this analysis, we normalized the dphi and dz distribution to be a standard Gaussian distribution with mean of 0 and σ of 1.

We did PC3 matching in 50 separate p_T bins from 0 to 5 GeV, 0.1 GeV per bin, six z-vtx bins

from -30 to -20 cm, -20 to -10 cm, -10 to 0 cm, 0 to 10 cm, 10 to 20 cm and 20 to 30 cm. We also separated East and West arms, and positive and negative particles.

The result of the dphi double-Gaussian fit is shown in Fig. 3.4, and the one for dz is shown in Fig. 3.5. The black line is the Gaussian assigned for the signal; the pink line is the Gaussian modeling background tracks. The red line is the combination of the two. After we get the mean and σ of the Gaussian function, we smooth the mean value as a funtion of p_T with the function

$$f(x) = a + bx + \frac{c}{x} + \frac{d}{\sqrt{x}} + \frac{e}{x^2} + \frac{f}{x^3} + \frac{g}{x^4}$$

and we smooth the distribution of σ with the function

$$f(x) = a + bx + cx^2 + dx^3 + ex^4 + fx^5 + \frac{g}{\sqrt{x}} + \frac{h}{x^2}$$

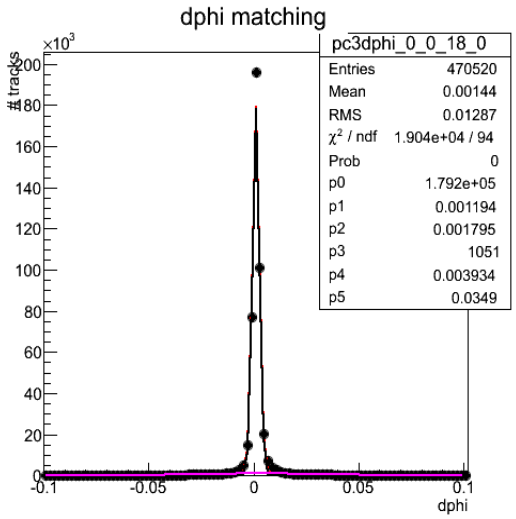

Figure 3.4: Double Gaussian fit of PC3 dphi in the range 1.7 GeV $< p_T <$ 1.8 GeV.

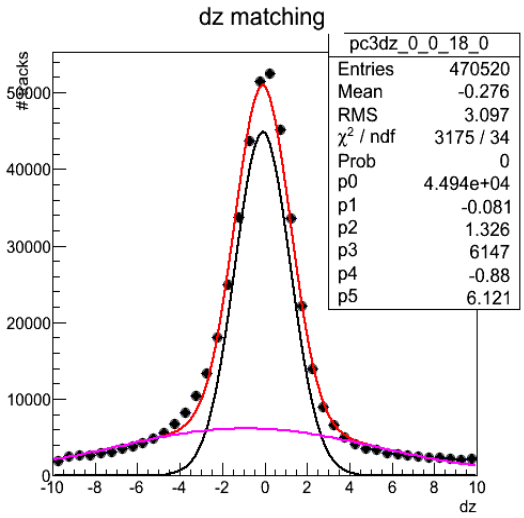

Figure 3.5: Double Gaussian fit of PC3 dz in the range 1.7 GeV $< p_T <$ 1.8 GeV.

The results of the smooth distributions for dphi mean, dphi sigma, dz mean and dz sigma are shown in Figs. 3.6, 3.7,3.8, and 3.9. The red lines are the fitted function.

The smooth function comparision between different zed bins is shown in Figs. 3.10, 3.11,

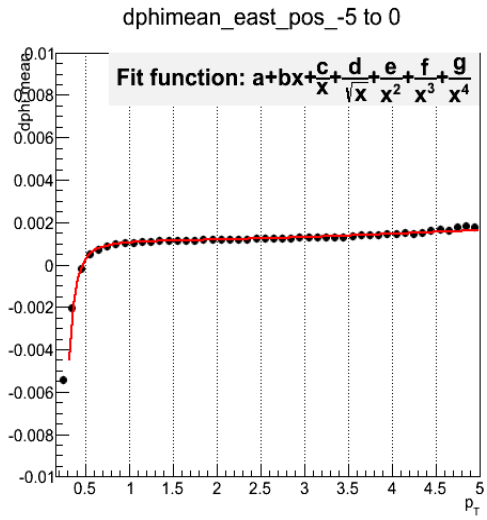

Figure 3.6: dphi mean smooth results for vtx zed in the range -5 to 0 cm.

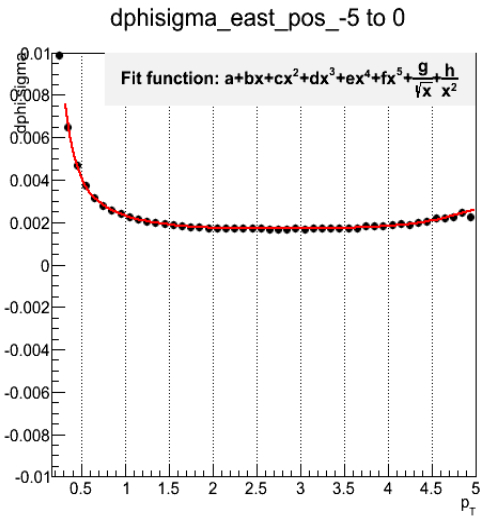

Figure 3.7: dphi sigma smooth results for vtx zed in the range -5 to 0 cm.

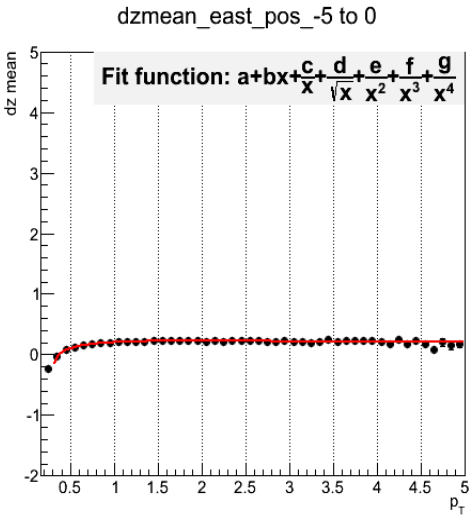

Figure 3.8: dz mean smooth results for vtx zed in the range -5 to 0 cm.

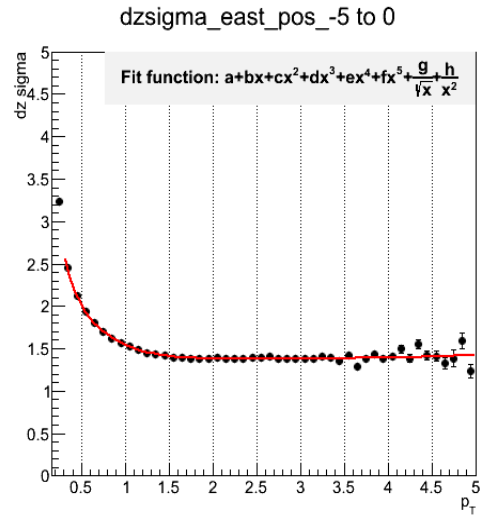

Figure 3.9: dz sigma smooth results for vtx zed in the range -5 to 0 cm.

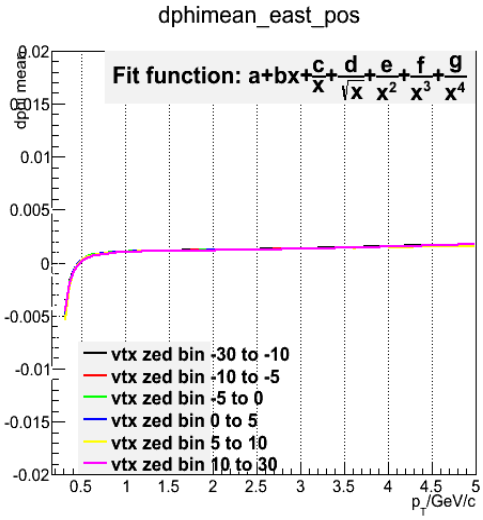

Figure 3.10: dphi mean smooth results

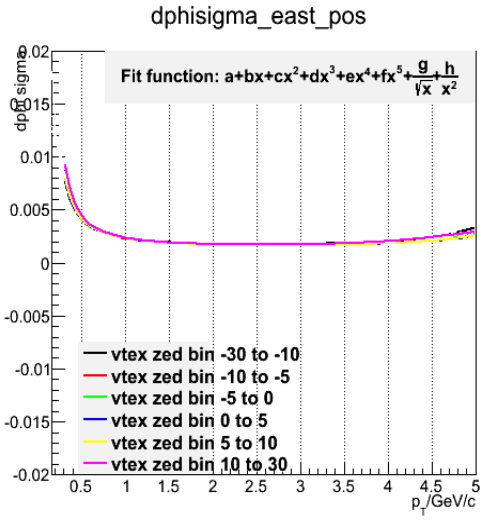

Figure 3.11: dphi sigma smooth results

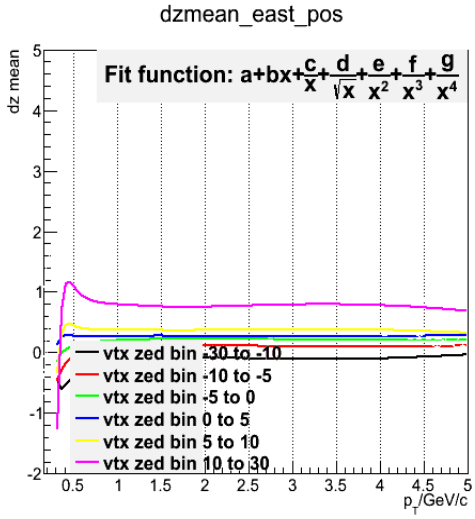

Figure 3.12: dz mean smooth results

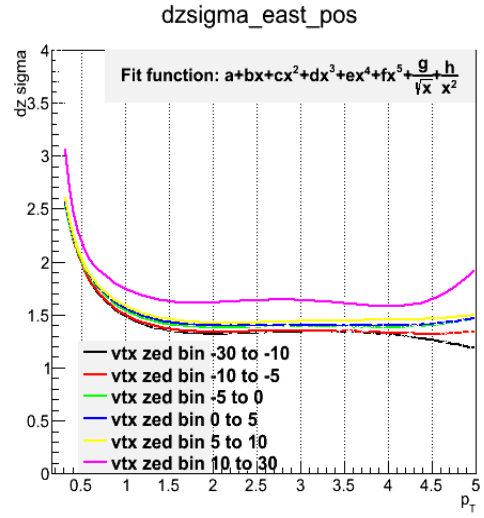

Figure 3.13: dz sigma smooth results

3.12, 3.13. From the plot we can see there is not much difference for dphi in different zvtx bins, but for dz there did exist some difference between different zvtx bins, and this is what is expected.

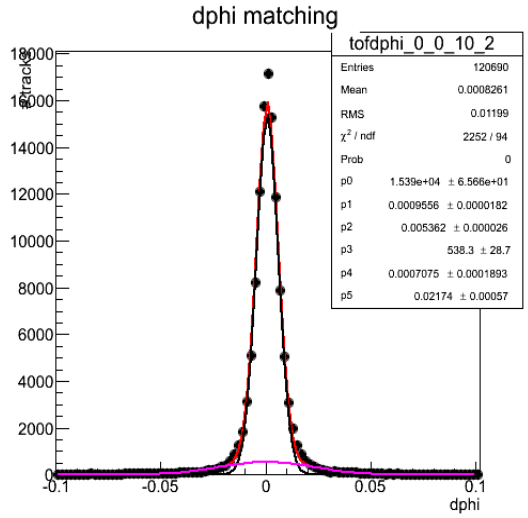

Figure 3.14: TOF dphi double Gaussian fit.

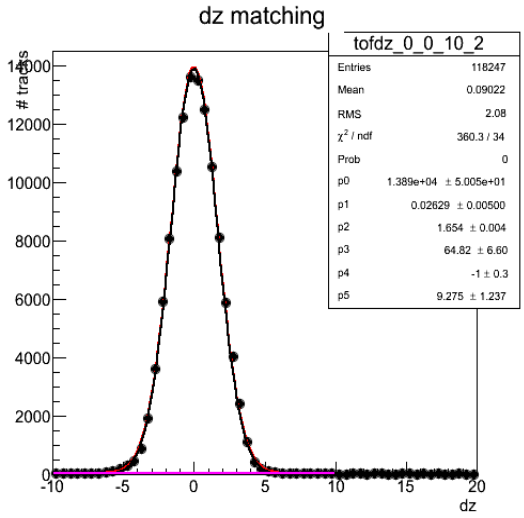

Figure 3.15: TOF dz double Gaussian fit.

3.2.3.2 TOF Matching

As with PC3 matching, we also need to calibrate the track-matching for the TOF detectors. We also separate the data into six vertex bins. The double-Gaussian results for the TOF matching for the second vertex bin are shown in Figs. 3.14, 3.15. The smoth results of the distributions of the mean and sigma are shown in Figs. 3.16,3.17, 3.18,3.19.

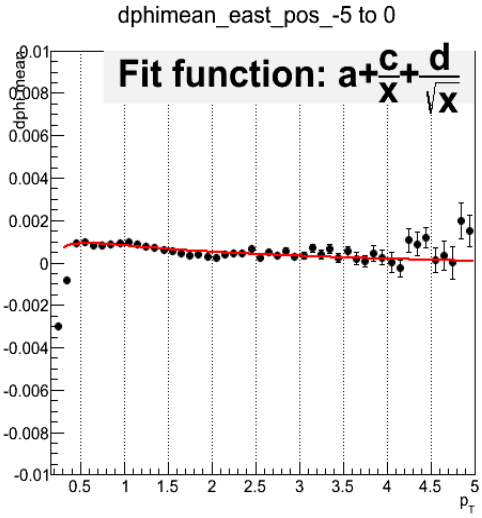

Figure 3.16: dphi mean smooth

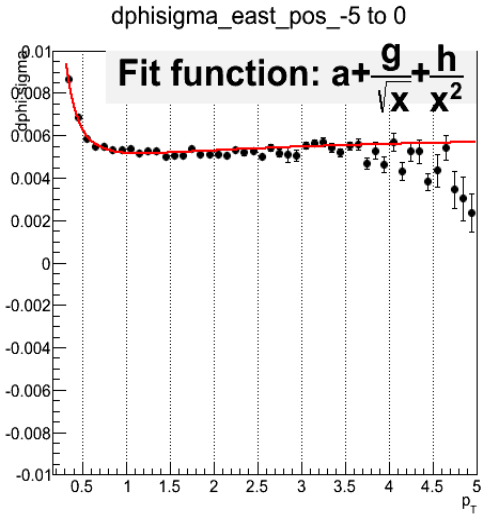

Figure 3.17: dphi sigma smooth

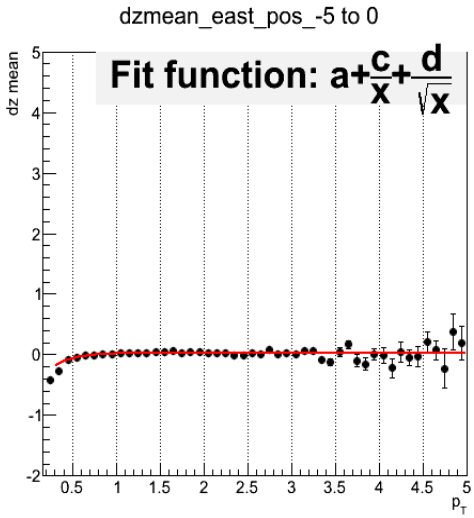

Figure 3.18: dz mean smooth

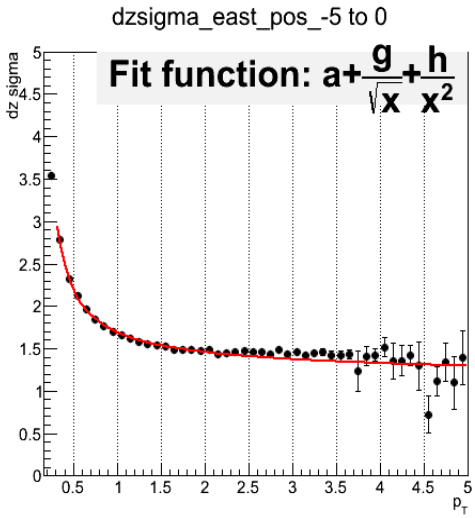

Figure 3.19: dz sigma smooth

3.3 Timing Calibration

In PHENIX, we identified particle according to the mass of the particle. According to the equation of special relativity, we will need the particle's velocity, which requires the track's length, and the time of flight. The start time is measured by the BBC and the end time is measured by TOF. Due to some hardware related issues, the timing measured by the TOF detector may not be correct and we need to do some timing calibrations. To do time calibration, we use pion as the standard, because pion is the most abundant particles produced in the collision. The time measured by the detector is denoted by t_{mea}, and the time calculated by theory is denoted by t_{theo}, the difference between these two values should be a Gaussian function centered at zero. But due to some hardware conditions, such as the time spent when the electric signal propagates through the wire, and the time-walk effects of the pulse-height spectrum (slewing effect) in the leading-edge discriminator used to digitize the signal, there are channel-by-channel differences in the time offsets and slewing that need to be calibrated through an iterative procedure that involves a series steps.

There are several different kinds of calibration that need to be done. As mentioned before, there are 960 scintillator slats in TOF-East and 512 copper strips in TOF-West - and these are read-out from both end. Each slat or strip may have its own bias, which means that the time measured in different slats may be centered at a different mean value. We need to correct this slat-by-slat. The method to achieve this is to fit the time measured by each slat with a Gaussian function and extract the mean value; then subtract the time offest to center the distribution at zero. Another calibration is related to the run-by-run variatios. Different run period may have very different mean values because the time difference between the BBC (which gives the start time) TOF can change. We need to make sure they are all centered at zero using the same procedure as in the slat-by-slat calibration of the time offsets.

3.3.1 Slat-by-slat Offset

The deltat for TOFw has an overall of nearly 30 ns shift from 0, as shown in Fig. 3.20. So, we need to move it back to 0 first, to do this, we fit the deltat for each slat by a Gaussian function and subtract the mean value from the deltat. The Gaussian fit of slat number 11 is shown in Fig. 3.21.

The deltat distribution after the slat-by-slat correction is shown in Fig. 3.22. We can see that after this slat offset, we can clearly see the three peaks, which corresponding to pions, kaons and protons.

3.3.2 Run-by-run Offset

During the data taking period, the detector will run for several hours and the detector condition and external factors, such as temperature, pressure, gas flow, etc for different runs maybe different. Therefore, their deltat may drift with time to a different mean value. To remove this difference, we need to do a run-by-run offset. We fit the deltat distribution for each run period, get the mean value and extract the mean values from all time measured during this specific run. The deltat distribution for run number 432639 is shown in Fig. 3.23.

3.3.3 Slewing Calibration

The method we measure TOF timing may introduce some amplitude dependent error. As shown in Fig. 3.24, the two signals should trigger at the same time, however, due to the fact that the trigger is engaged when the voltage pulse crosses a pre-define threshold, the signal with lower amplitude will cross the the threshold later and the corresponding digital pulse will appear later. This will introduce some pulse-height dependent time walk. As shown in Fig. 3.21, the x axis is a charge-related variable; y axis is the difference between measured time and the expected time. We can see there is clearly dependence on pulse-height and this is an intrinsic bias of the detector electronics that needs to be fixed. We can fix this using a pulse-height-dependent time offset, called slewing calibration. This offset is slat related so it is corrected slat-by-slat. The offset caused by this is a function of the average integrated charge of one MRPC strip. The functional

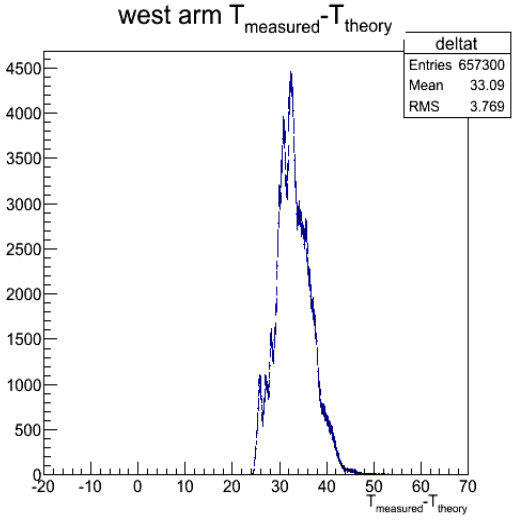

Figure 3.20: deltat of TOFw

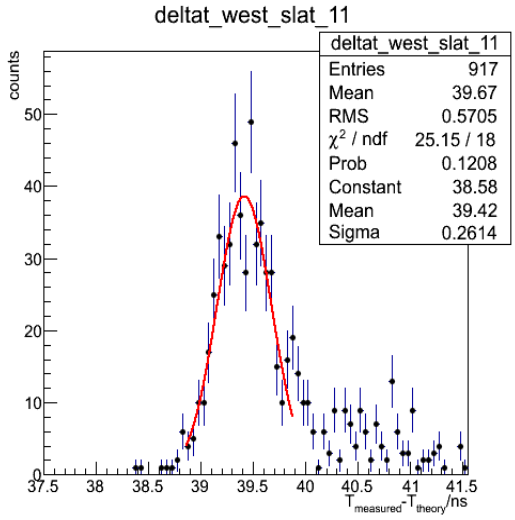

Figure 3.21: TOFw slat 11 Gaussian fit

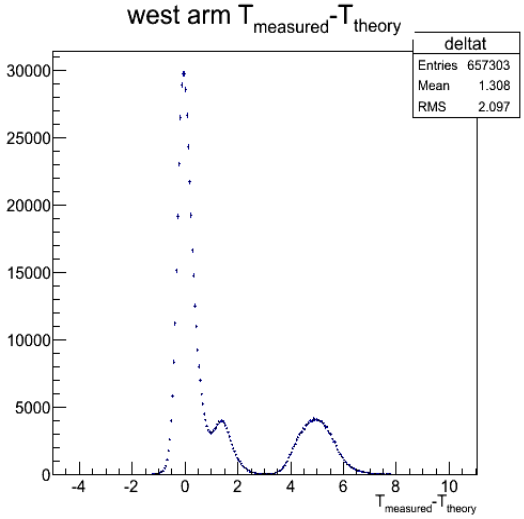

Figure 3.22: deltat of TOFw after offset

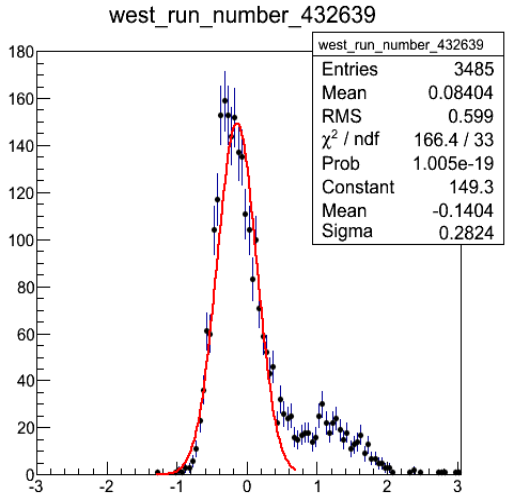

Figure 3.23: deltat for runnumber 432639

form is as follows:

$$T_{slewing} = A + (B/ADC_{STRIP}^{0.4})$$

where ADC is defined as

$$ADC = \sqrt{Q_{up}Q_{down}}$$

Q_{up} and Q_{down} are the charge measured in the two ends of one MRPC copper strip.

So, we draw a 2-D histogram of deltat and ADC and fit it with a 2 parameter function. The fit results of slat 11 and slat 489 are shown in Figure 3.25, 3.26. After we got the fit function, we extract the corresponding value from that time measurement.

3.3.4 Slat-by-slat and Run-by-run Calibration

After the slewing calibration, we redo the slat-by-slat calibration and run-by-run calibration twice to further reduce the deltat dependence on slat number and run number, the plots are show in Figs. 3.27,3.28, 3.29,3.30.

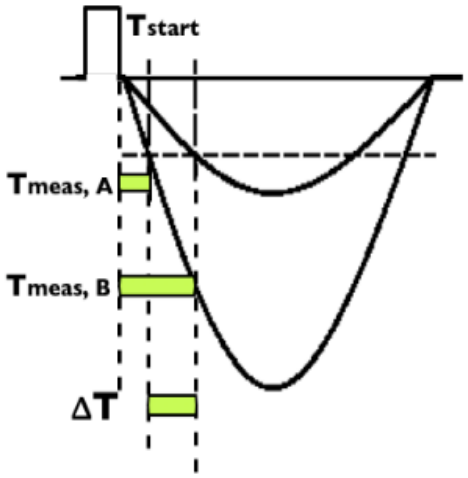

Figure 3.24: Small pulse height induced time walk

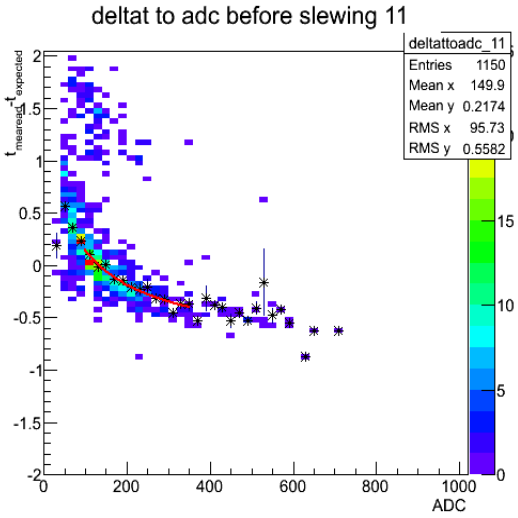

Figure 3.25: slat 11 fit

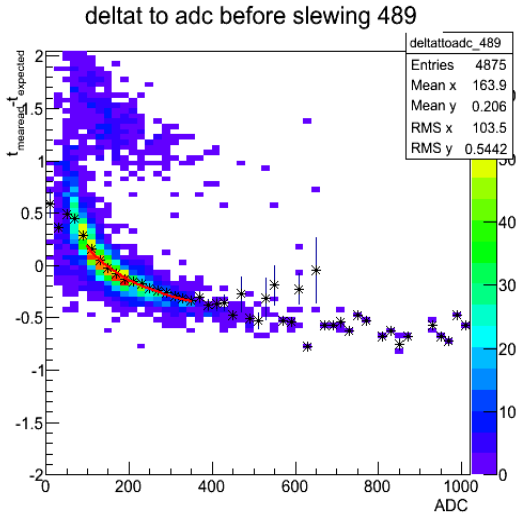

Figure 3.26: slat 489 fit

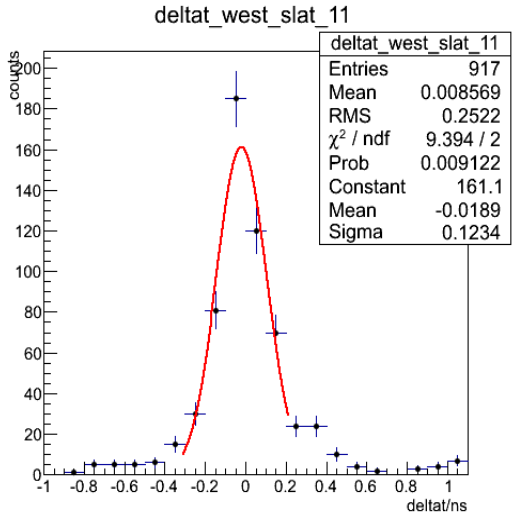

Figure 3.27: slat-by-slat 1 calibration

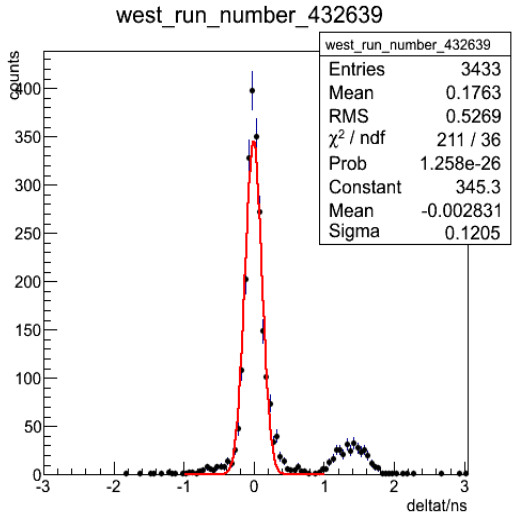

Figure 3.28: run-by-run 1 calibration

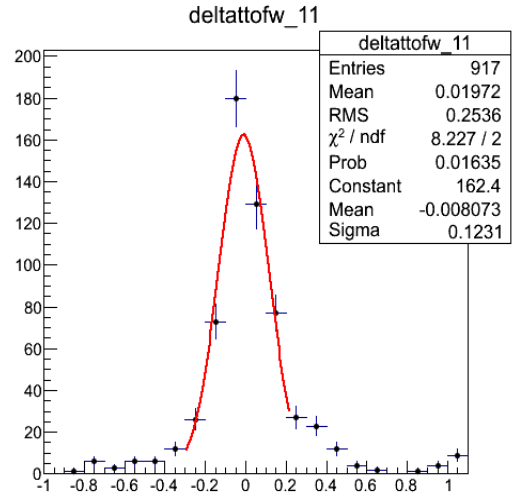

Figure 3.29: slat-by-slat 2 calibration

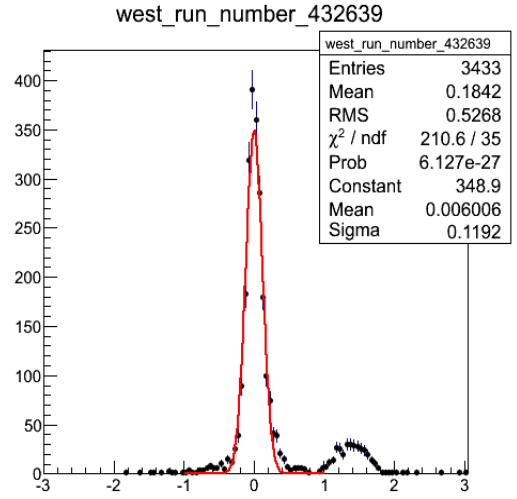

Figure 3.30: run-by-run 2 calibration

3.3.5 Timing Resolution after Timing Calibration

In this section we will have a look at the timing resolution before and after calibration. On the following four figures, the upper left shows the East arm mean vs slat number (run number), the upper right shows the East arm σ vs slat number (run number), the lower left shows the West arm mean vs slat number (run number), lower right shows the West arm σ vs slat number (run number). Figure 3.31 shows the mean and σ distribution as a function of slat numbers before timing calibration, and Fig. 3.33 shows the same thing after timing calibration. We can see there is a large improvement for the timing resolution for both West arm and East arm TOF detectors. Another thing we notice is that the timing resolution of West arm is better than that of the East arm TOF, which is due to the different detector technology (scintilla tors vs MRPC). However, since there are acceptance problems in West arm, we only use the East arm for the spectra measurements, which require absolute normalization; both were used in the flow measurements, which do not. Figures 3.32 and 3.34 show the timing resolution for each run period before and after the timing calibration. We can also see an improvement.

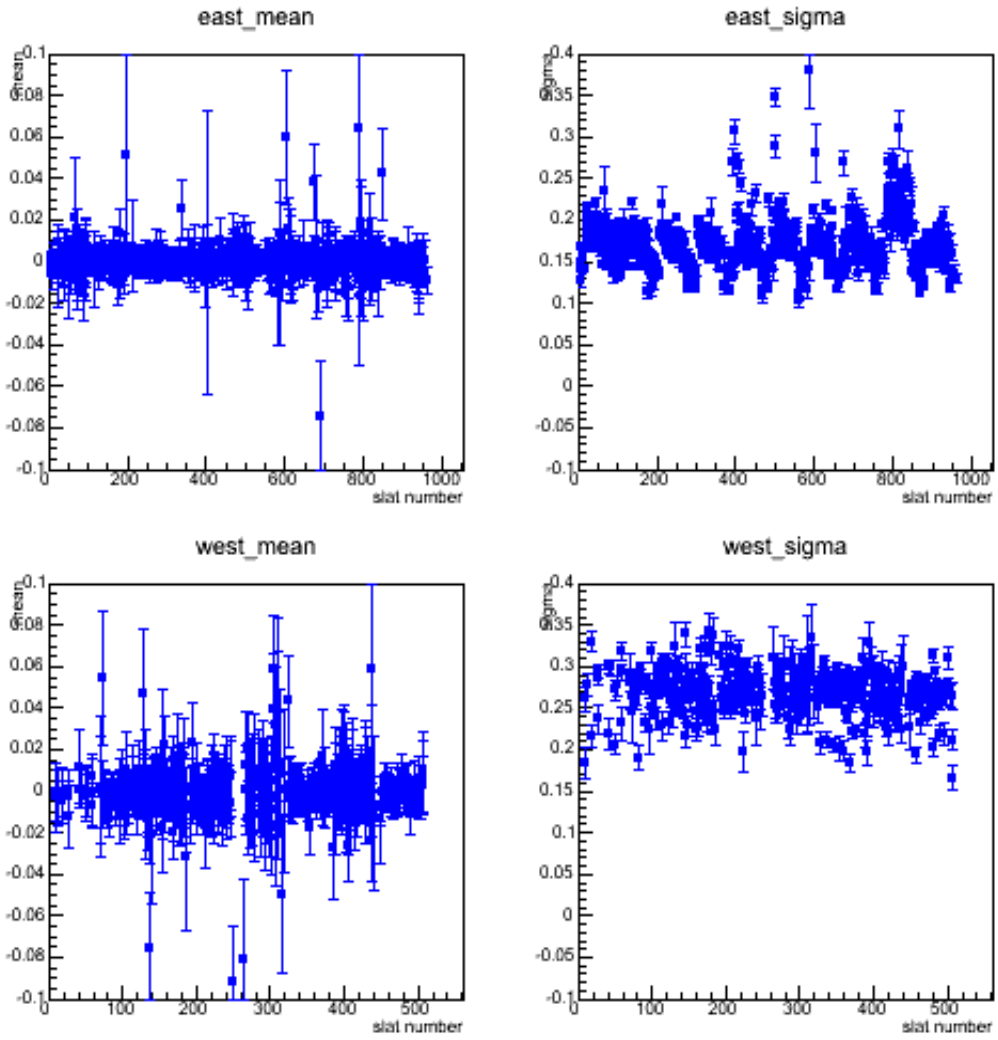

Figure 3.31: slat-by-slat mean and σ before calibration

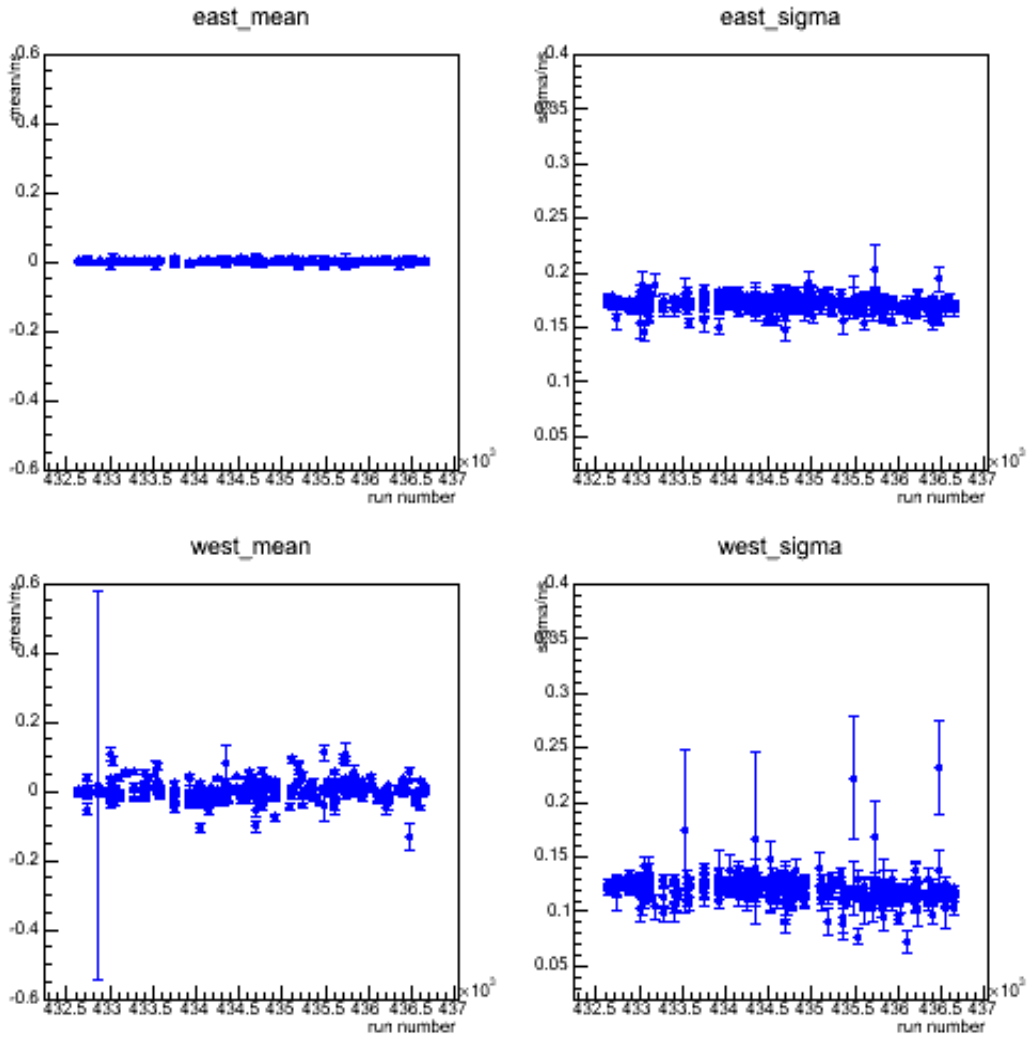

Figure 3.32: run-by-run mean and σ before calibration

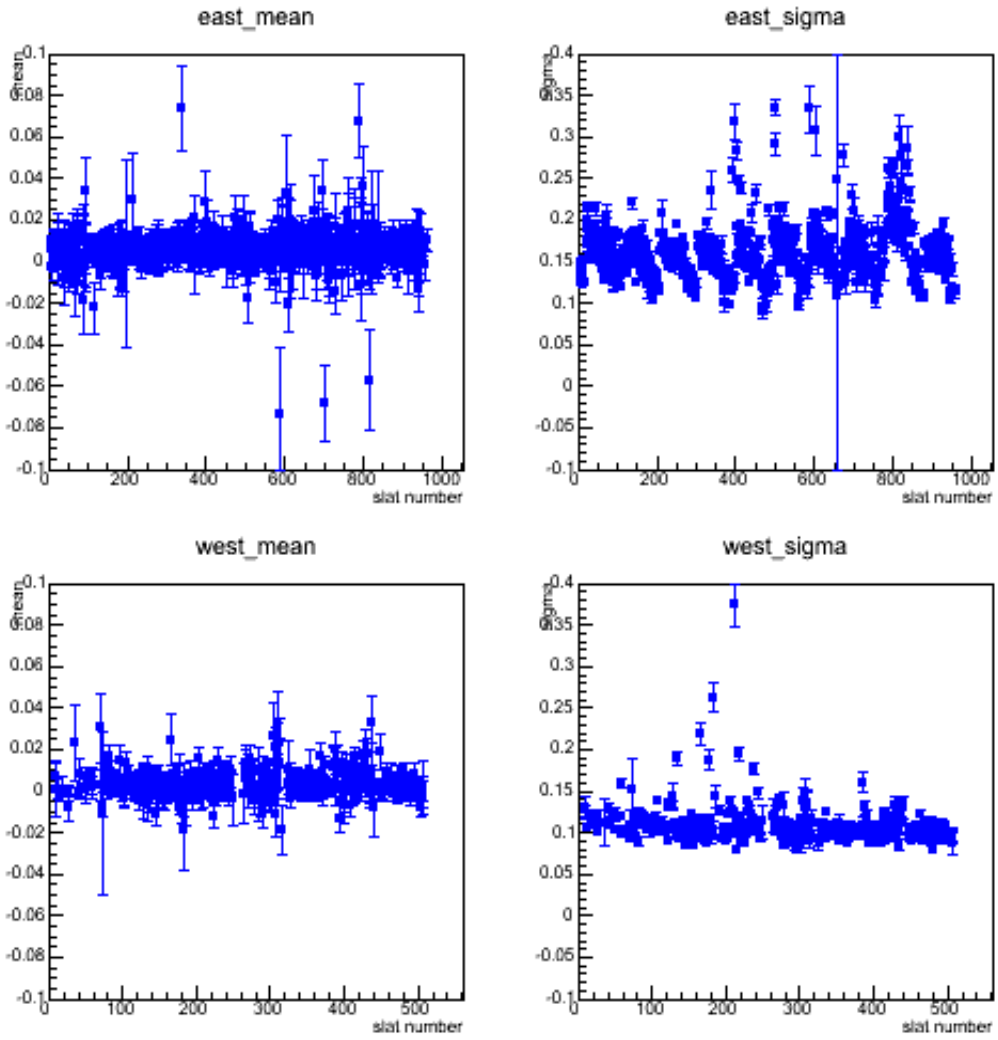

Figure 3.33: slat-by-slat mean and σ after calibration

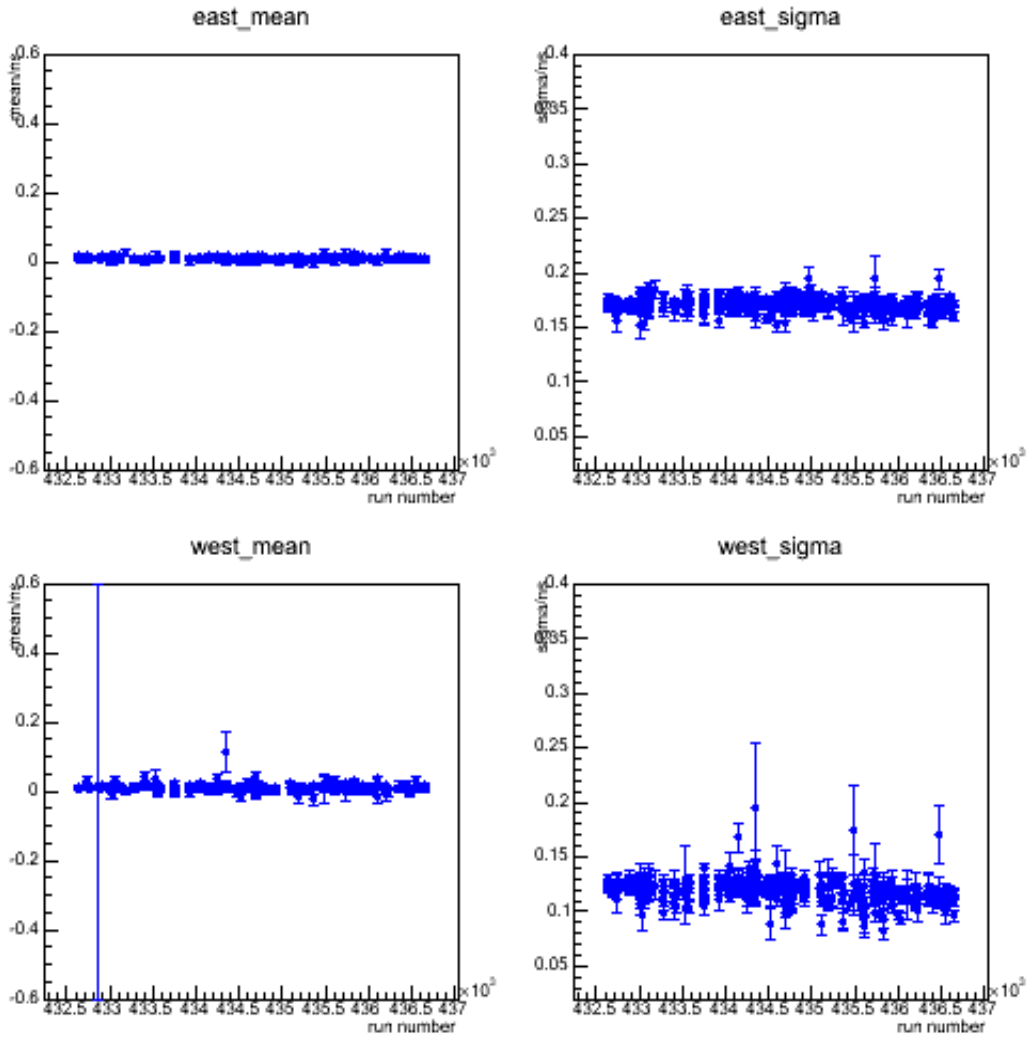

Figure 3.34: run-by-run mean and sigma after calibration

3.4 Particle Identification

We identified particles using their mass, to calculate the mass of a particle, we need the length of the track, the time of flight and the momentum. As stated in specially relativity, the particle's energy and momentum in relativistic regime is expressed in the following formula:

$$E^2 - (pc)^2 = (mc^2)^2$$

Combined with the equation:

$$E = \frac{pc}{\beta}$$

where β is defined as $\beta = \upsilon/c$, we got the following expression:

$$(mc^2)^2 = (\frac{1}{\beta^2} - 1)(pc)^2$$

Plug in the function for the velocity $\upsilon = L/T_{tof}$ and be expressed in proper units, we can get the final formula for calculating the mass of the particle:

$$m^2 = ((\frac{cT_{tof}}{L})^2 - 1)p^2$$

Since we have the right timing, it is time to do the particle identification for pion, kaon and proton. Figure 3.38 shows the m^2 as a function of $p_T \times charge$. Figure 3.39 shows its projection to pt range 1.8-1.9 GeV; and it is fitted with a tripple Gaussian to extract the mean and σ of the three particles. We can see clearly that the positive proton band is broader than the negative one and the reason for this is that there are many knocked out protons from VTX detector, which are also observed in the simulation.

Figure 3.35 shows the reconstructed particles' mass^2 distribution from simulation when negative pions are the input to the simulation. We can see even if there are only negative pions as input, we see protons in the simulation output. If we further look at the vertex position of protons in x-y plane, as shown in figure 3.36. We can see some particles vertex are far away from the

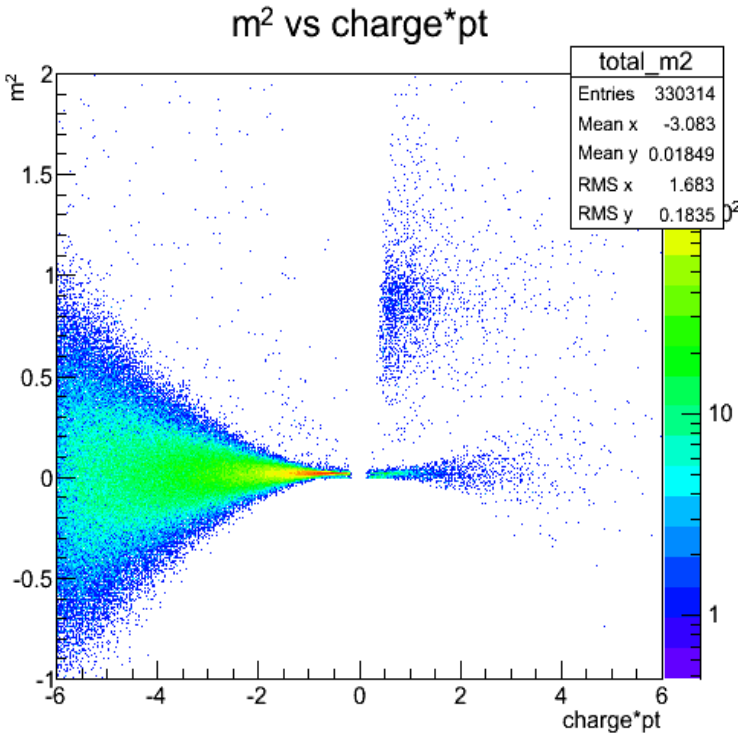

Figure 3.35: Mass^2 distribution from simulation when pions are used as input.

center of the detector and forms a half circle shape; and this is where the VTX detector is located. So these protons are knocked out from the VTX detector by the particles.

We tried to use the DCA2d cut to eliminate the knocked out protons, but it turns out that the simulation can not describe the ratio of protons eliminated by the cut, which means that we can not get an absolute efficiency correction from the simulation. So we give up the proton and only focus on anti-proton spectra.

After we extract the mean and sigma for different pt bins we will need to fit the sigma with the parametrization. The standard deviation of m^2 distribution can be parametrized by the angular resolution σ_α of the DC, the multiple scattering term,σ_{ms}, and the timing resolution σ_t in the following equation:

$$\sigma^2_{m^2} = \frac{\sigma^2_\alpha}{K^2}(4m^4p^2) + \frac{\sigma^2_{ms}}{K^2}(4m^4(1+\frac{m^2}{p^2})) + \frac{\sigma^2_t c^2}{L^2}(4p^2(m^2+p^2)) \tag{3.1}$$

Figure 3.37 shows the parametrization of particle identification band coming from different

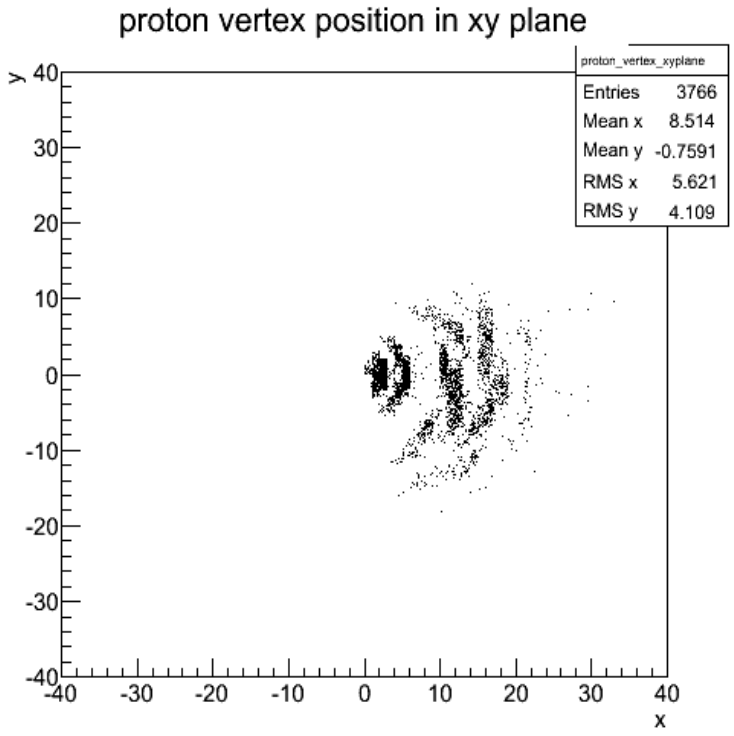

Figure 3.36: Proton vertex distribution from simulation.

sources, assuming σ_{TOF} = 120 ps. From this figure, we know that for protons and pions at high p_T, the main source of uncertainty comes from different components; for protons, it mainly comes from momentum resolution and timing resolution but for pions momentum resolution only contributes very little.

We fit our σ with this equation to extract the angular resolution, multiple sacttering term and the timing resolution. The fitted result is shown in Figure 3.40.

The particle is then identified as pions (kaons/protons) if that particle's mass falls into the 2 σ region of pions (kaons/protons) mean value.

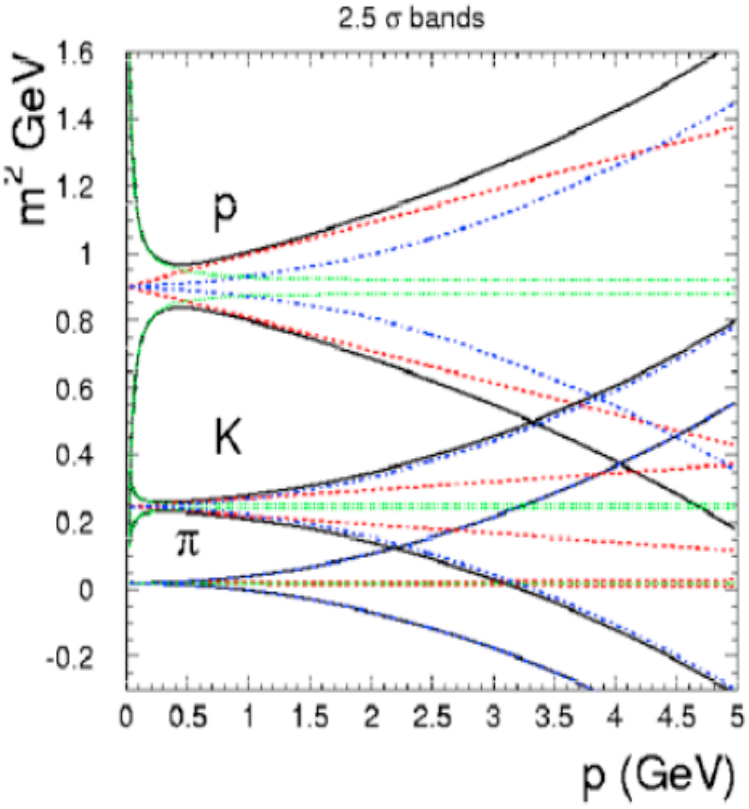

Figure 3.37: Parametrization of particle identification band. Contributions from different sources are in different colors: σ_{ms} (green) multiple scattering contribution, σ_{red} (red) momentum resolution, σ_{ttof} (blue) timing resolution.

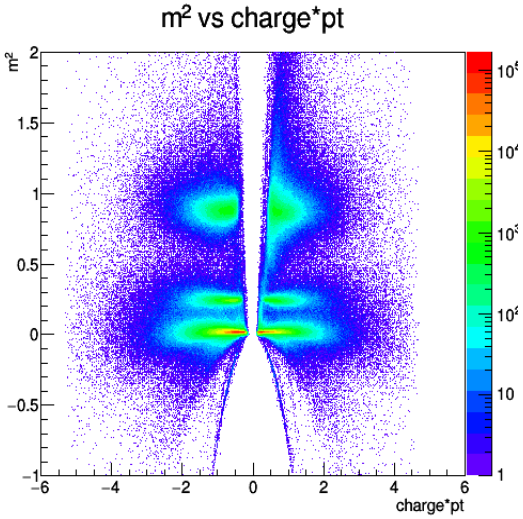

Figure 3.38: m^2 vs $charge \times pt$

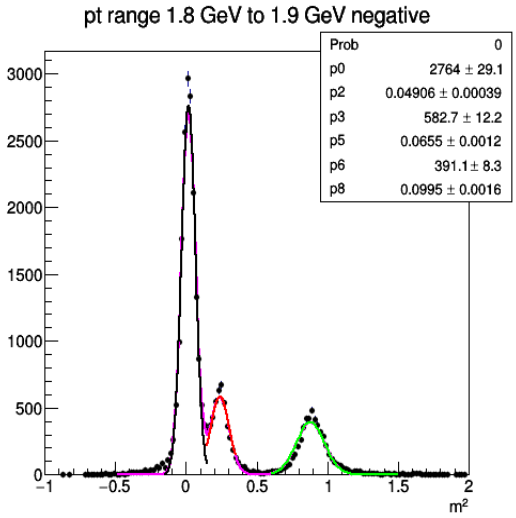

Figure 3.39: pt bin 1.8-1.9 GeV

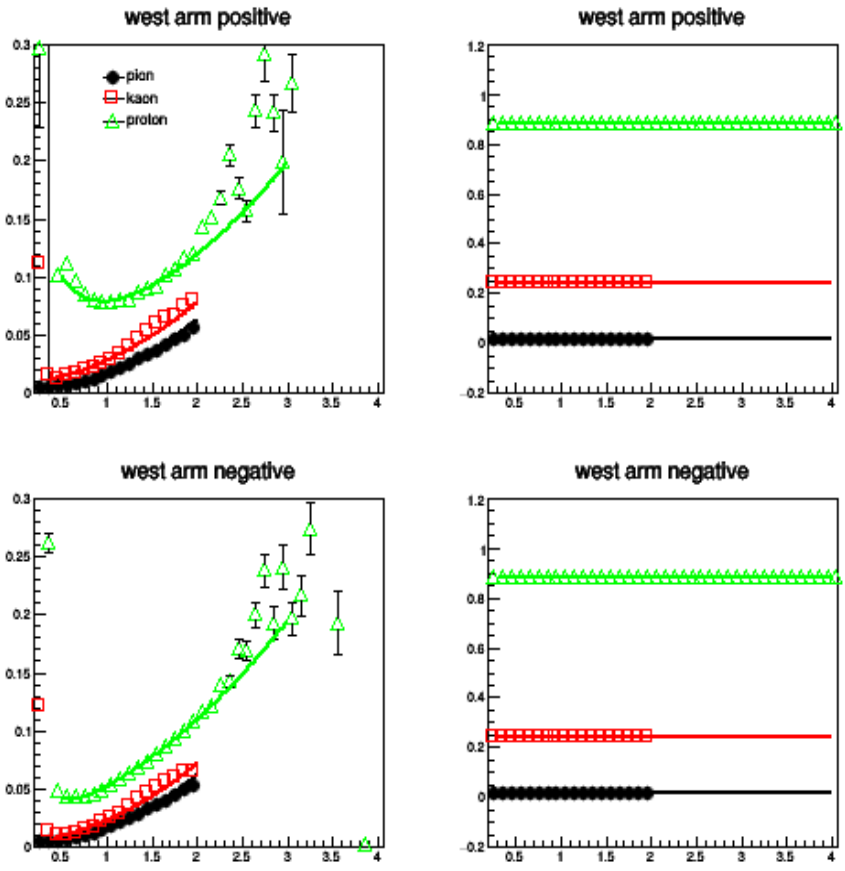

Figure 3.40: West arm σ and mean vs pt

3.5 Experimental Methods for Flow Measurement

As shown in figure 3.41, when a collision happened, if the impact parameter is not zero, the collision will generate a azimuthally anisotropic region. If QGP is formed, this region will evolve hydrodynamically, so the initial spatial anisotropy will generate azimuthally anisotropic pressure gradients that are stronger at the shorter dimension. This will result in a spatially anisotropic momentum distribution that is experimentally observable.

Experimentally, this is measured by expanding the momentum distribution as a Fourier series and measure its coefficient:

$$E\frac{d^3N}{dp^3} = \frac{1}{2\pi}\frac{d^2N}{p_T dp_T dy}(1 + \sum_{n=1}^{\infty} 2\upsilon_n cos[n(\phi - \Psi)]) \tag{3.2}$$

where υ_n measures the asymmetry of order n, Ψ is the reaction plane of the collision. In this analysis, we measure the second order coefficient, which is also called elliptic flow.

Experimentally, the reaction plane varies event by event and it is not possible to get this directly from experiment; so we need to make an approximate of it by another variable : the event plane. The event plane is determined by using all the produced particles, calculating their average plane and use that as a substitute for the reaction plane. However, in reality, there are finite produced particles and the detector have limited resolution, there is usually a shift between the event plane and the reaction plane. This need to be corrected by a factor called "event plane resolution".

To calculate the event plane, we need to calculate the flow vector in x and y direction and then calculate the event plane angle using the arctan function. The x and y flow vector component is calculated using the folloing formula:

$$Q_x = \sum_{i=1}^{N} w_i cos(n\phi_i), Q_y = \sum_{i=1}^{N} w_i sin(n\phi_i)$$

where N is the number of PMT hits in the BBC south arm, the weight factor is the charge deposited in each of the PMTs. The ϕ_i is the ϕ angle of the center position of each PMT.

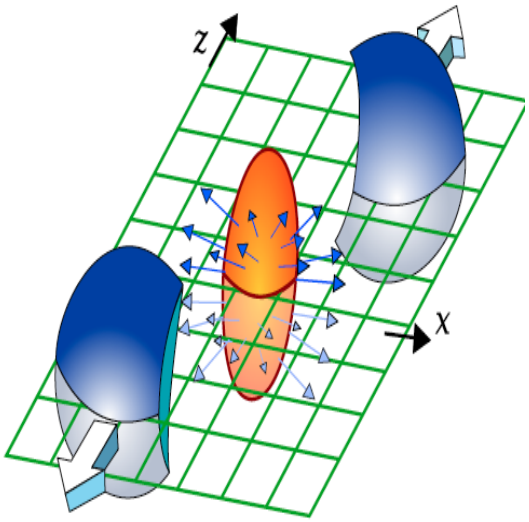

Figure 3.41: The picture showing the reaction plane in a nucleus-nucleus collision

Then the n_{th} harmonic event plane angle is calculated using

$$\Psi_n = atan(Q_y/Q_x) \tag{3.3}$$

After obtaining the event plane angle, the υ_n is extracted by

$$\upsilon_n = \frac{< cos(n(\phi - \Psi_{n,BBC_{south}}) >}{Res(\Psi_{n,BBC_{south}})} \tag{3.4}$$

where $Res(\Psi_{n,BBC_{south}})$ is the event plane resolution. In PHENIX, we usually use a three sub-events methods to determine the resolution using the follow formula:

$$Res(\Psi_{n,BBC_{south}}) =< cos(n(\Psi_{n,BBC_{south}} - \Psi_{RP})) >=$$

$$\sqrt{\frac{< cos(n(\Psi_{n,BBC_{south}} - \Psi_{n,CNT})) >< cos(n(\Psi_{n,BBC_{south}} - \Psi_{n,FVTXs})) >}{< cos(n(\Psi_{n,CNT} - \Psi_{n,FVTXs})) >}} \tag{3.5}$$

where $\Psi_{n,CNT}$ is the nth order event plane measured using the central arm detectors. Similarly,

$\Psi_{n,FVTXs}$ is the nth order event plane measured by forward silicon vertex detector located in the Au-going side (FVTXs). In this analysis, we used the results measured by FVTXs as the main results and use the other two to calculate the event plane resolution.

3.6 Corrections to Raw Spectra from Monte Carlo Simulation

To get the invariant yield from the raw spectra, we need to consider the efficiency of the detectors. First of all, the acceptance of the detector is not perfect, it only covers part of the $4\pi^2$ region. For PHENIX central arms specifically, it only covers π in azimuthal angle and 0.7 in rapidity region. Second, even in the regions that the detector covers, the efficiency of that part is 100%. Some part of the detector may be broken. So we need to make corrections to the raw spectra.

In this section, we will consider the method of calculating the efficiency using the single particle monte carlo simulation method. In next section we will consider another method, the bootstrap method. The basic steps of the simulation method are:

1. Produce some single particles using event generators. One details in this step is that the generated particle's distribution is flat in p_T and η, which is not the case in the real data. The reason for this is that in real data the spectra falls exponentially and if we generate an spectra like this; the particle at high p_T would be too less to calculate the efficiency.

2. Pass these single particles to PISA. PISA is short for PHENIX Integrated Simulation Application. PISA is the PHENIX simulation software package based on the GEANT3 libraries. It is used to simulate the particle interaction with the detector materials.

3. Track reconstruction from PISA to pisaTODST. The output of PISA is the hits file and we need to construct the hit information to tracks using the same package we used to reconstruct real data points.

4. Analysis the reconstructed tracks the same as in the data

5. Calculation of correction factors

Table 3.3: Simulation input parameters

Parameter	Value
Event type	single particle
p_T distribution	flat
p_T range	0.0 GeV/c $<$ p_T $<$ 10.0 GeV/c
rapidity range	-0.6 $<$ y $<$ 0.6
rapidity distribution	flat
z-vertex range	-10 cm $<$ z $<$ 10 cm
azimuth range	$-\pi$ $<$ ϕ $<$ π

The correction factors are determined by comparing the Exodus input to the final output of the analyzed simulated tracks. The efficiency can be determined by the following relation:

$$\frac{dN_{output}/dp_T}{dN_{input}/dp_T} = \epsilon_{acceptance}\epsilon_{efficiency}; \tag{3.6}$$

The correction factor is the inverse of this quantity:

$$F_C(p_T) = \frac{dN_{input}/dp_T}{dN_{output}/dp_T} \tag{3.7}$$

The true spectrum is the raw multiplied by the correction factor:

$$\frac{dN_{corrected}}{dp_T} = \frac{dN_{raw}}{dp_T}F_C(p_T) \tag{3.8}$$

Table 3.3 describes the parameters for our simulation. The generated particles have a flat distribution on p_T to ensure there are plenty particles at high p_T.Its distribution on rapidity, z-vertex and azimuth angle are also flat.

3.6.1 Drift Chamber Fiducial Map

After many years of running, not all regions of the detector are working well. When calculating the correction factor, we have to insure that the working area in the data and simulation are the same, which can be seen in 2-D phi vs alpha plot. Also, we need to make sure the detector

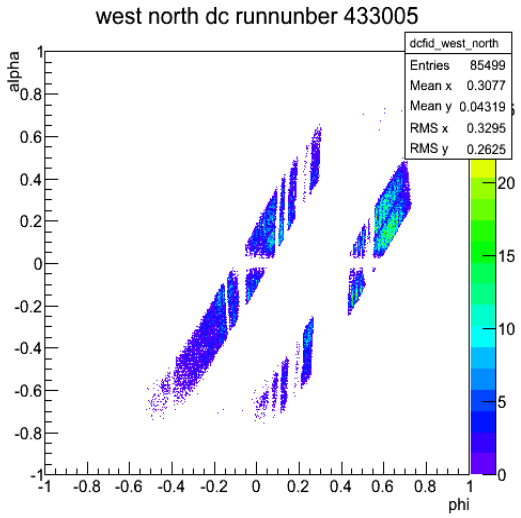

Figure 3.42: Fiducial map of DC for West arm for run 433005

efficiency at different p_T bins are the same as in the simulation, this can be seen in the 1-D DC phi distribution. If there are some area that are working in the simulation but not in the data, we will cut these part of area both in data and simulation.

As mentioned in the run selection section, we only use the east arm data because the there is a big hole in the West arm, which can be seen in the 2-D fiducial map. Figure 3.42 shows the fiducial map in West arm for run number 433005, we can see there is a big hole in the negative alpha region, which corresponds to positive tracks. And by looking at the fiducial maps run by run. We found that over 80% of runs have a big hole in West arm. So we decide to use East arm only. Another thought might be only look at the negative particle in the West arm since from the 2-D fiducial map it seems the negative part of West arm is ok. But we will see shortly that even this is feasible because the 1-D phi response is very different in data and simulation. Also, there is another question, that is the simulation can not really simulate the big efficiency gap between East and West arm in data.

Figure 3.43 and 3.44 shows the Drift Chamber fiducial map comparison in East arm between data and simulation, one for south arm and one for north arm. In each of the figures, the left part shows the fiducial map in data and the right part shows the fiducial map in simulation. From the comparison we find that the fiducial map for data and simulation do not agree so well. The

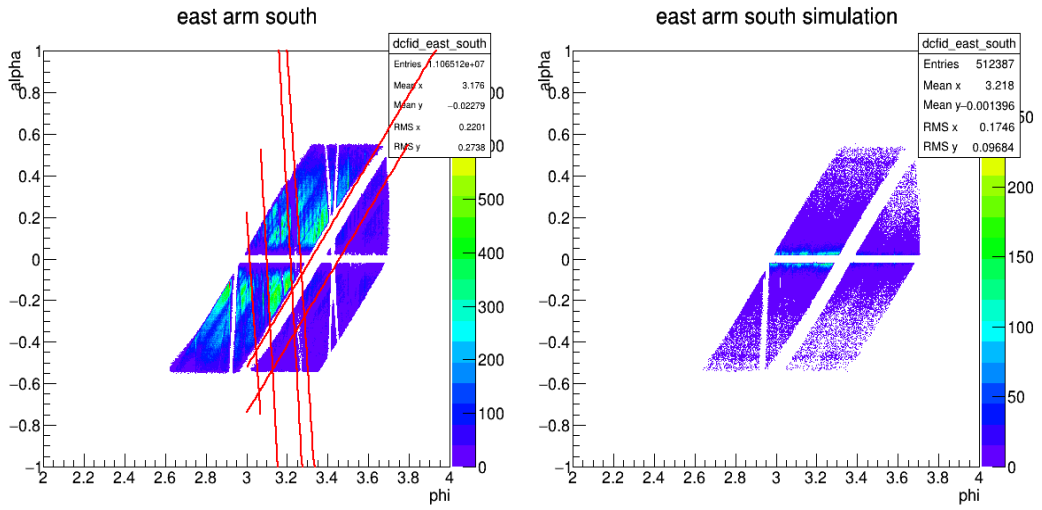

Figure 3.43: Fiducial map of DC for east arm south in data and simulation

detector has many bad regions that do not work well so we employ some cuts. The red line shown in the figure is the cut we applied.

Figure 3.45 and 3.46 shows the fiducial map in data and simulation after the cut.

3.6.2 Drift Chamber 1-D phi Distribution

Having looked at the 2-D distribution of phi vs alpha for DC, we may want to take a closer look at the 1-D phi distribution in data and simulation to see if their response is close enough. In order to get the closest match, we use a very narrow bin width : 0.1 GeV. We show all the combination of track charge and DC side (south and north). Only a few p_T bins are shown since there are too many in total. For East arm, we showed the 1-D phi distribution for 0.6 GeV $< p_T <$ 0.7 GeV and 1.6 GeV $< p_T <$ 1.7 GeV for south and north arm and before and after fiducial cut. For West arm, we showed the 1-D phi distribution for 0.8-0.9 GeV before and after fiducial cut.

From these figures we noticed that after the fiducial cut, the 1-D phi distribution for East arm between data and simulation becomes more similar. However, this is not true for West arm. We observed that even after ficucial cut, there is still a big difference from data and simulation. This is the reason that we can only use East arm.

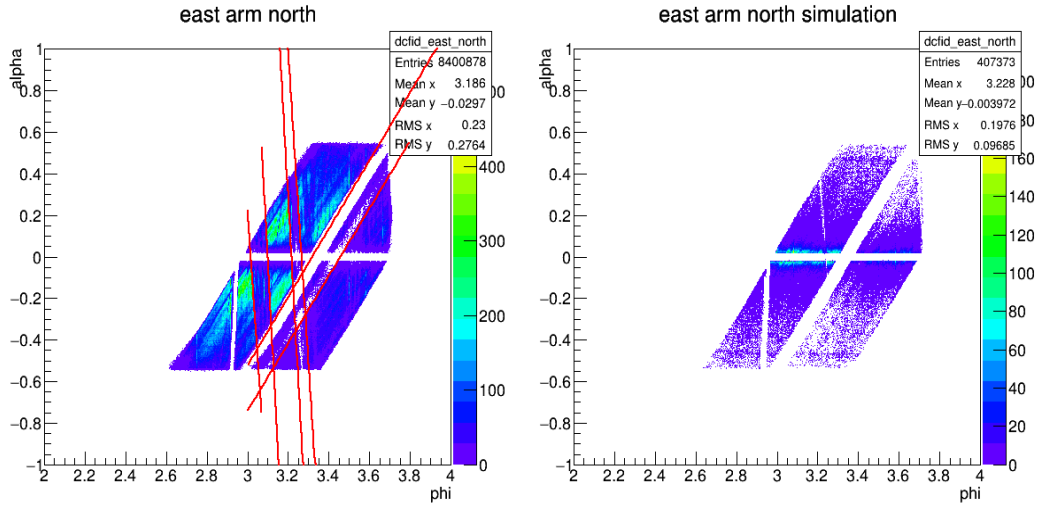

Figure 3.44: Fiducial map of DC for East arm- North in data and simulation

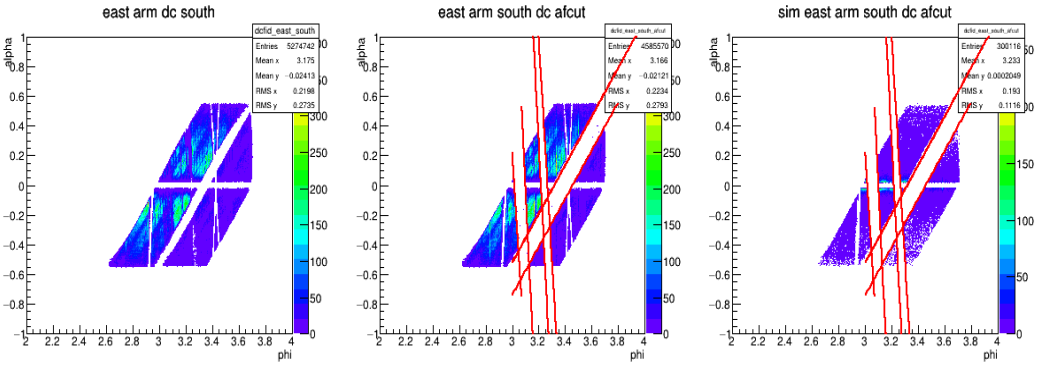

Figure 3.45: Fiducial map of DC for East arm -South in data and simulation

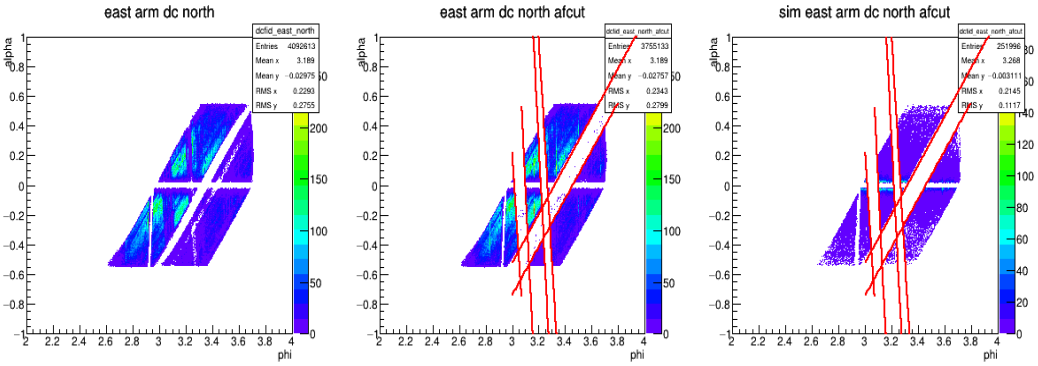

Figure 3.46: Fiducial map of DC for East arm south in data and simulation

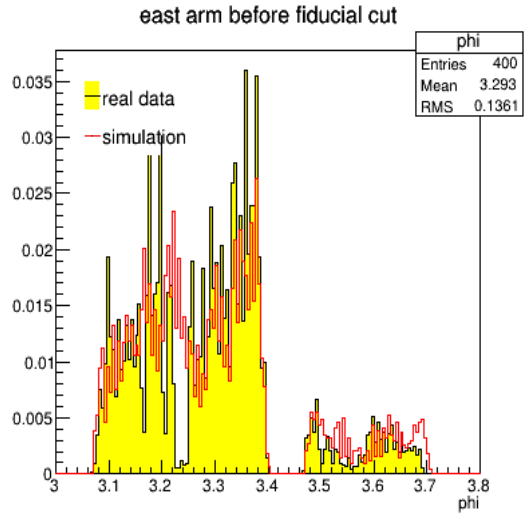

Figure 3.47: DC phi, negative charge, negative zed for p_T range 0.6 - 0.7 GeV before fiduical cut

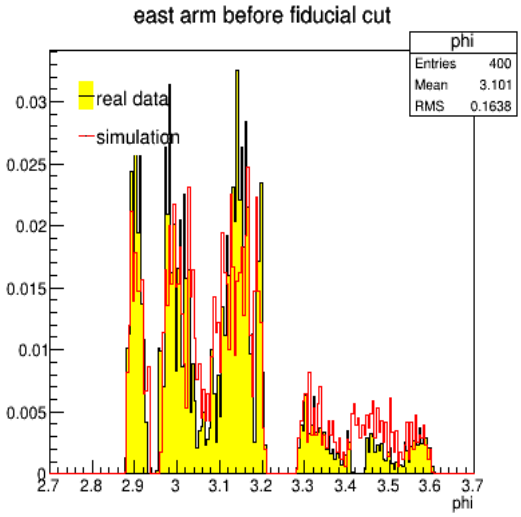

Figure 3.48: DC phi, negative charge, positive zed for p_T range 0.6 - 0.7 GeV before fiduical cut

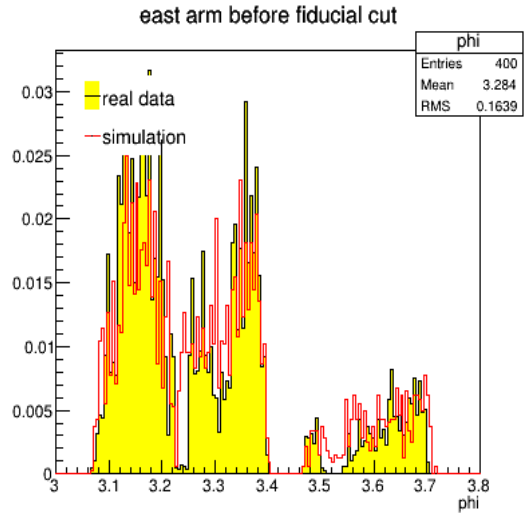

Figure 3.49: DC phi, positive charge, negative zed for p_T range 0.6 - 0.7 GeV before fiduical cut

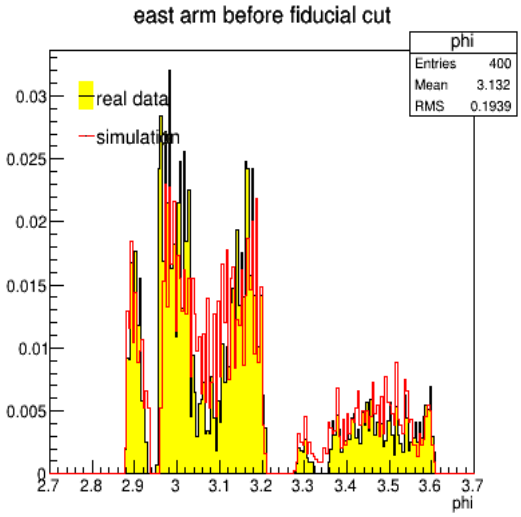

Figure 3.50: DC phi, positive charge, positive zed for p_T range 0.6 - 0.7 GeV before fiduical cut

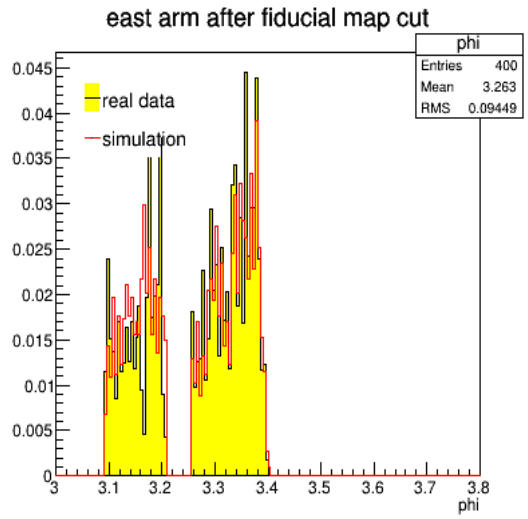

Figure 3.51: DC phi, negative charge, negative zed for p_T range 0.6 - 0.7 GeV after fiduical cut

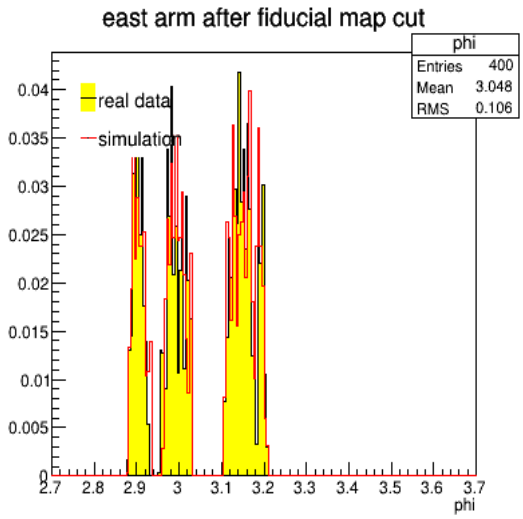

Figure 3.52: DC phi, negative charge, positive zed for p_T range 0.6 - 0.7 GeV after fiduical cut

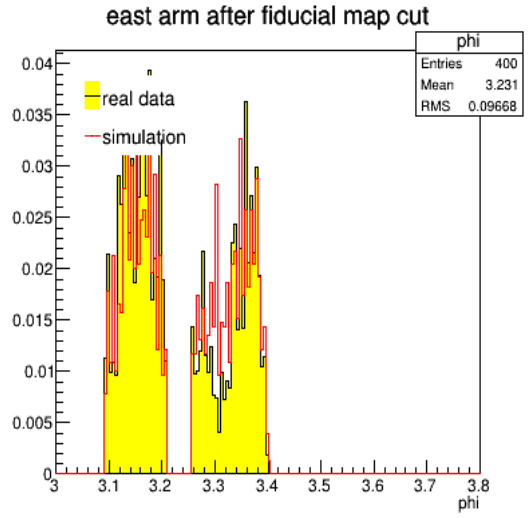

Figure 3.53: DC phi, positive charge, negative zed for p_T range 0.6 - 0.7 GeV after fiduical cut

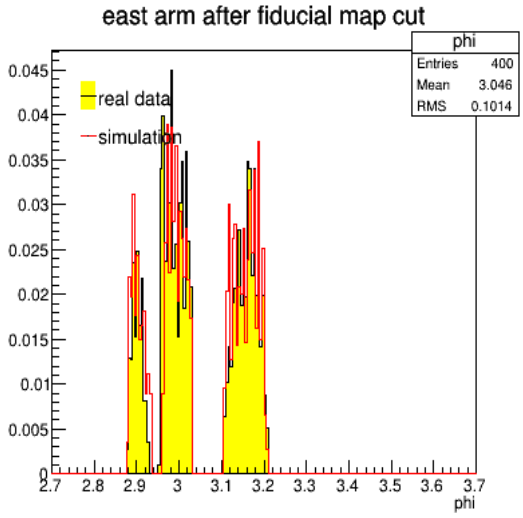

Figure 3.54: DC phi, positive charge, positive zed for p_T range 0.6 - 0.7 GeV after fiduical cut

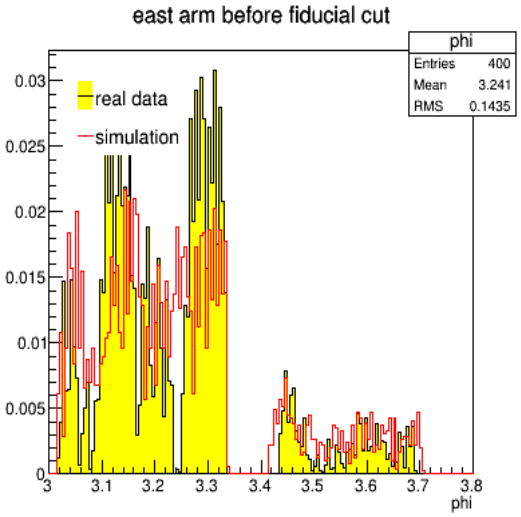

Figure 3.55: DC phi, negative charge, negative zed for p_T range 1.6 - 1.7 GeV before fiduical cut

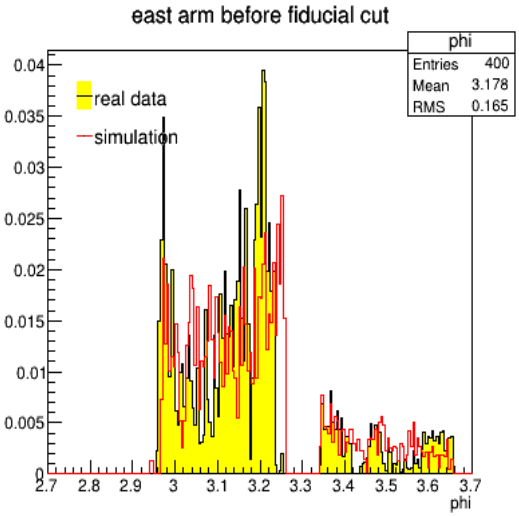

Figure 3.56: DC phi, negative charge, positive zed for p_T range 1.6 - 1.7 GeV before fiduical cut

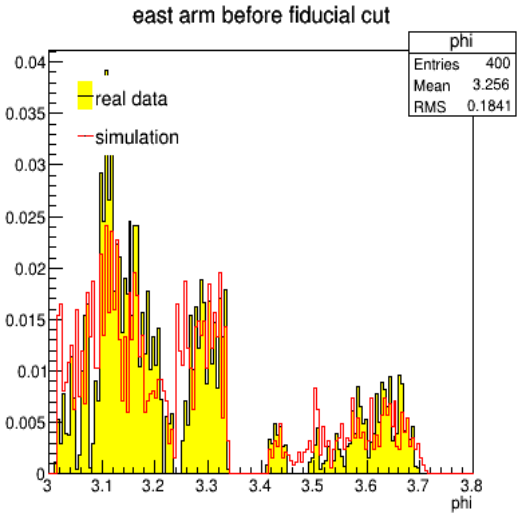

Figure 3.57: DC phi, positive charge, negative zed for p_T range 1.6 - 1.7 GeV before fiduical cut

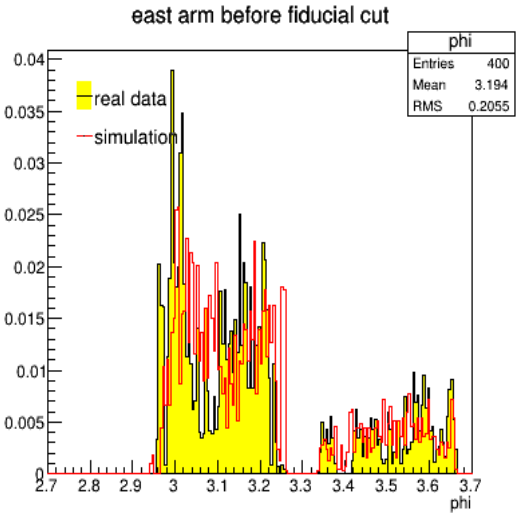

Figure 3.58: DC phi, positive charge, positive zed for p_T range 1.6 - 1.7 GeV before fiduical cut

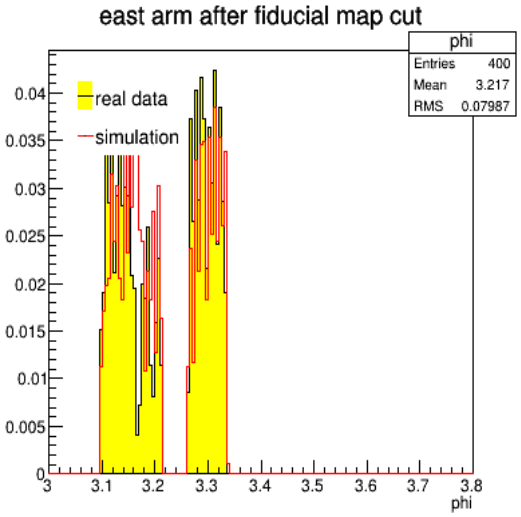

Figure 3.59: DC phi, negative charge, negative zed for p_T range 1.6 - 1.7 GeV after fiduical cut

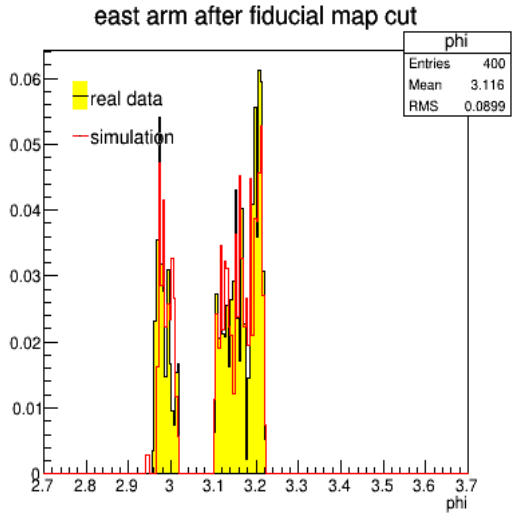

Figure 3.60: DC phi, negative charge, positive zed for p_T range 1.6 - 1.7 GeV after fiduical cut

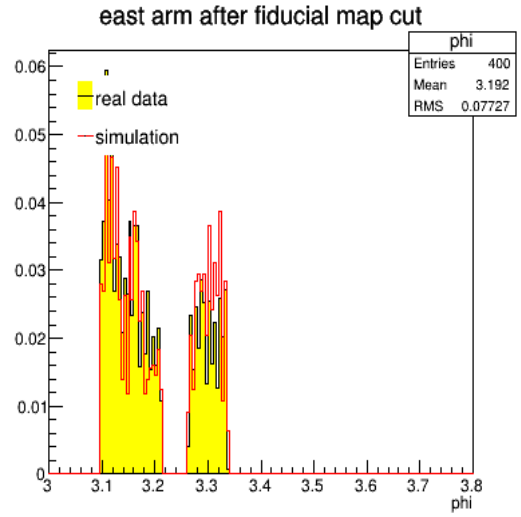

Figure 3.61: DC phi, positive charge, negative zed for p_T range 1.6 - 1.7 GeV after fiduical cut

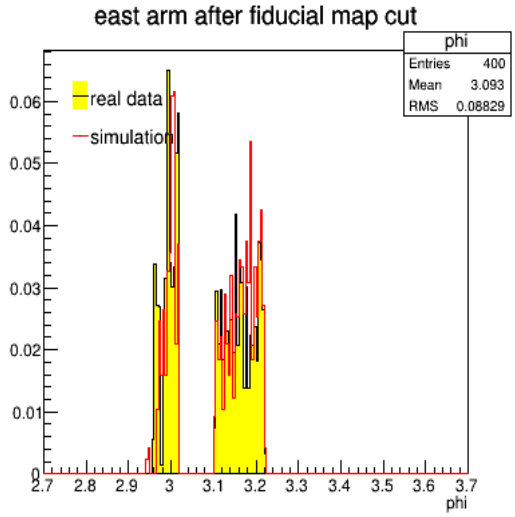

Figure 3.62: DC phi, positive charge, positive zed for p_T range 1.6 - 1.7 GeV after fiduical cut

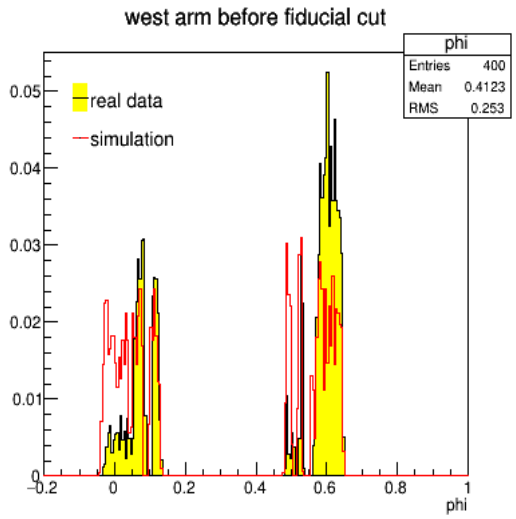

Figure 3.63: DC phi, negative charge, negative zed for p_T range 0.8 - 0.9 GeV before fiduical cut

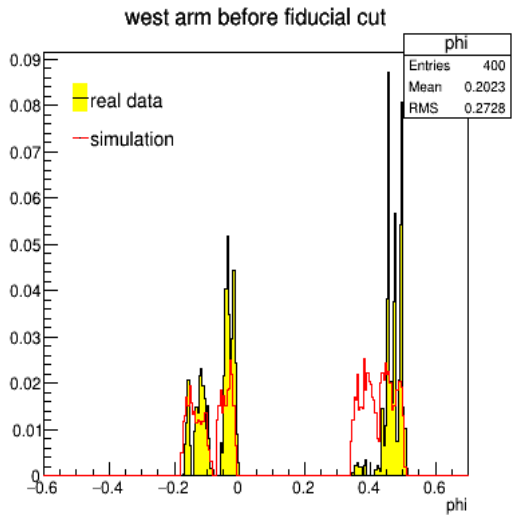

Figure 3.64: DC phi, negative charge, positive zed for p_T range 0.8 - 0.9 GeV before fiduical cut

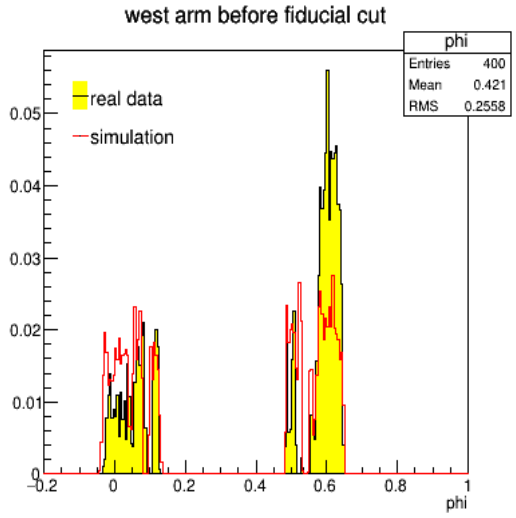

Figure 3.65: DC phi, positive charge, negative zed for p_T range 0.8 - 0.9 GeV before fiduical cut

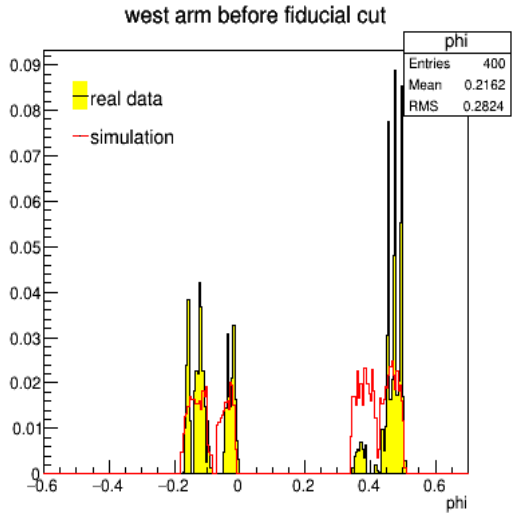

Figure 3.66: DC phi, positive charge, positive zed for p_T range 0.8 - 0.9 GeV before fiduical cut

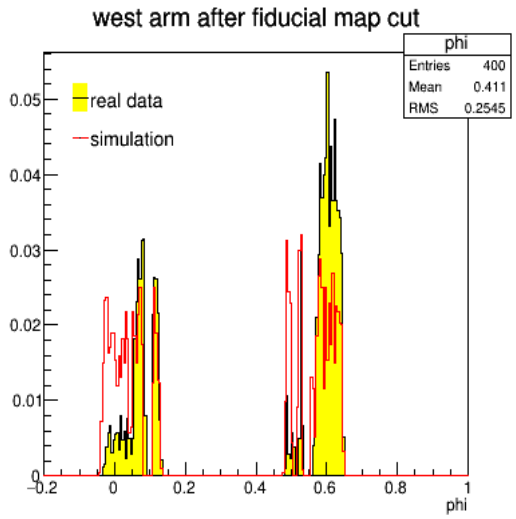

Figure 3.67: DC phi, negative charge, negative zed for p_T range 0.8 - 0.9 GeV after fiduical cut

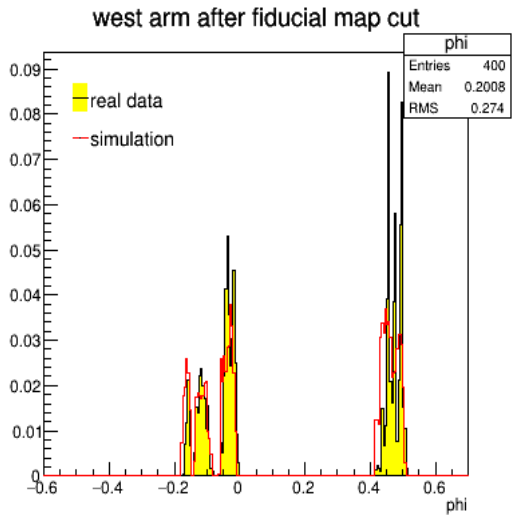

Figure 3.68: DC phi, negative charge, positive zed for p_T range 0.8 - 0.9 GeV after fiduical cut

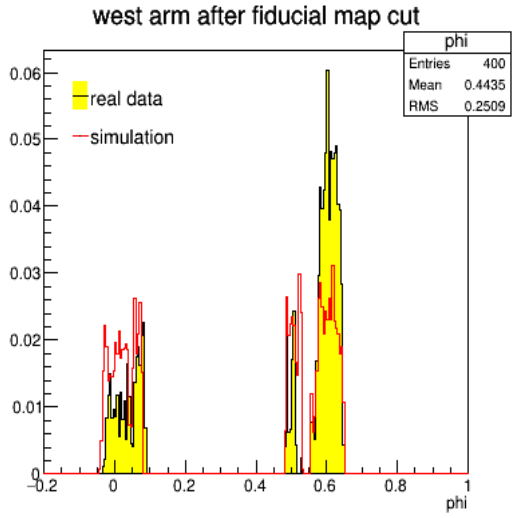

Figure 3.69: DC phi, positive charge, negative zed for p_T range 0.8 - 0.9 GeV after fiduical cut

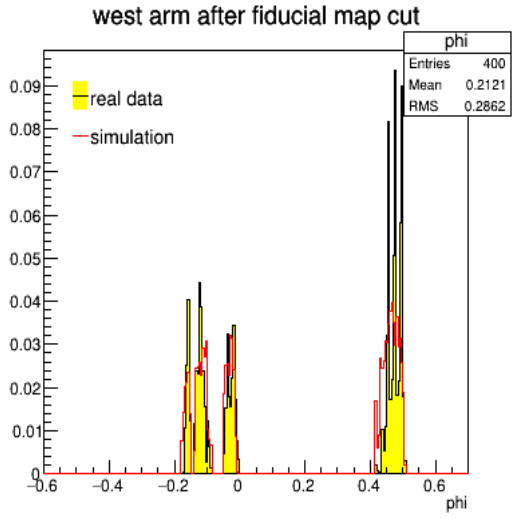

Figure 3.70: DC phi, positive charge, positive zed for p_T range 0.8 - 0.9 GeV after fiduical cut

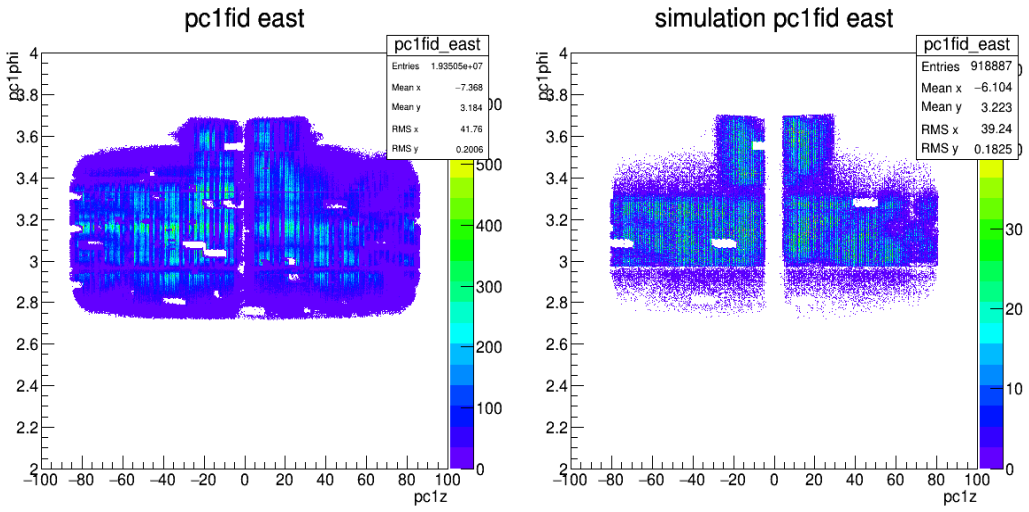

Figure 3.71: Fiducial map of PC1 for East arm in data and simulation

3.6.3 Fiducial Map in Pad Chamber

Similar to the fiducial map in Drift Chamber, in this section we show the fiducial map in PC1 and PC3 and the cut we applied.

Figure 3.71 and figure 3.72 shows the fiducial map for East arm pc1 and PC3 in data and simulation. The following two figures, figure 3.73 and figure 3.74 shows the fiducial map after the cut. The axis for PC fiducial map is the z position measured by PC and y axis is the azimuth phi angle measured by PC. The left plot of figure 3.71 and 3.72 shows the fiducial map for data; the right shows the fiducial map for simulation. The left plot of figure 3.73 and 3.74 shows the fiducial map for data before cut; the middle shows the fiducial map for data after cut; the right shows the fiducial map for simulation after cut.

From these figures we see that there are many regions in the detector are bad and the simulation can not match; so we cut some regions both in data and simulation to make them as similar as possible.

3.6.4 PID Function in Real Data and Simulation

In simulation, the timing resolution is a little bit higher than in the real data, which makes the PID band a little narrower than in the data. In order to match real data, the TOF time in simulation

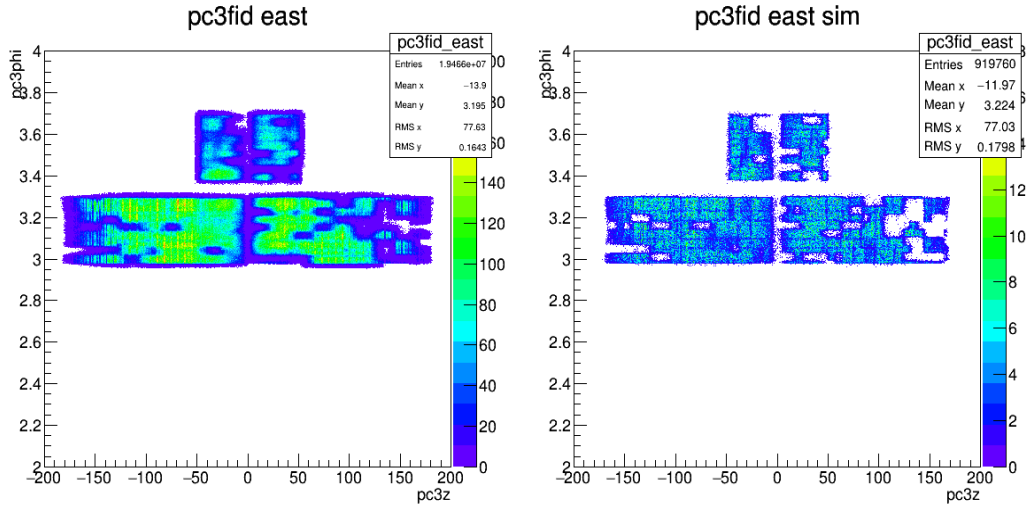

Figure 3.72: Fiducial map of PC3 for East arm in data and simulation

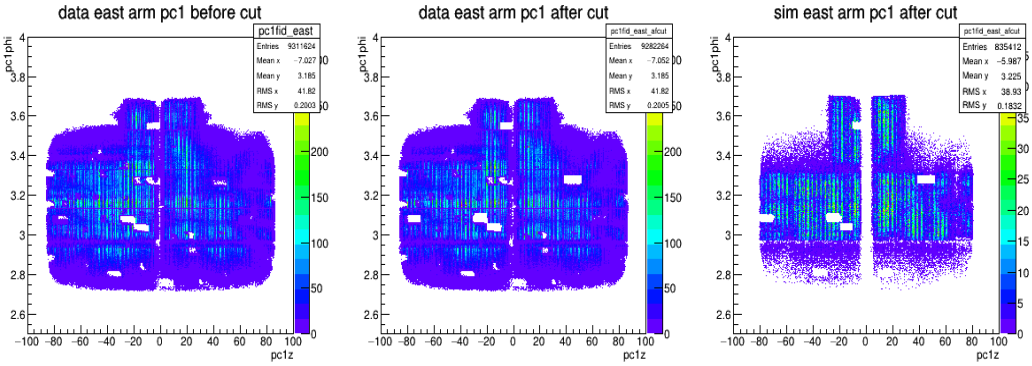

Figure 3.73: Fiducial map of PC1 for east arm in data and simulation after cut

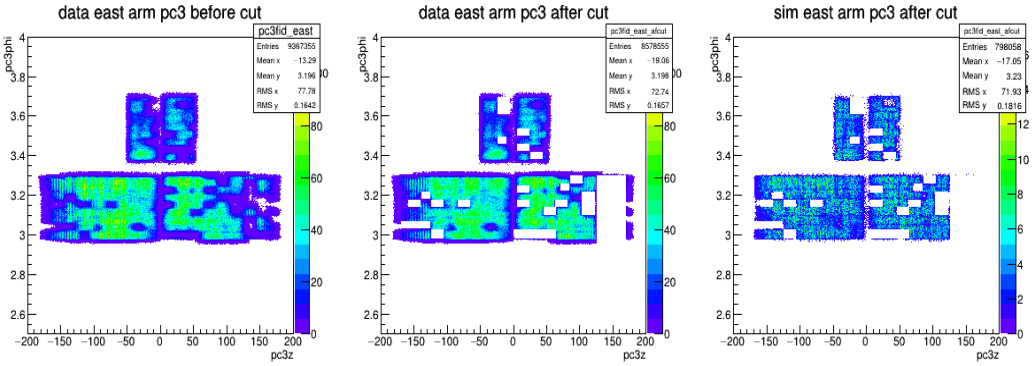

Figure 3.74: Fiducial map of PC3 for East arm in data and simulation after cut

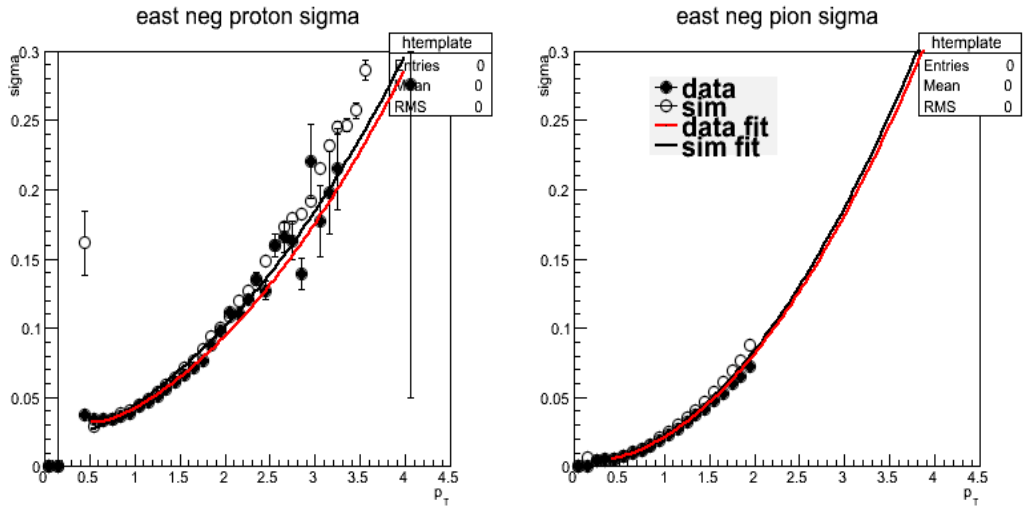

Figure 3.75: PID function of π^- and anti-proton in real and simulation in East arm

is smeared with a Gaussian function and recalculated. After the smearing, the PID function for protons and pions in real data and in simulation is plotted in Figure 3.75 and Figure 3.76. From the comparison we can say that the PID band for proton and pion agree very well in data and in simulation.

3.6.5 Plots of the Correction Factor

After we got the PID band for simulation, we can calculate the raw spectra from simulation and then calculate the correction factor by dividing the simulation input by the raw spectra in simulation. The plots of the correction factor for pions and protons are shown in figure 3.77 and 3.78.

3.6.6 Weak Decay Feeddown Correction for Protons

We need a special correction for protons, since there are a lot of protons comes from weak decay of hyperons such as lambdas. To calculate the fraction of protons that come from weak decay from hyperons, mostly lambda, we also generate lambdas and use these lambdas as input for the simulation and see how many protons we get in the detector. We then compare the number of protons that fall into the PID band after reconstruction weight by a factor : $W(p_T) = p_T^{\Lambda} e^{(m_T^{\Lambda} - m_0^{\Lambda})/T}$.

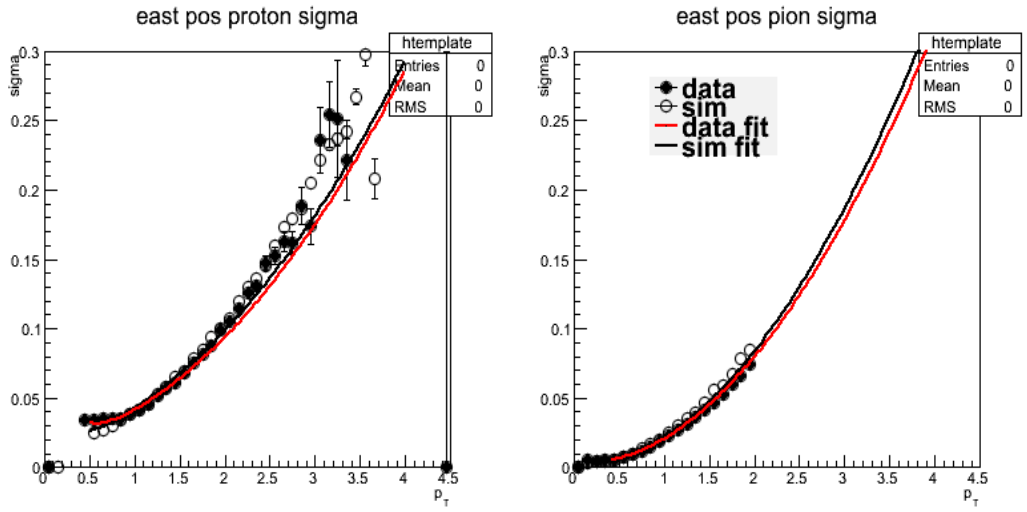

Figure 3.76: PID function of pion and proton in real and simulation in East arm

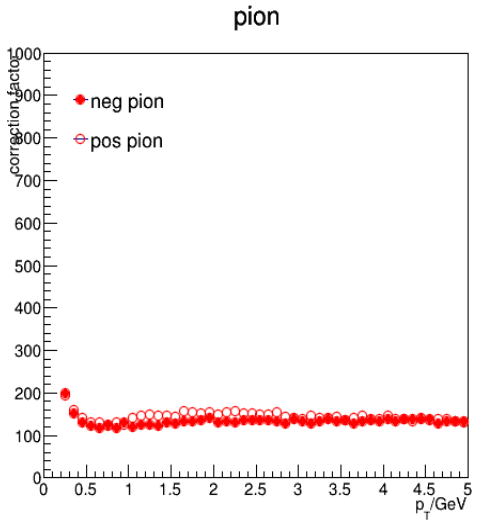

Figure 3.77: correction factors for pions in East arm

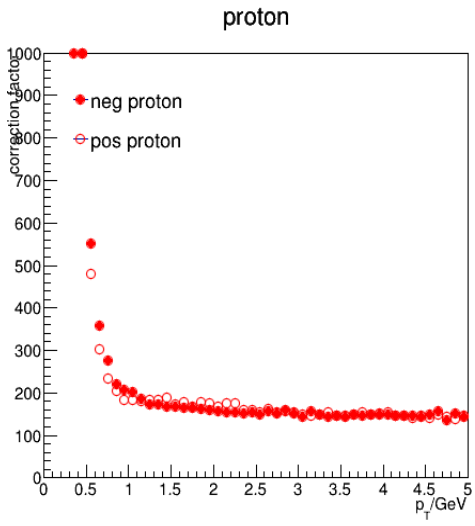

Figure 3.78: correction factor for protons in East arm

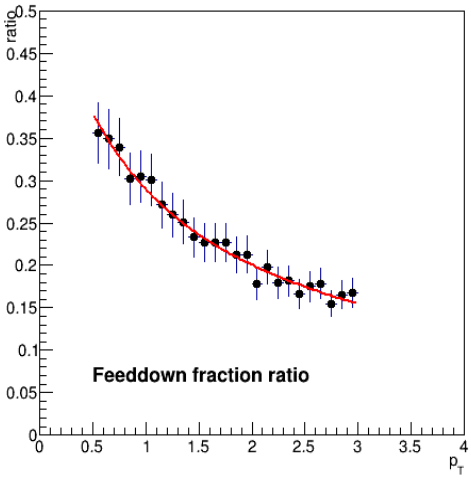

Figure 3.79: Feeddown fraction

We then compare the number of real protons that fall into the PID band and compare it to the lambda simulation result and get the ratio of feeddown proton. The resulting faction is shown in figure 3.79, the red line is a function fitted to the ratio and used to smooth the ratio.

3.7 Correction Factor from Bootstrap from Spectra Previously Measured in pp Collisions

When using the correction factor obtained above using the single particle simulation method, we found some inconsistency in the results. More specifically, the anti-proton over negative pion ratio in the most peripheral bin is too high compared to the measurement in pp collisions, but the results should be similar when the proton hits the edge of the gold nucleus. That is what we observed in dAu collisions; since dAu collisions is very similar to pAu collisions, we did not expect pAu have a big difference from dAu results. This indicates that there is some systematic effect that we do not understand completely and is not modeled in our simulation.

So, we tried another method to get the efficiency, that is what is going to be described below. In year 2015 there is also a pp run, and PHENIX has published measurements of indetified particle spectra in pp collisions from 2005. The spectra of these particles should not dependend on the year in which the collisions were measured. Therefore, we can obtain the efficiency and acceptance correction by comparing the uncorrected spectra measured in the pp portion of Run 15 to the published spectra from 2005, and then apply the same correction to the pAu portion of the run. In this section we will show the correction factor obtained this way and compare this result to the correction factor obtained from the simulation. The formula to calculate the invariant yield is as follows:

$$\frac{1}{2\pi p_T}\frac{d^2N}{dp_T d\eta} = \frac{1}{2\pi p_T} \times \frac{\Delta N_{data}}{\Delta p_T \Delta \eta} \times \frac{1}{N_{evt}^{data}} \times \frac{1}{\varepsilon_{acc\times eff}} \times \frac{1}{\varepsilon_{trig}} \times \frac{1}{biasfactor} \tag{3.9}$$

where $\varepsilon_{trig} = 0.79/0.55$, and $biasfactor$ is the bias factor in pAu collisions in the selected centrality class. Since in p+p collisions, not all events are captured by the minimum bias trigger, the fraction of events that satisfy the trigger is 79%; so the invariant yield must be corrected up by dividing the yield by this factor. In addition to the effect described above, we must also account for the factor that the MB trigger is biased towards events with coincident high-pT particles at midrapidity, since these are events with a higher multiplicity. The measured invariant yield should be corrected down to account for this bias, multiplying by 0.55.

From the above formula, we noticed that in order to obtain the efficiency factor $\varepsilon_{acc\times eff}$, we need to divide the invariant yield by all other factors. Another thing to notice is that pion spectra published from Run5 p+p collisions are expressed in units of cross section, and we need to turn them into invariant yields. Since the total inelastic cross section is 42 mb, we also need to multiply this factor.

We will also show two methods of calculate anti-proton spectra: one is bootstrap directly from previous anti-proton spectra; the other is trying to obtain the proton efficiency from the bootstrapped pion efficiency and the different factor for pions and protons when converting from rapidity to pseudorapidity.

3.7.1 Run Selection in pp Collisions

To select runs in pp collisions, we plotted the negative pion run by run variations for all the runs in Run15 pp collisions. Shown in Fig. 3.80 is the ratio of negative pion spectra in run number 421989 to the negative pions measured in all runs together; the ratio is fitted with a line. This process is done for every run and all the fitted value is plotted in Fig. 3.81. One thing to note is that I started the run number with 0 instead with the long number for better show the x axis, the runs are numbered according the actual run numbers. From this figure, we noticed that the run-by-run variance is pretty large, up to 30%. In addition, there is a rising trend in the first 100 runs. To try to reduce the uncertainty introduced by the run-by-run variations in pp collisions, we only selected the runs which fitted value is between 0.95 to 1.05 and excluded the first 100 runs. Using this method, we selected 248 runs from around 800 runs. This selection also limits the uncertainty due to variations in luminosity and double interactions in the same bunch crossing.

3.7.2 DC Phi Response in pAu and pp

We plan to use the bootstrapped correction factor obtained form pp for the pAu data. We are assuming that the during the same year run, the efficiency of the detector is the same for pp collision and pAu collision; this have some sense in it, since when calculating the efficiency from the simulation we are using single particle as input for both pp and pAu collision. One thing

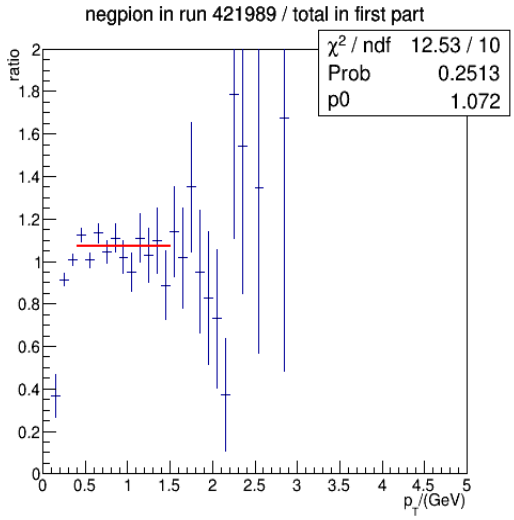

Figure 3.80: Run15 pp raw negative pion spectrum measured in Run 421989 divided by the spectrum from all runs.

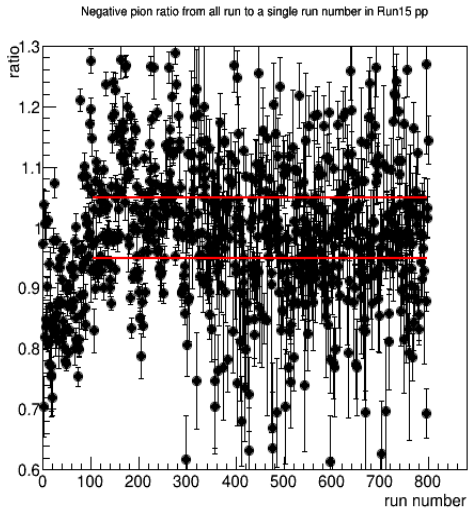

Figure 3.81: Run15 pp: run-by-run variation in the negative pion spectra.

that changes every year is the detector configuration file that is used as part of the input for the simulation; for the same year, we do not expect the detector will have big variations. But to be more sure about this, we will do some comparisons between the pp and pAu dataset. The first thing we will compare is the Drift Chamber 1-d phi response.

Figure 3.82, 3.83, 3.84, and 3.85 shows the comparison of 1-D phi distribution between run15pp and run15pAu for p_T range between 1.6 GeV to 1.7 GeV before fiducial cut. Figure 3.86, 3.87, 3.88, and 3.89 shows the same thing after fiducial cut.

We can see from these figures that the 1-D phi response for pp data and pAu data are very similar both before the fiducial cut and after the cut. This gives us the confidence for using the efficiency from pp to pAu.

3.7.3 DC and PC fiducial map in pp and pAu

The next thing we want to have a look at is the 2-D fiducial map in pp and pAu. Figure 3.90, 3.91, 3.92 and 3.93 shows the comparison of fiducial maps between pp and pAu data for Drift Chamber and Pad Chambers. On each one of this figures, the left one is for pAu and the right one is for pp. We can see in pp and pAu the patterns are very similar.

3.7.4 PID Cut in pp and in pAu

In this section, we will show the PID cut in pp and pAu collisions. The mass-squared plot for pAu and pp are shown in Figs. 3.94, 3.95. In these two figures, the protons are not flat as the one previous shown because DCA2d cut is applied and the protons come from the background is mostly removed. We are not using this for efficiency correction since this is not reproduced well in the simulation; we only use this cut to derive the true PID band. From the figure we see that the cut for pions is very wide at p_T greater than 2 GeV, which will contain a lot of kaon contamination. To eliminate the kaon contamination, we will count only the pion below the mean value and then multiply by a factor of two. When calculating the correction factor for pions, we used this method both for pions in pp and pAu to be consistent.

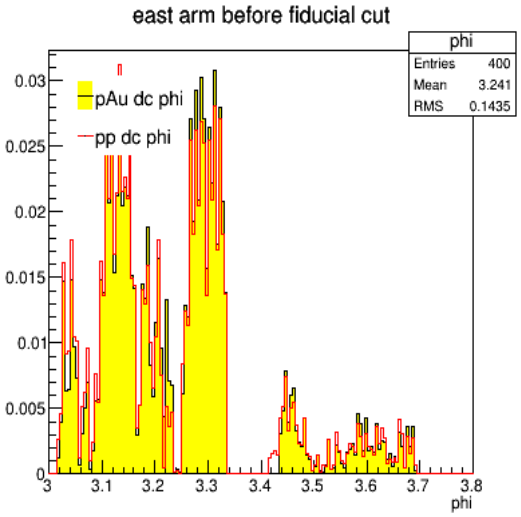

Figure 3.82: DC phi, negative charge, negative zed for p_T range 1.6 - 1.7 GeV before fiduical cut

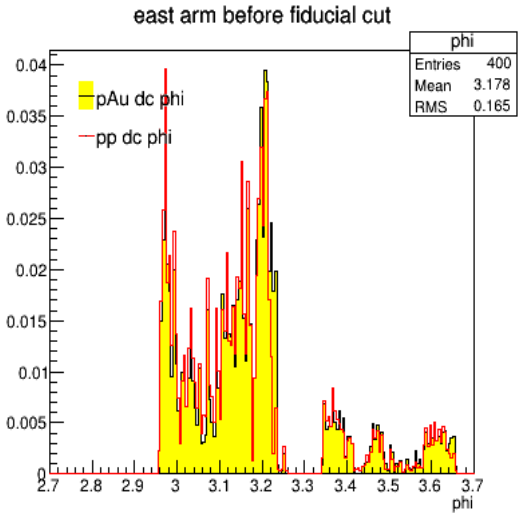

Figure 3.83: DC phi, negative charge, positive zed for p_T range 1.6 - 1.7 GeV before fiduical cut

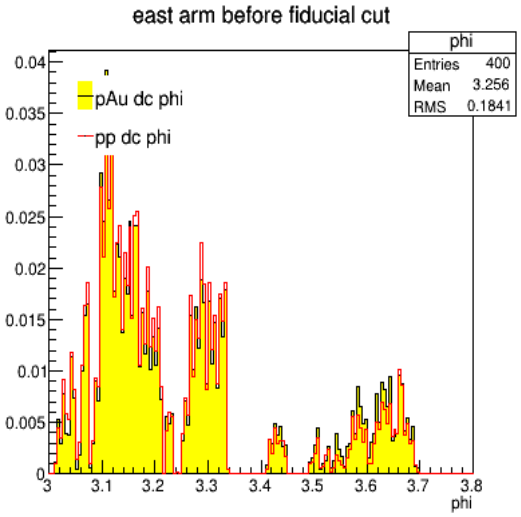

Figure 3.84: DC phi, positive charge, negative zed for p_T range 1.6 - 1.7 GeV before fiduical cut

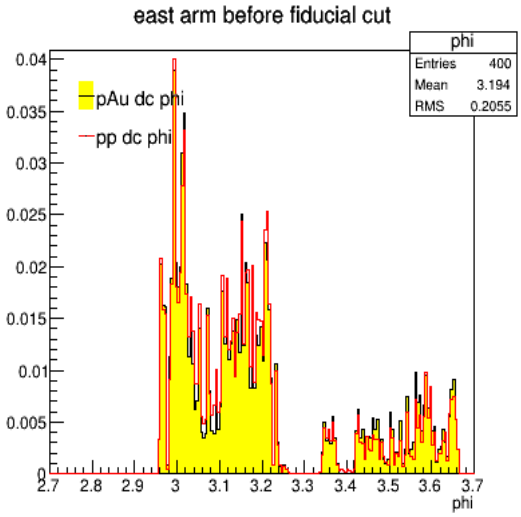

Figure 3.85: DC phi, positive charge, positive zed for p_T range 1.6 - 1.7 GeV before fiduical cut

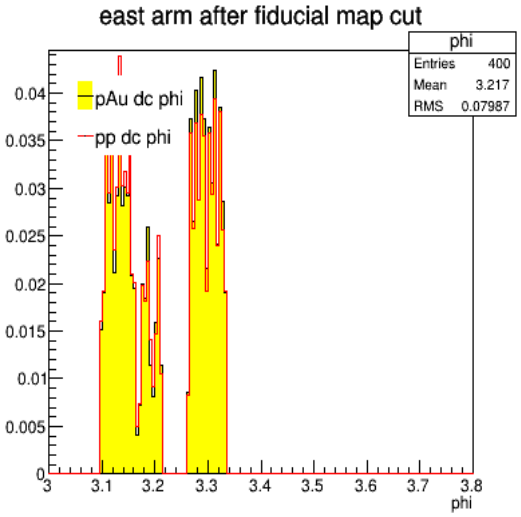

Figure 3.86: DC phi, negative charge, negative zed for p_T range 1.6 - 1.7 GeV after fiduical cut

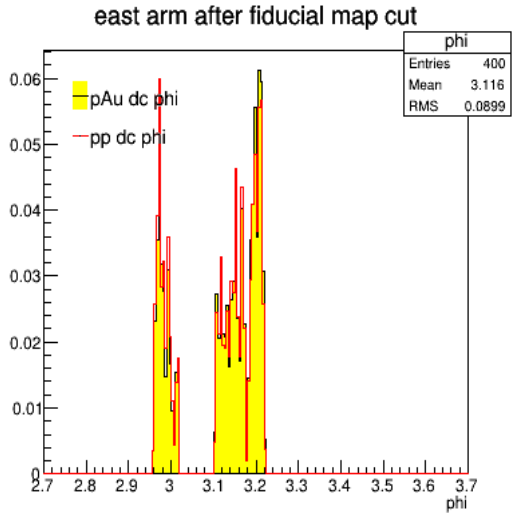

Figure 3.87: DC phi, negative charge, positive zed for p_T range 1.6 - 1.7 GeV after fiduical cut

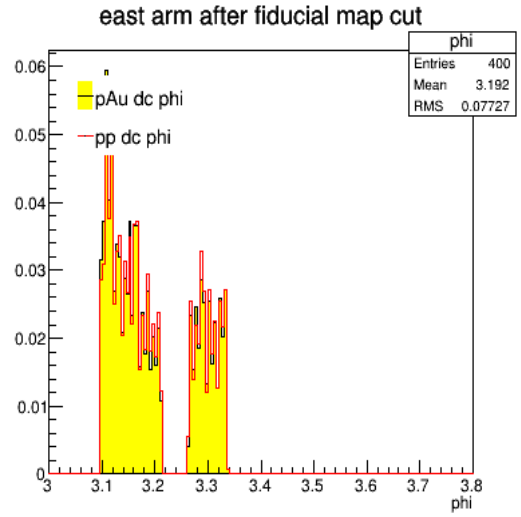

Figure 3.88: DC phi, positive charge, negative zed for p_T range 1.6 - 1.7 GeV after fiduical cut

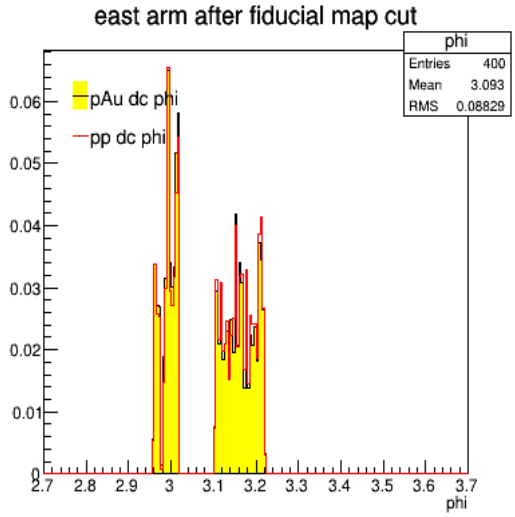

Figure 3.89: DC phi, positive charge, positive zed for p_T range 1.6 - 1.7 GeV after fiduical cut

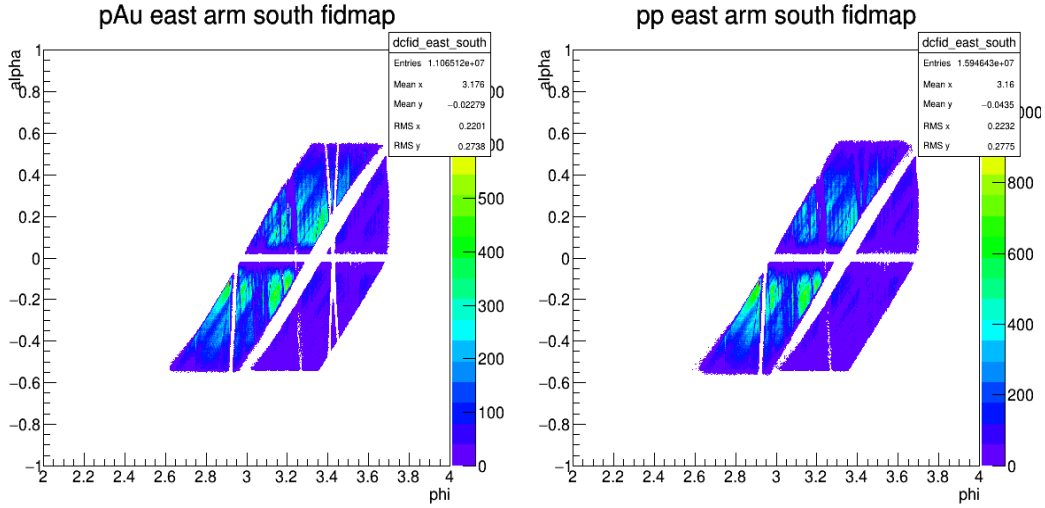

Figure 3.90: Fiducial map of DC for East arm -South in pp and pAu

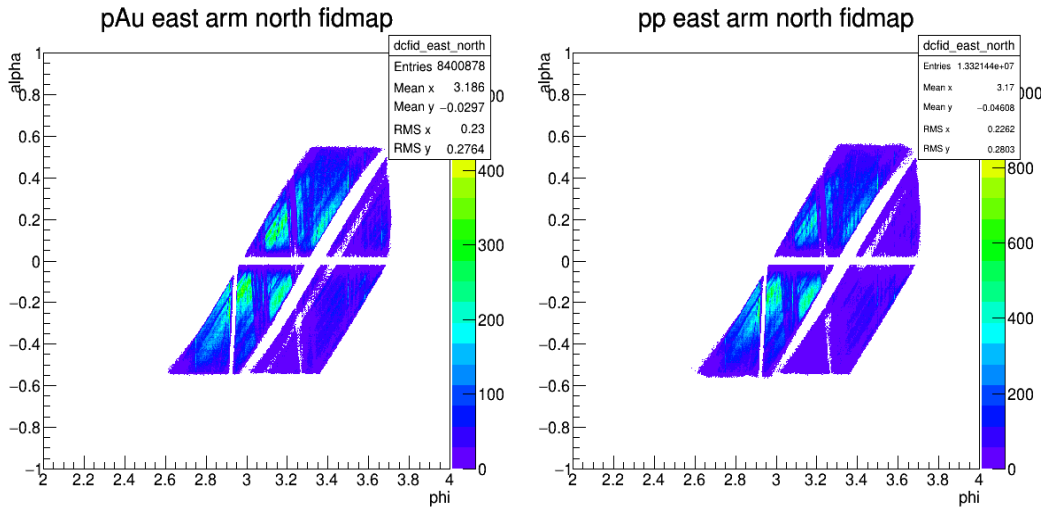

Figure 3.91: Fiducial map of DC for East arm North in pp and pAu

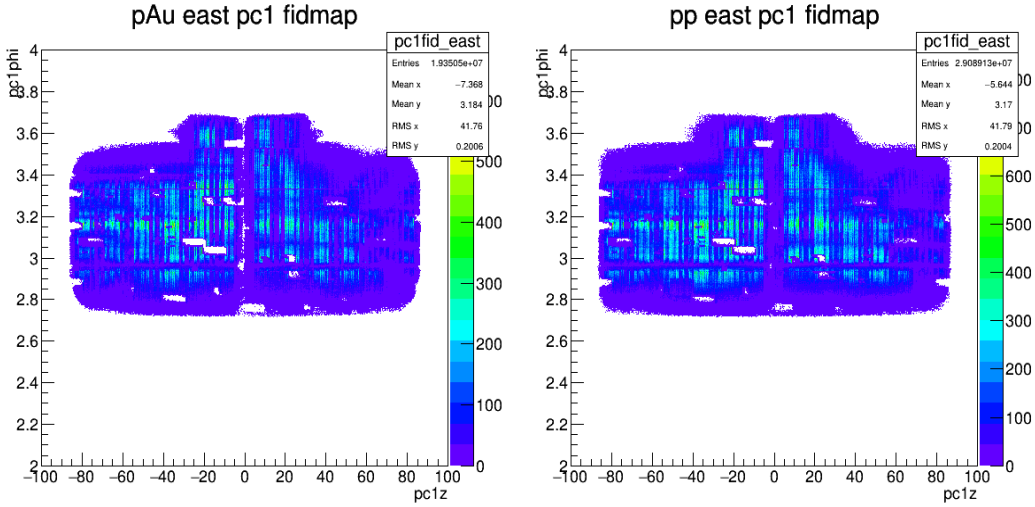

Figure 3.92: Fiducial map of PC1 for East arm in pp and pAu

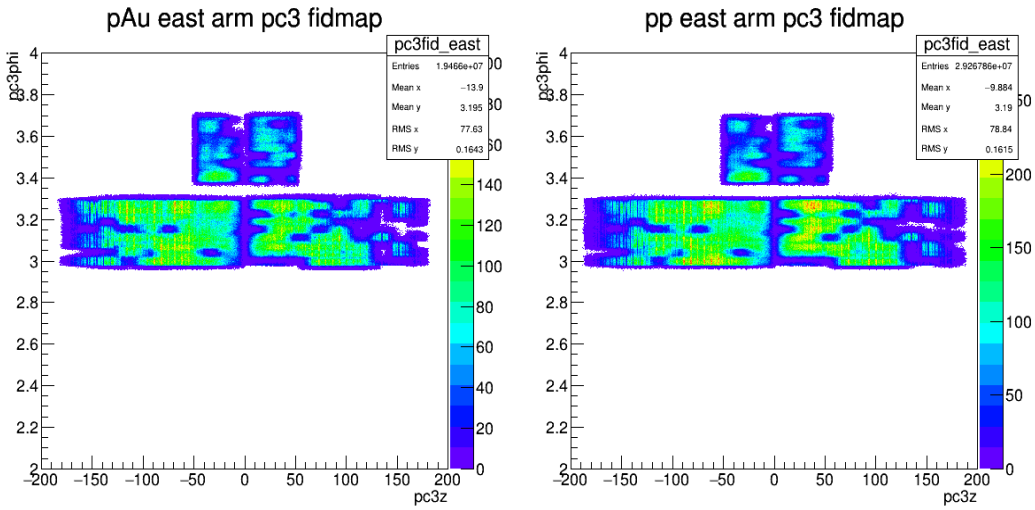

Figure 3.93: Fiducial map of PC3 for East arm in pp and pAu

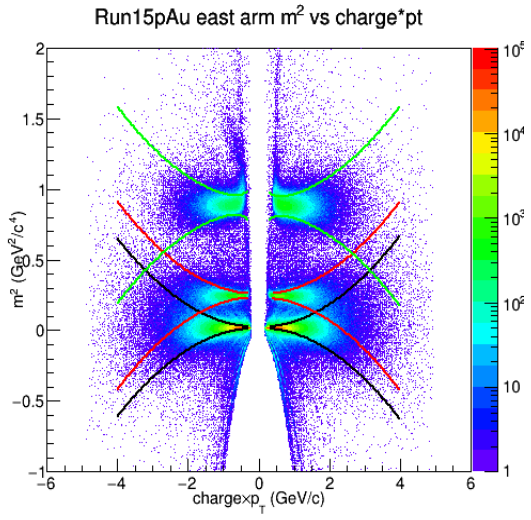

Figure 3.94: Mass-squared vs $p_T \times charge$ for Run15 pp.

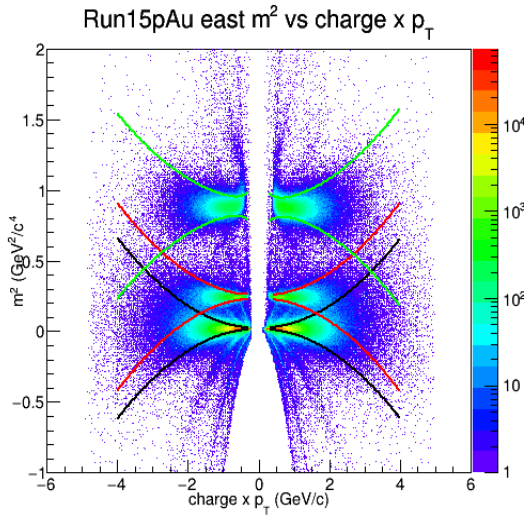

Figure 3.95: Mass-squared vs $p_T \times charge$ for Run15 pAu.

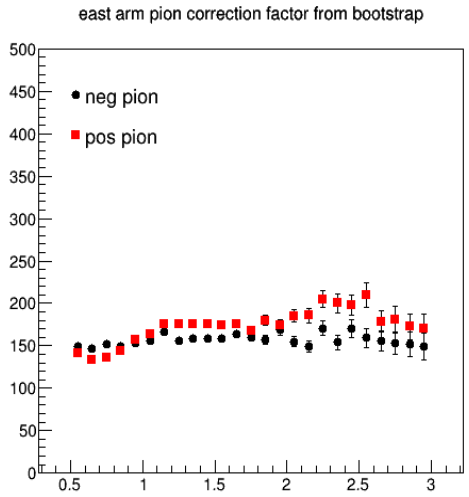

Figure 3.96: correction factors for pions

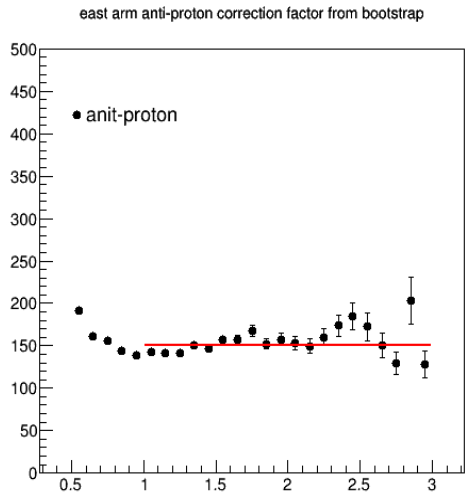

Figure 3.97: correction factor for protons

3.7.5 Correction Factors from Bootstrap and its Comparison with that Come From Simulation

Figure 3.96 and 3.97 shows the correction factors for pions and protons from pp bootstrap. When calculating the correction factors, we first measured the raw run15 pp yield, then we did the same calculation as we did for Run15 pAu data except we did not multiply the raw spectra by the correction factor. The detailed calculations we did are things such as: divide the raw by the number of events, scale the raw spectra by $1/2\pi$, and for each pt bin we divide them by dp_T and the middle p_T value of that bin and scale the spectra by the bias factors. We did this in order to get the correction factor so that we can apply this to the pAu spectra directly.

For the pion correction factor we see there is a slight increase as a function of p_T; this is because we did not use symmetric PID cuts pions, instead, we only count the pions for the lower part and then multiply the yields by a factor of two. This method is used to reduce the kaon contamination. We can also notice that the bootstrapped anti-proton spectra has a bump between 2-3 GeV, we think this bump is due to the lack of statistics, so we fit it with a straight line and use the fitted value instead.

We also plot the ratios of the correction factor obtained from bootstrap to that obtained from

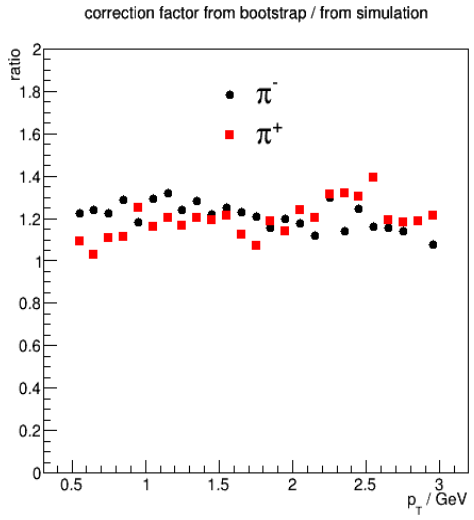

Figure 3.98: correction factors ratios for pions

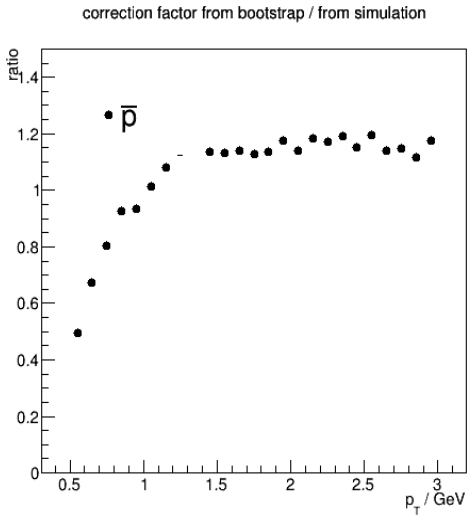

Figure 3.99: correction factor ratio for protons

simulation.

Figures 3.98 and 3.99 show the ratios of the correction factor from pp bootstrap and that from simulation. The correction factor obtained from simulation is around 20% lower than that obtained from bootstrap. Considering the detector is not at in a very good condition, we will use the bootstrapped pion efficiency for our data. For the anti-proton correction factor, we will use the pion correction factor, but we add a conversion factor that accounts for the Jacobian transformation from pseudorapidity to rapidity, which depends on the particle mass.

We know that the detector has a fixed acceptance in pseudorapidity η, which is the same for all particles, but we are reporting the yield measurements per unit of rapidity. So, when changing from pseudorapidity to rapidity, the factor for pions and protons are different, as shown in the following formula.

$$\frac{dN}{d\eta dp_T} = \sqrt{1 - \frac{m^2}{m_T^2 cosh^2 y}} \frac{dN}{dy dp_T} \tag{3.10}$$

The factor is mass dependent, which causes the detector acceptance is lower for protons than for pions. We plot the ratio of the factor for protons and pions, shown in figure 3.100. We can use the pion correction and the ratio to derive anti-proton correction factor.

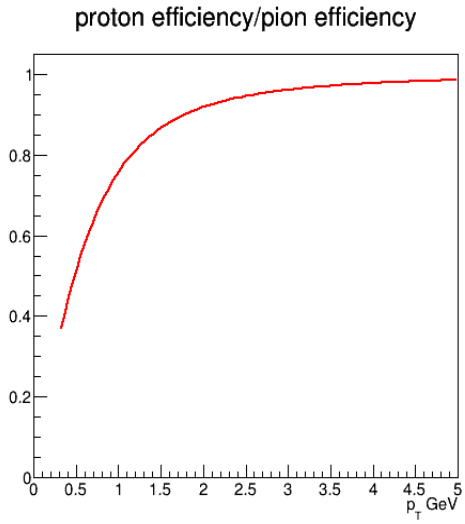

Figure 3.100: Proton efficiency over pion efficiency

3.8 Systematic Study

There are usually three types of systematic uncertainty: point to point uncorrelated; point to point correlated, which can change the shape of the spectra smoothly as a function of p_T; and global, which will only move the point up and down same amount. In PHENIX, we usually refer these as Type A, Type B and Type C systematic uncertainty.

The normal way of calculating systematic uncertainty introduced by the various cuts is by varying the cuts and examine the effects of the variation. The absolute value of the deviation from unity of the ratio can be used as a measure of systematic uncertainty of the cut. But since our correction factor comes from bootstrap, we need some special way to estimate the systematic uncertainty. Sources of systematic uncertainty comes from the previous pp result, run-to-run variations, timing calibration, pile-up study, particle selection and for protons, an additional source coming from the feeddown correction.

The total systematic uncertainties for Run5 pp spectra pion and negative pion is 7%.

3.8.1 Uncertainty from Track Selection

In our analysis, we used the PC3 and TOF 2σ track-matching cuts to remove background tracks. To see the systematic uncertainty introduced by the PC3 and TOF matching cuts, we changed the 2σ cut to 3σ cut and compared to the Gaussian ideal 2σ to 3σ ratio. Figure 3.101 and figure 3.102 shows the negative pion spectra ratio using PC3 2σ cut over 3σ cut in pp and pAu collisions separately. From the double ratio we assign around 4% systematic to the PC3 cut. Figures 3.103 and 3.104 shows the same thing for TOF cut. From the double ratio, we assign 3% systematic uncertainty to the TOF cut.

3.8.2 PID Band Selection in pp and pAu Collisions

In this section, we studied the uncertainty introduced by the particle identification band. When we make particle particle selection, we selected the tracks that are within 2 standard deviations of the mean, which should capture 95% of all the particles according to the Gaussian function. If we change that to be 3 standard deviation of the mean, we should capture 99% of all

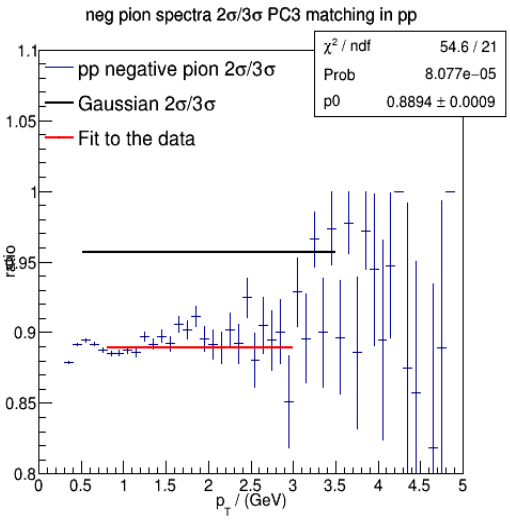

Figure 3.101: Negative pion spectra ratio using PC3 2σ over 3σ in Run15 p+p collisions

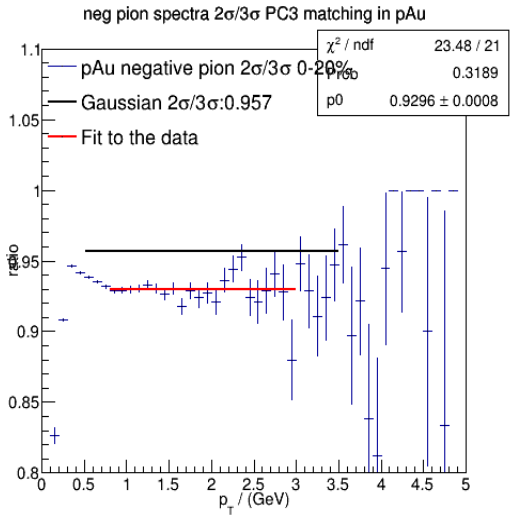

Figure 3.102: Negative pion spectra ratio using PC3 2σ over 3σ in Run15 p+Au collisions in 0-20% centrality bin

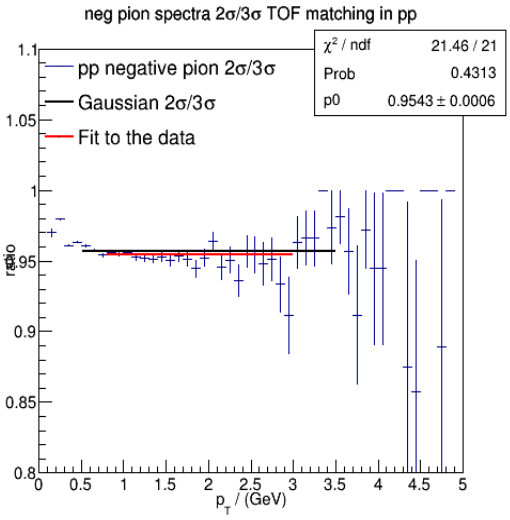

Figure 3.103: Negative pion spectra ratio using TOF 2σ over 3σ in Run15 p+p collisions

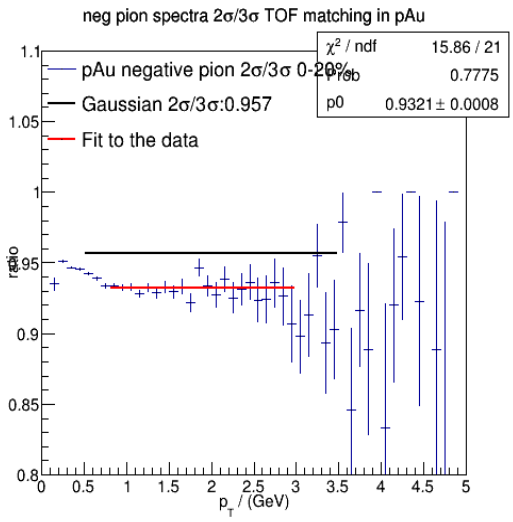

Figure 3.104: Negative pion spectra ratio using TOF 2σ over 3σ in Run15 p+Au collisions in 0-20% centrality bin

particles. We compare the spectra that are calculated using 2 σ and 3 σ; the ratio should be equal to 0.95/0.99, and we assign the difference to be systematic uncertainty.

Figure 3.105, 3.106 shows the spectra ratio in p+p collisions using 2σ and 3σ. We can see for pions, the ratio agrees almost perfectly with the Gaussian ratio. Figure 3.107 shows the spectra ratio for anti-proton with 1.5σ with that to 2σ, we can see this value also very close to the Gaussian ideal value. The reason we select different σ as that for pion spectra is we want to reduce the kaon contamination.

Figure 3.109, 3.110 and 3.111 shows the same result for Run15 p+Au collisions. We see a similar pattern as that in pp collisions. Considering the double ratio, we assign 1% systematic for the PID cut.

3.8.3 Run-by-run Variation in Run15 pAu Collisions

To compare the run-by-run variation, we first divide the spectra obtained from a single run number to that from all runs. Then, we fit the ratio to a single number. We choose 0.5 to 1.5 GeV as the fit range since this p_T range have more statics. An example fit is shown in Fig. 3.113; the value for this fit is 0.8919. We can get this value for each run and then we plot the fitted number as a function of the run numbers. The results for the spectra in 0-20% centrality selection are shown in Figs. 3.114 and 3.115, 3.116. Notice that we renamed the run numbers from 0, since this makes the x-axis more readable. We also separated the runs to be low luminosity runs and high luminosity runs. From these figures we noticed that for high luminosity runs, the ratios are lower than that for low luminosity runs.

For the pion spectra, the difference for most runs are within 10%, so we assign 10% systematic uncertainty due to the run-by-run variation.

3.8.4 Systematic Uncertainty from Timing Calibration

For calculating the systematic uncertainty caused by timing calibration, we will compare the spectra obtained by two different set of timing calibration; one version is done by me and the other one is done by Takahito Todoroki in PHENIX collaboration. Since this is a multi-step process

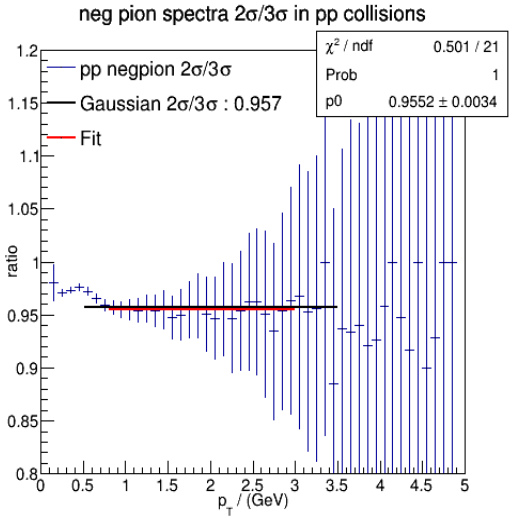

Figure 3.105: Negative pion spectra ratio using PID 2 σ over 3σ in Run15 p+p collisions

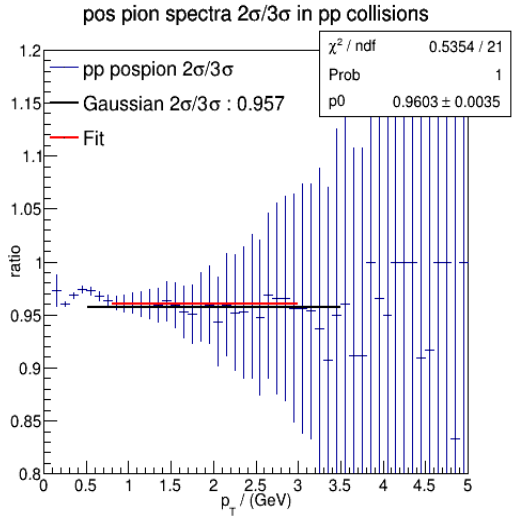

Figure 3.106: Positive pion spectra ratio using PID 2 σ over 3σ in Run15 p+p collisions

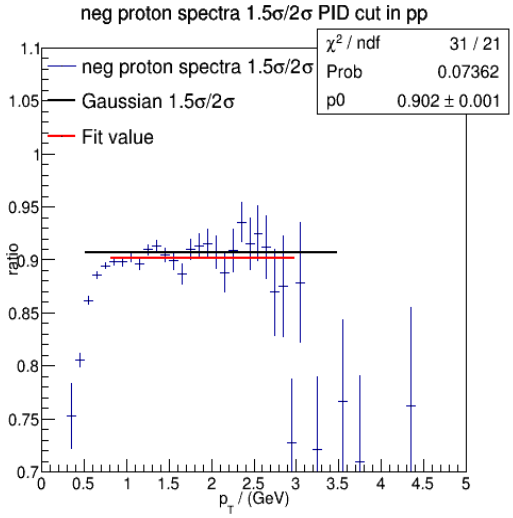

Figure 3.107: Anti-proton spectra ratio using PID 1.5 σ over 2σ in Run15 p+p collisions

Figure 3.108: Systematic uncertainly introduced by PID band in Run15 p+p collisions

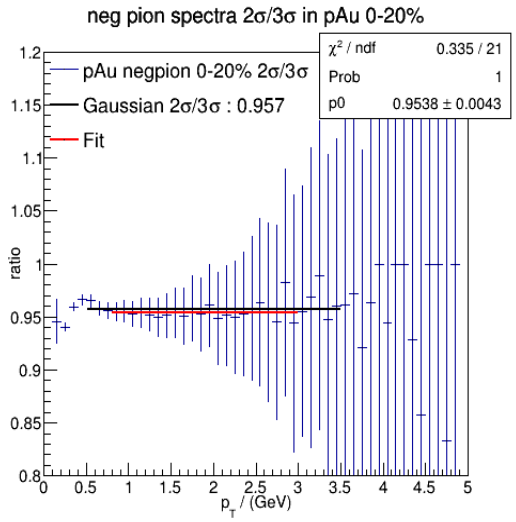

Figure 3.109: Negative pion spectra ratio using PID 2 σ over 3σ in Run15 p+Au 0-20% centrality collisions

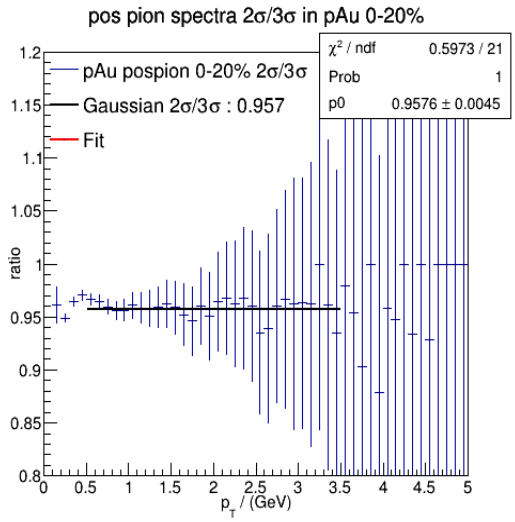

Figure 3.110: Positive pion spectra ratio using PID 2 σ over 3σ in Run15 p+Au 0-20% centrality collisions

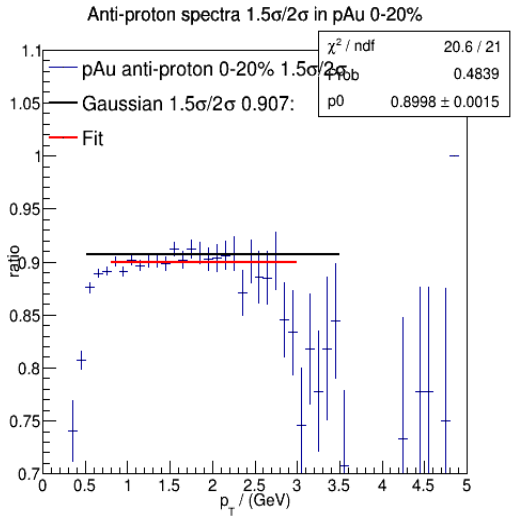

Figure 3.111: Anti-proton spectra ratio using PID 1.5 σ over 2σ in Run15 p+Au 0-20% centrality collisions

Figure 3.112: Systematic uncertainly introduced by PID band in Run15 p+Au collisions

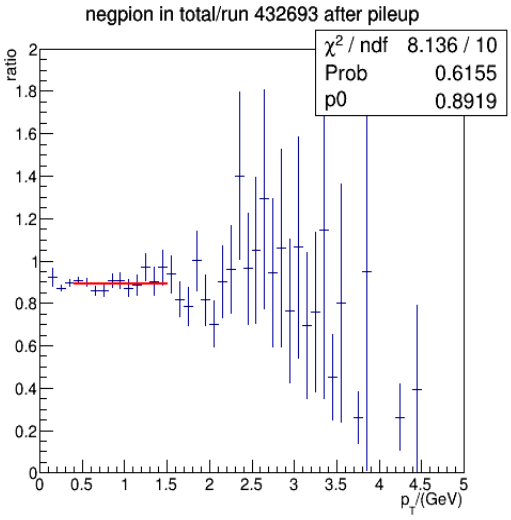

Figure 3.113: Negative pion spectra from run number 432693 divided by the that from all the runs.

involving slat-by-slat calibration and run-by-run calibration, the results may differ depending on the order and number of iterations that are applied. To compare our timing calibration, we summed up the offset in each step for each run and each slat number and compared the total offset. Figure 3.118 shows the comparison for run number 432637 with a subset of slat number for a better view. The black points is Todoroki's result and the red square is my result and we can see the offset is pretty close except for some points which I marked as bad slats and set the offset to 0.

I also compared the calculated mass square values from these two different sets of timing calibration. To have a clear comparison, I selected very narrow p_T range, 0.1 GeV. Figure 3.119 shows the comparison of mass square for p_T range between 1.4 GeV and 1.5 GeV. We can see they are very similar.

Finally, we compared the final spectra results from the two set of timing calibrations. Figure 3.120, 3.121 and 3.122 shows the ratio of negative pion from my local timing calibration to the one on the database for three different centrality bins: 0-5%, 0-20% and 20-40%. The red shows the ratio fitted with a constant value; the difference is around 3%, so we assign 3% systematic uncertainty to the timing calibration.

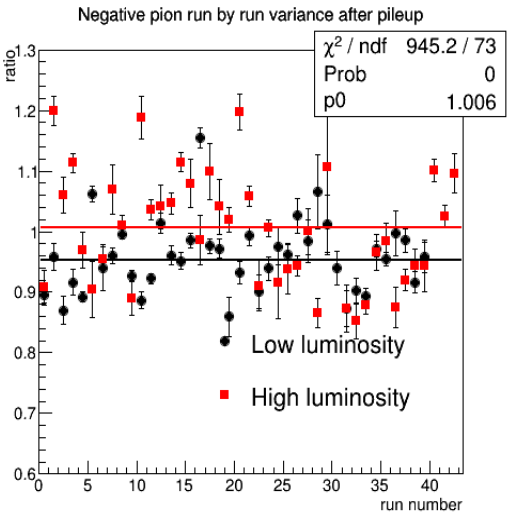

Figure 3.114: Negative pion run by run variation in Run15 pAu collisions

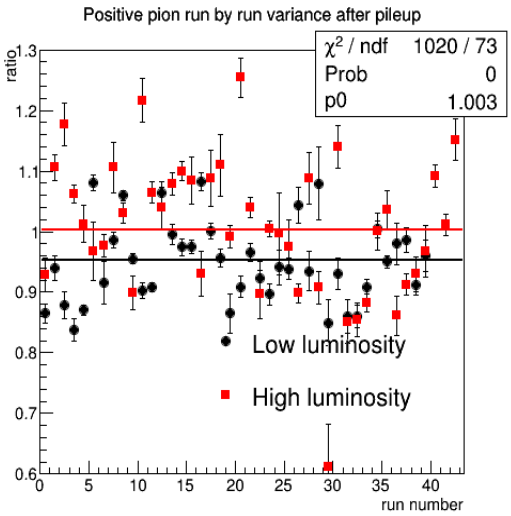

Figure 3.115: Positive pion run by run variation in Run15 pAu collisions

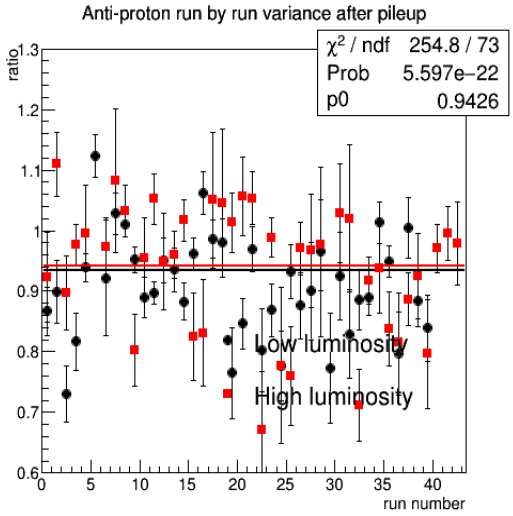

Figure 3.116: Anti-proton run by run variation in Run15 pAu collisions

Figure 3.117: Run by run variation of the pion and anti-proton spectra in Run15 pAu collisions at centrality 0-20%

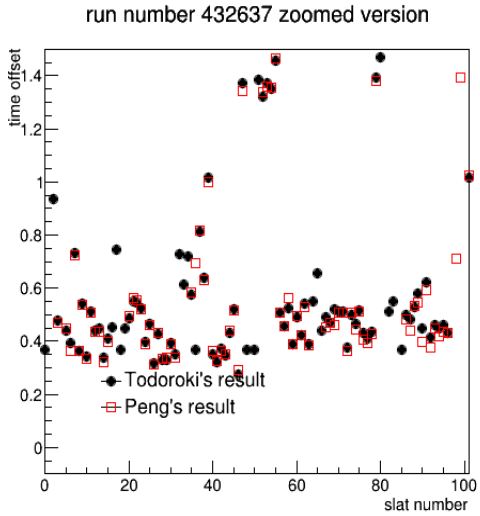

Figure 3.118: Comparison of two different timing calibration done by Takahito Todoroki and Weizhuang Peng

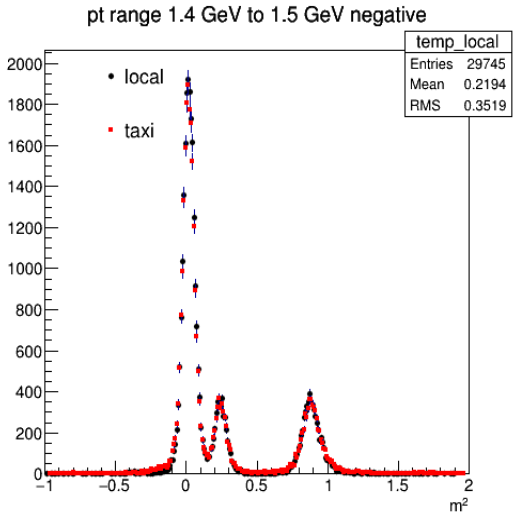

Figure 3.119: Mass square comparison from two timing calibrations for 1.4 GeV p_T < 1.5 GeV

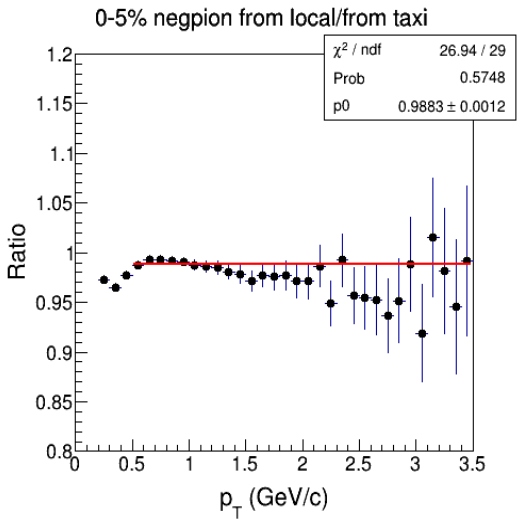

Figure 3.120: Ratio of 0-5% negative pion spectra got from two timing calibration

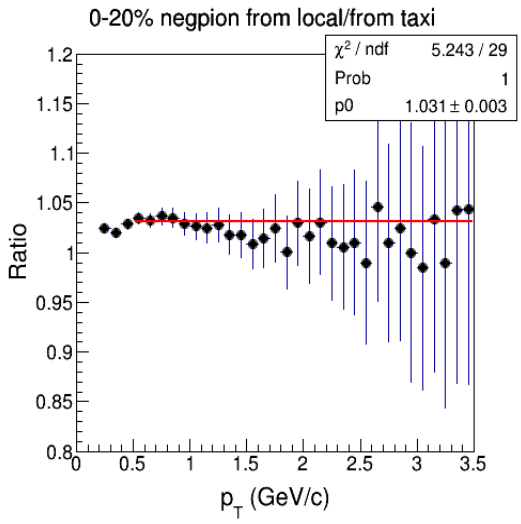

Figure 3.121: Ratio of 0-20% negative pion spectra got from two timing calibration

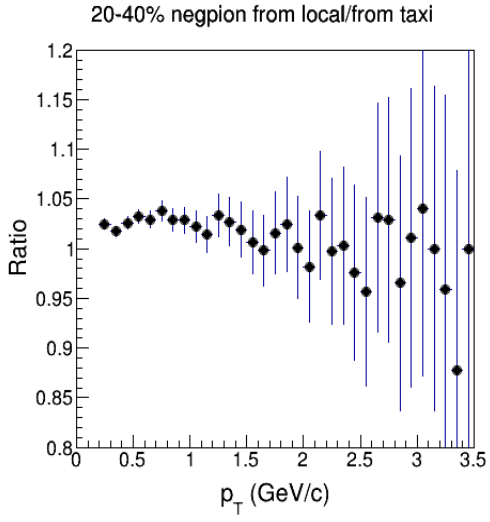

Figure 3.122: Ratio of 20-40% negative pion spectra got from two timing calibration

From these figures we can see there are around 3% differences between the two timing calibrations, which we can assign to systematic uncertainties.

3.8.5 Pile-up Study in pAu Collisions

In high luminosity environment, two collisions may occur during the same bunch crossing and be treated as one event by the detector; this is called pile-up. In central pAu collisions, 0-5% mainly, pile-up are observed to occur at an average rate of 8%. Qiao Xu at Vanderbilt University and Darren McGlinchey at Colorado University developed a method to filter out the pile-up events. The method used the hit time information recorded by the PMTs of Beam Beam Counter. The BBC is capable of recording the time that the particle travels from the vertex to the detector. In normal events, the timing distribution should be centered at some mean value and the width should be relative small. However, in pile up event there may be multiple peaks or at least the width should be wider. They defined a quantity called f which is equals to the number of PMTs which is within the mean time $\pm 0.5ns$ divided by the total number of PMTs fired. If this value is larger than 0.9, it is thought that the time measured by BBC is clustered and this event is not a pile-up event.

Our previous results did not implement the pile-up filter. And we would like to check the influence of applying the pile up filter and assign the difference as a systematic uncertainty.

Figure 3.123 shows the ratio of negative pion before and after pile up cut. It seems except for the most 0-5% event, applying the pile up cut did not have any influence on the final spectra result. In central events, after removing the pile up events, the spectra become higher around 5%; which means that some peripheral events are registered as central events but do not have as many tracks as central events. What we found is that even in the peripheral events, the total number of events removed by the pile up filter is also around 8%. However, removing these events did not really affect the spectra, maybe the reason for this is that in other centralities the number of tracks per event is not as high as that in 0-5% and the mis-classified pileup events have a similar number of tracks per event.

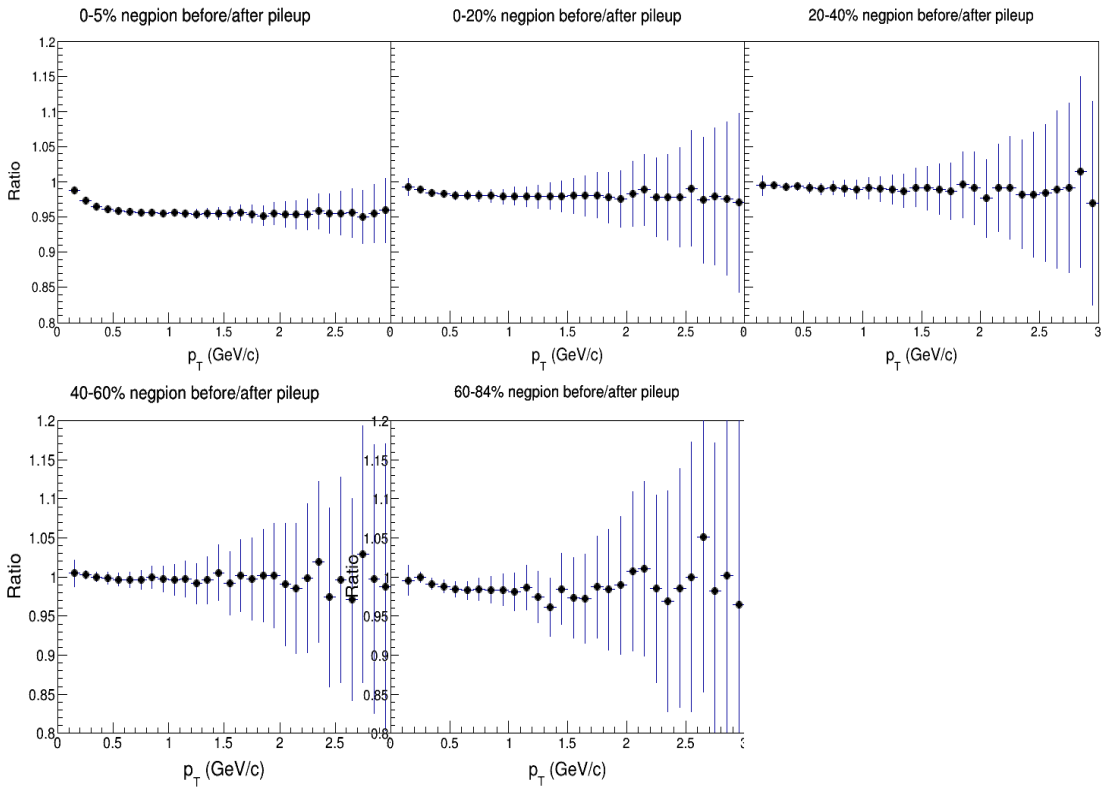

Figure 3.123: Ratio of negative pion before and after pile up cut for different centrality bins

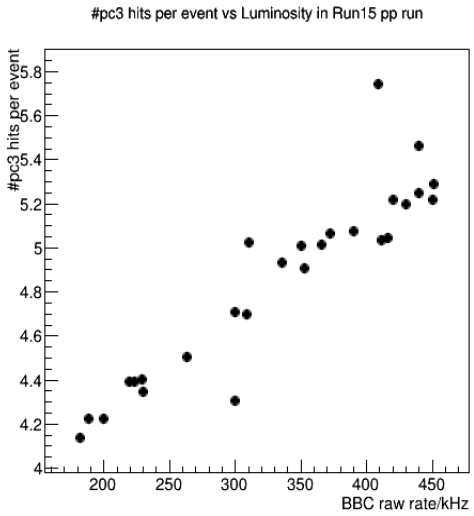

Figure 3.124: Number of PC3 hits per event vs luminosity in Run15 p+p runs

3.8.6 Pile-up Study in pp

We have applied the pile up filter in p+Au collisions, so we wondered how pile-up in p+p collisions would influence the results. So we did some study. Since there are no pile-up filter developed for p+p collisions, we did some simple research. Since the luminosity in Run15 p+p collisions is higher than that in Run5 p+p collisions our efficiency and acceptance corrections may not be accurate if there the pile-up effects are different in the different run period and collision systems. We want to see if there is a big difference in Run15 p+p collisions in low and high luminosity runs. First, we compared the number of PC3 hits per event in different runs with BBC raw rates ranging from 180 to 450, shown in figure 3.124. We see the number of PC3 hits basically increase linearly with the BBC raw rates, which is expected.

Then we compared the number of TOF hits per event as a function of the BBC raw rate, shown in figure 3.125. As expected, the number of TOF hits also increases with the BBC raw rate.

In the end, we selected runs that have at most 5% variation in the pion multiplicity, and assign this as an uncertainty - it should cover the effect of the double-interaction events.

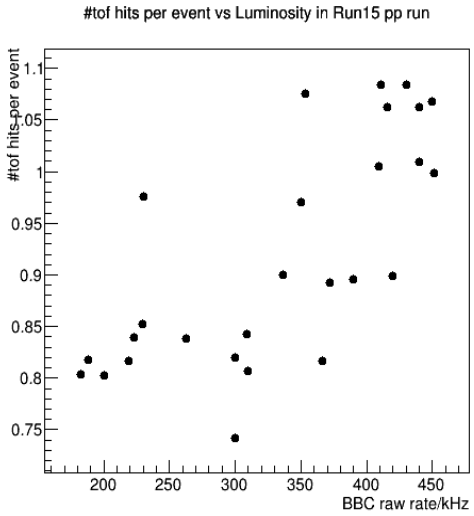

Figure 3.125: Number of TOF hits per event vs luminosity in Run15 p+p runs

3.8.7 Feed-down Systematic Uncertainty for $\bar{p}$

For the anti-proton, there is another source of uncertainty: the part that comes from the feed-down correction. The way we calculate the systematic uncertainty for feeddown fraction is by calculating the feeddown fraction using two method. We have mentioned the method before where we used the simulation anti-proton and anti-lambda as input to PISA and calculated the feeddown fraction. In this section, we will introduce another method to calculate the feeddown fraction ratio. The new method is data-driven, and we uses a DCA cut. Figures 3.126 and 3.127 shows the DCA2d distributions for decayed anti-protons and prompt anti-protons in simulation. We can see that the decayed anti-protons have a much wider DCA distribution. We implemented a p_T-dependent DCA2d cut, which removes about 70% of the decayed anti-protons in simulation, which is shown in table 3.4. We then apply the same cut in the data, assuming that it removes the same fraction of decayed anti-protons. Then we calculate the feeddown fraction using the following formula:

$$f = \frac{spectrum - spectrum_d cacut}{spectrum} \times \frac{1}{0.7} \tag{3.11}$$

The data-driven estimate of the feeddown fraction and its comparison to that calculated from

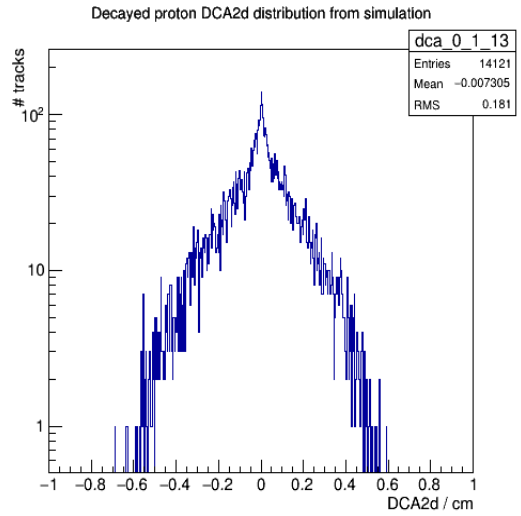

Figure 3.126: DCA2d distribution for the decayed anti-proton from anti-lambda input in simulation in pt range 1.3-1.4 GeV

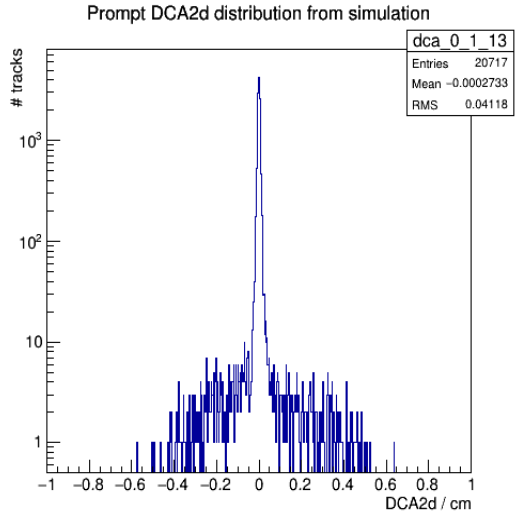

Figure 3.127: DCA2d distribution for the prompt anti-proton from anti-proton input in simulation in pt range 1.3-1.4 GeV

simulation is shown in Figs. 3.128 and 3.129. The black line shown in ig. 3.128 is the fitted line for the feeddown fraction obtained using the MC simulations. We can see that the difference in the feeddown fractions is around 10% at p_T < 2GeV, and 20% at higher p_T. We used the recalculated feeddown fraction to obtain the corrected anti-proton spectra and compare them to the nominal result; the ratio is shown in Fig. 3.130. The uncertainty in the final spectrum is smaller than the uncertainty in the feeddown fraction.

We also implemented another set of DCA2d cuts, which remove about 60% of the decayed anti-protons in simulation, and repeated the procedure described above. The corresponding results are shown in Figs. 3.131, 3.132, and 3.133.

From the above study, we assign 5% uncertainty from feeddown to the anti-proton spectra for p_T range below 2.0 GeV, and 10% above 2.0 GeV.

3.8.8 Summary of Systematic Uncertaities

So, the total systematic uncertainty for pions is 12%, and the total systematic uncertainty for antiprotons is 16%. A summary of the systematic uncertainties is shown in Table 3.5.

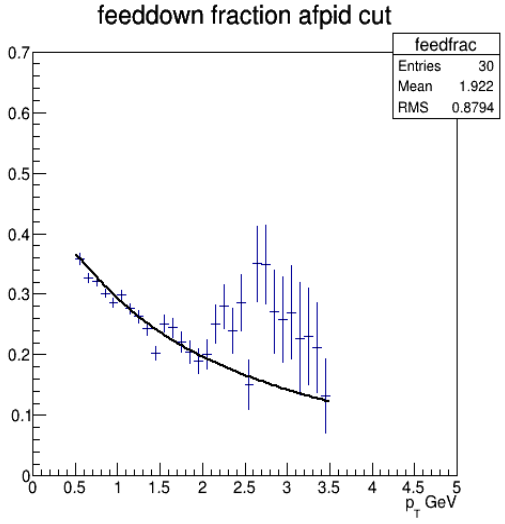

Figure 3.128: Feeddown fraction calculated using the DCA2d cut 1

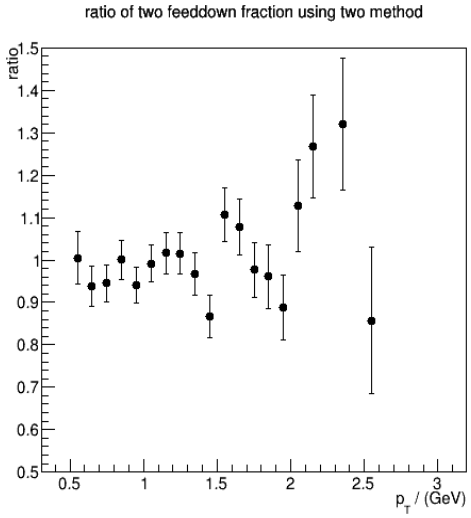

Figure 3.129: Feeddown fraction ratio to the one calculated using simulation

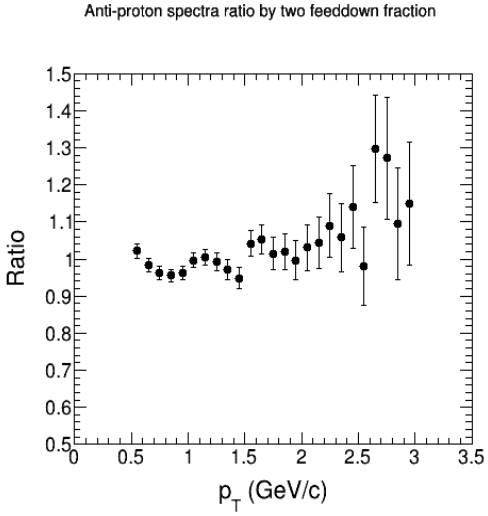

Figure 3.130: Anti-proton spectra ratio using two feeddown fraction

Table 3.4: p_T dependent DCA2d cut to remove decayed anti-protons

p_T range	cut around 70%	p_T range	cut around 60%
0-1 GeV	0.05	0-1 GeV	0.074
1.0-1.5 GeV	0.043	1.0-1.5 GeV	0.066
1.5-1.8 GeV	0.035	1.5-1.9 GeV	0.055
1.8-2.4 GeV	0.032	1.9-2.5 GeV	0.048
2.4-2.8 GeV	0.027	2.5-2.8 GeV	0.042
2.8-3.0 GeV	0.025	2.8-3.0 GeV	0.038

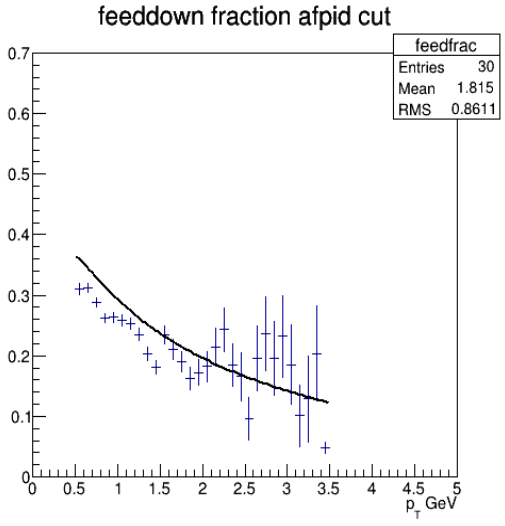

Figure 3.131: Feeddown fraction calculated using the DCA2d cut 1

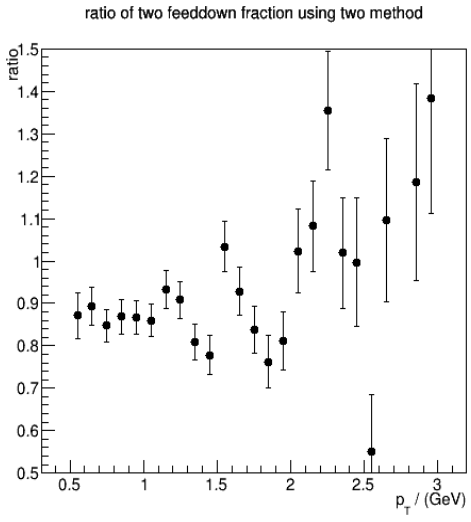

Figure 3.132: Feeddown fraction ratio to the one calculated using simulation

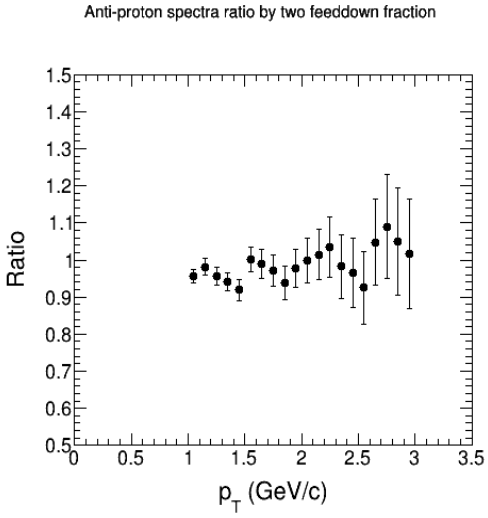

Figure 3.133: Anti-proton spectra ratio using two feeddown fraction

Table 3.5: Systematic uncertainties on the p_T spectra for $\sqrt{s_{NN}}$ = 200 GeV p+Au given in percent

Source	π^+	π^-	$\bar{p}$	Type
Track selection	5	5	5	B
Timing Calibration and PID	3	3	3	B
Efficiency correction based on pp results	7	7	7	B
Run by run variations in pAu	10	10	10	B
Run by run variations in pp	5	5	5	B
Feeddown anti-proton	-	-	5-10	B
Scale uncertainty in pp (from Run 5)	9.7	9.7	9.7	C
Bias factors	1-2	1-2	1-2	C
Total uncertainty for spectra	17	17	20	
Spectra ratio to minbias results	3	3	3	
Anti-proton/negpion pion ratio		7-11		
R_{pAu}	12	12	16	

In the derived quantities, many of the uncertainties cancel since they are present in both the denominator and numerator. For the $\pi-/\bar{p}$ ratios only the uncertainty from PID and feeddown corrections remain; for R_{pAu} the uncertainties that come from the bootstrapped efficiency cancel, but others remain.

Chapter 4

Results and Discussions

4.1 Identified Particle Elliptic Flow and Comparison with Theory Models

In collaboration with Qiao Xu, we measured the identified particle elliptic flow v_2 in pAu collisions and compared them with theory models. I provided the deector calibrations and particle identification, as well as some of the model calculations. In the hydro models, due to the common velocity field, we expect to see that in the measurement of v_2 as a function of p_T, pion and proton distributions to split since their mass is different. In the case when the v_2 does not originate from collective flow, but from other correlations such as particle produced in jets, such mass dependence is not necessarily expected.

Figure 4.1 shows the pion and proton v_2 in pAu, dAu and ^{3}HeAu collisions. We can see there is a mass splitting for pion and proton v_2 at low p_T and high p_T in all three systems. Also, the splitting is more obvious in dAu and ^{3}HeAu collision than pAu collisions. This is within expectation, since the QGP formed in pAu should be smaller in volume and shorter in duration than that formed in dAu and ^{3}HeAu collisions.

Figure 4.2 and 4.3 shows the identified particle v_2 in comparison with SONIC and AMPT model. From the comparison we see that the hydrodynamic model describes the mass splitting of v_2 very well at low p_T, but at high p_T it fails. Also, the hydrodynamic models also predicts the splitting is smaller in p+Au collisions, which is consistent with data. What is unexpected is that even in AMPT model, we can also see the mass splitting pattern of $v_2(p_T)$ even though it have not implemented the flow evolution. We conducted a series of calculations, where we turned on and off the scattering between the hadrons after the system hadronizes. It turns out that the mass splitting at low p_T in AMPT occurs in the later hadronic stage becuase the different hadrons have different hadronic interaction cross section. At high p_T AMPT describes correctly the split between baryons and mesons, becuase it forms hadrons via the quark recombination mechanism.

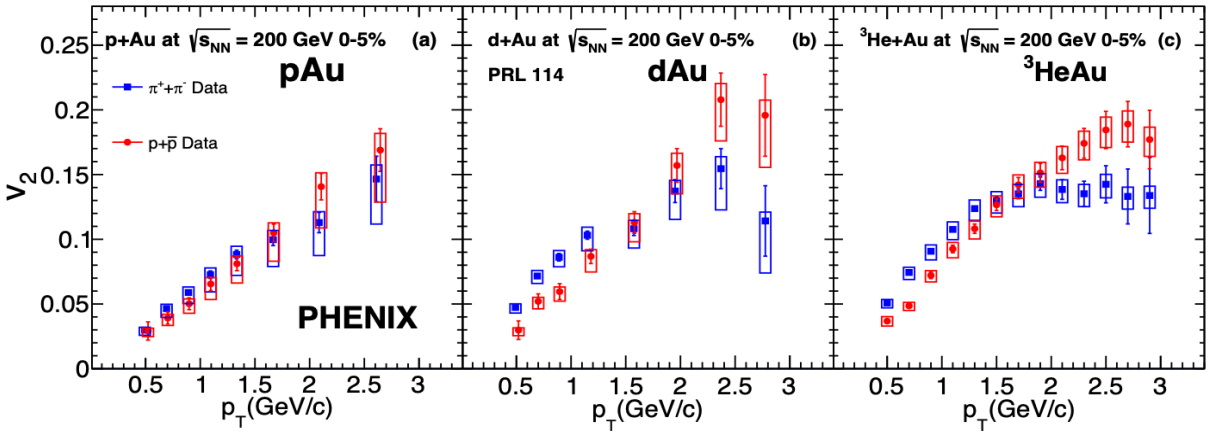

Figure 4.1: Identified particle v_2 in pAu, dAu and ^{3}HeAu collisions [12]

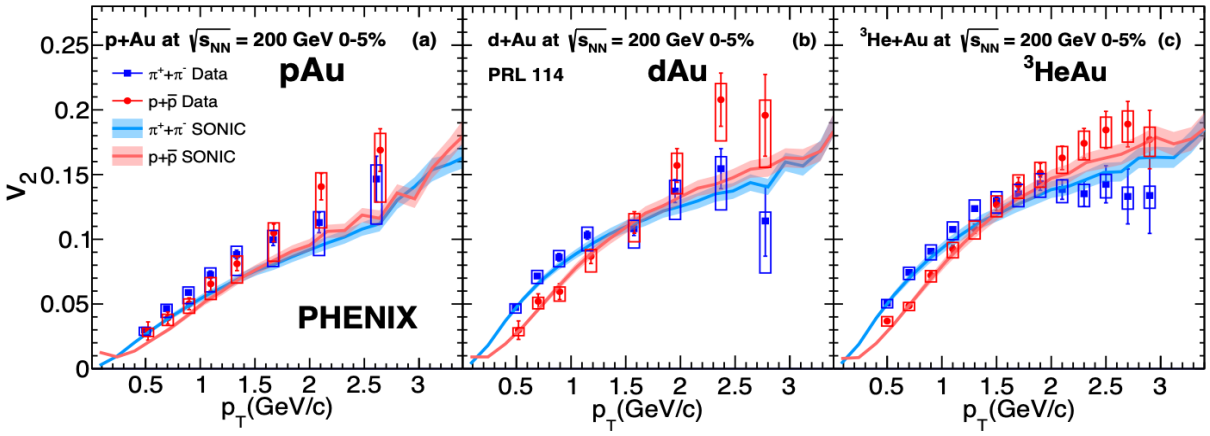

Figure 4.2: Identified particle v_2 in pAu, dAu and ^{3}HeAu collisions and results from a hydrodynamic model called SONIC [12]

The hydrodynamic models, which produce hadrons from the fluid do not capture this feature of the data.

From this we learned that at the early stage of the evolution of the medium, the medium may indeed flow like a fluid but at later stages as the temperature drops, the hydro models no longer work. And when the partons form into hadrons, recombination may play an important role in the process.

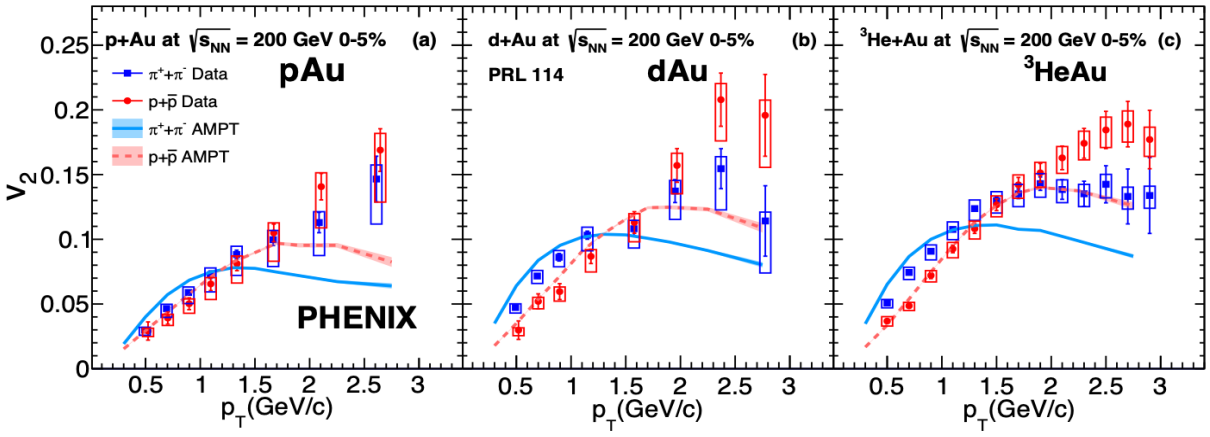

Figure 4.3: Identified particle v_2 in pAu, dAu and ^{3}HeAu collisions and results from a hydrodynamic model called AMPT [12]

4.2 Spectra for Pions and Anti-protons

Figure 4.4 shows the invariant yields of pions and anti-proton in different centrality bins as a function of transverse momentum. Different centrality bins are scaled by a different factor for better plotting, they are ordered by the number of binary collisions N_{coll}. From this plot we can see that the anti-proton spectra are more flattened at low p_T than pions. This is consistent with the predictions of thermal models due to the common velocity of flow. One thing to notice here is that the 0-5% spectra comes from the high-multiplicity trigger, which are designed for more central events, so this centrality has more statics than the other centrality bins, which can be seen in the particle ratio plots. We plot the pion and anti-proton spectra in a single plot for 0-5% centrality, shown in figure 4.5. In this figure, the different spectra shape of pion and proton can be seen more clearly.

Figure 4.6 shows the ratio of the yield in different centrality bins to the minimum bias trigger. From this figure we can see the yield in central bins increases as a function of p_T with respect to the minimum bias trigger, while the yield in peripheral bins decreases as a function of p_T. And in 20-40% centrality the ratio keeps constant as a function of p_T. Also, the centrality dependence for proton is much larger than that for pions.

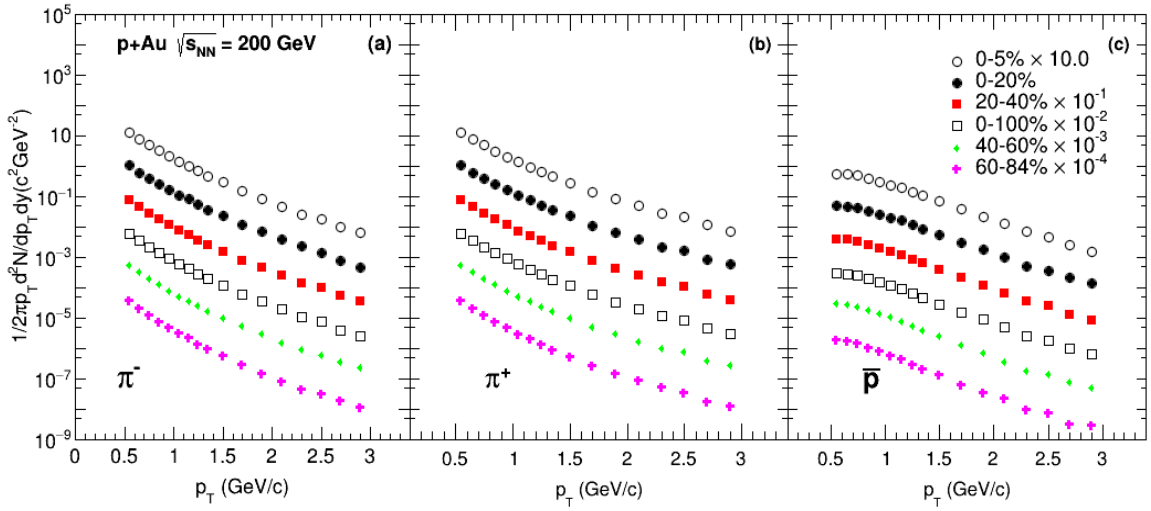

Figure 4.4: Invariant yield of $\pi^{\pm}$, $\bar{p}$ as a function of p_T in p + Au collisions. The yields are scaled by the arbitrary factors indicated in the legend, keeping collisions species grouped together.

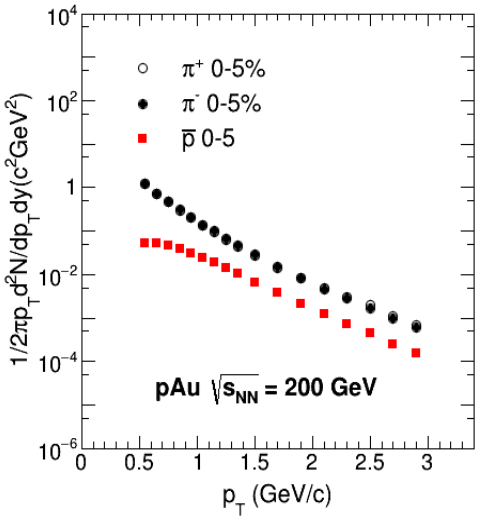

Figure 4.5: Invariant yield of $\pi^{\pm}$, $\bar{p}$ as a function of p_T in p + Au collisions for 0-5% centrality

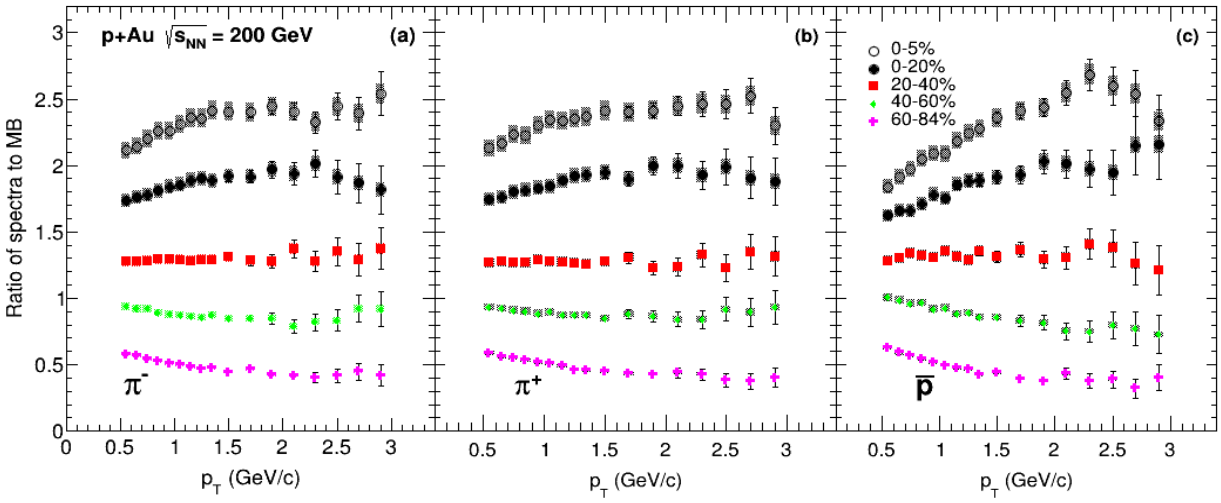

Figure 4.6: The ratio of invariant yield of $\pi^{\pm}$, $\bar{p}$ to minimum bias trigger for different centrality bins

4.3 Particle Ratio as a Function of Transverse Momentum

Shown in Fig. 4.7 is the ratio of the invariant yields of anti-protons to negative pions in six different centrality bins compared to the pp result. In AuAu collisions, this ratio is much larger than the pp result and has a strong centrality dependence, as shown in Fig. 4.8. This effect is attributed a combination of radial flow and parton recombination mechanism of hadronization, which produces enhancement in the baryon yield at intermediate p_T (between 2 and 5 GeV) [16]. Shown in Fig. 4.9 is the antiproton-to-pion ratio in d+Au collisions, compared to AuAu. The ratio in d+Au collisions is much smaller because this system has a much smaller N_{coll}. However,the result in the most central d+Au collisions is very similar to the result in the most peripheral bin in Au+Au. In p+Au collisions, we see similar pattern as seen in d+Au: there is a slightly centrality dependence and the ratio is slightly above the baseline p+p result.

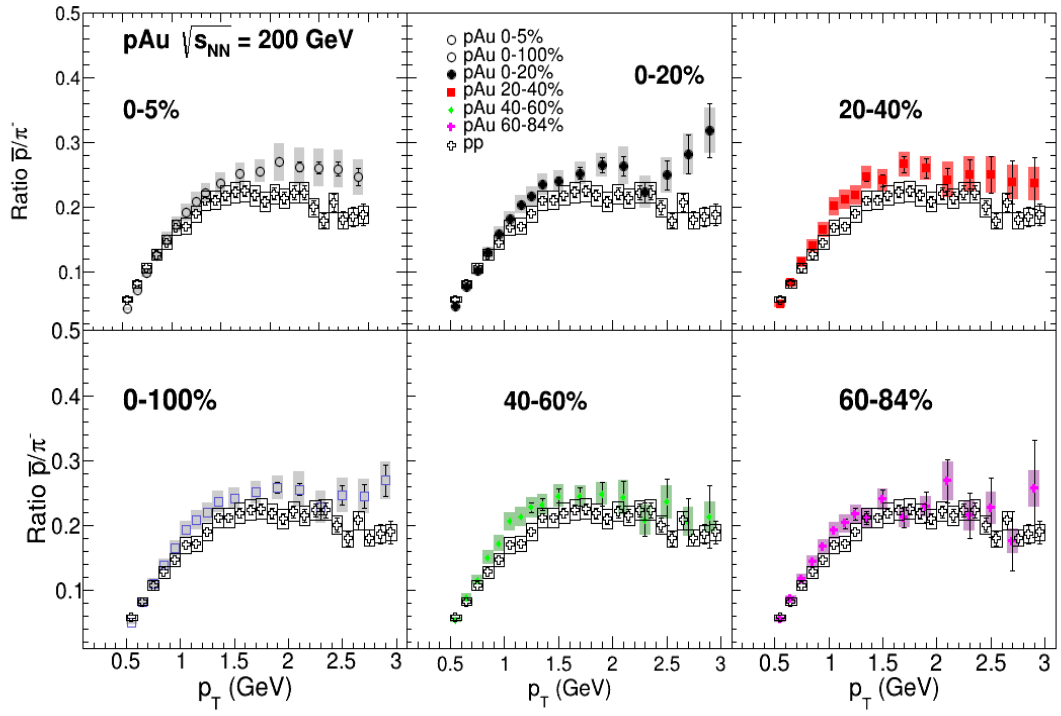

Figure 4.7: Ratios of invariant yields of $\bar{p}$ to $\pi^{\pm}$ as a function of p_T in p + Au collisions for different centrality bins

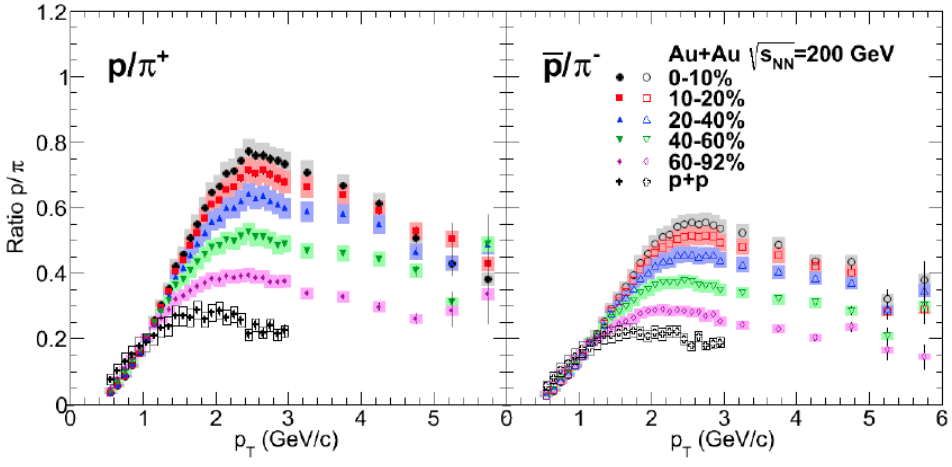

Figure 4.8: Ratios of invariant yields of proton to pion as a function of p_T in Au + Au collisions for different centrality bins [16]

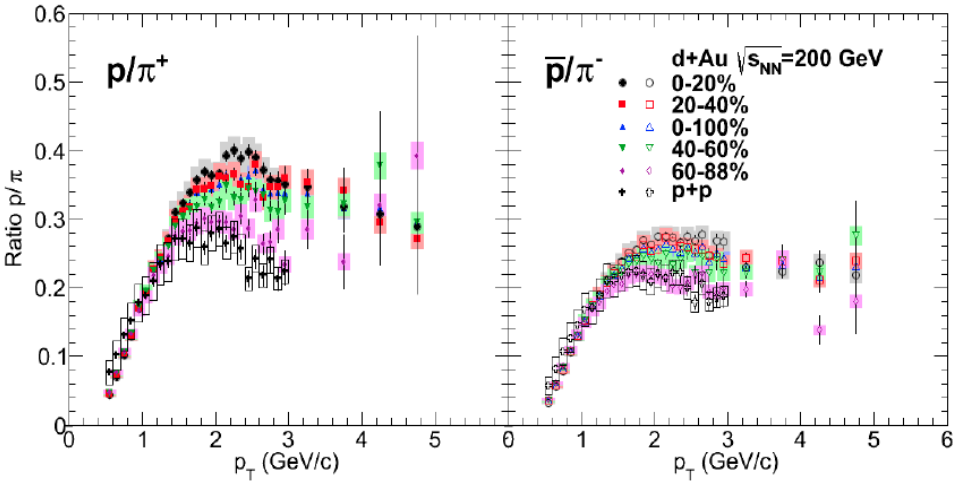

Figure 4.9: Ratios of invariant yields of proton to pion as a function of p_T in d + Au collisions for different centrality bins [16]

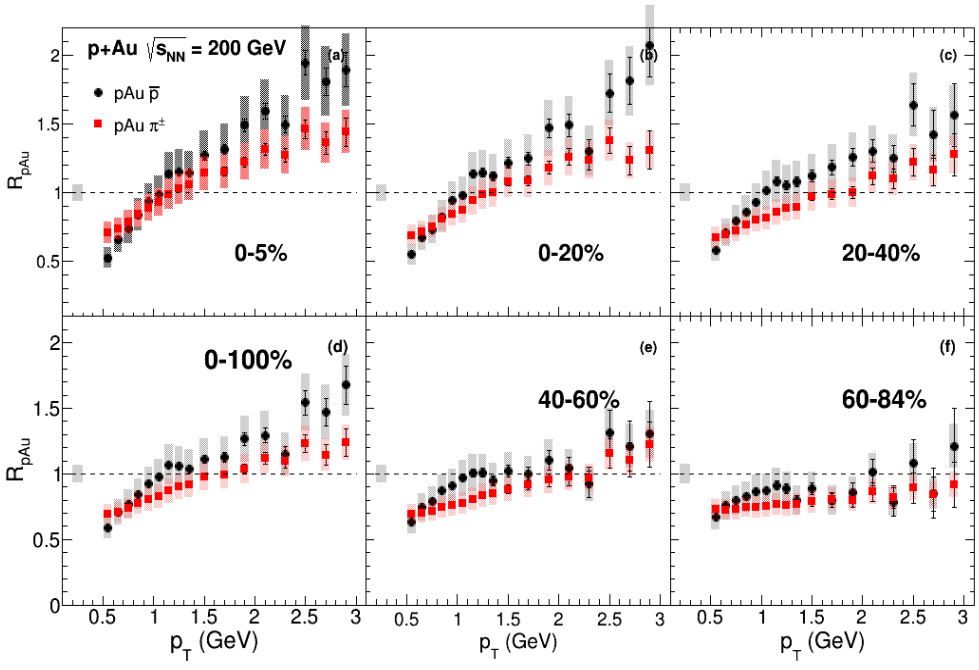

Figure 4.10: Nuclear modification factor as a function of p_T in different centrality bins in pAu collisions

4.4 Nuclear Modification Factor as a Function of Transverse Momentum

To measure the particle yield in pAu collisions compared to pp collisions we should consider the nuclear modification factor R_{pAu}, which are defined as the yield in pAu collisions divided by the yield in pp collisions, normalized by the number of binary collisions N_{coll} determined by Glauber Model. The following is shown as below:

$$R_{pAu} = \frac{Yield^{pAu}}{Yield^{pp} N_{coll}^{pAu}} \tag{4.1}$$

Figure 4.10 shows the nuclear modification factor of pions and anti-protons as a function of p_T. For central collisions, the ratio is above one for both pions and protons, which shows the effect of Cronin enhancement. And with the the centrality becoming more peripheral, this enhancement effect drops down and at the most peripheral centrality, it is almost negligible.

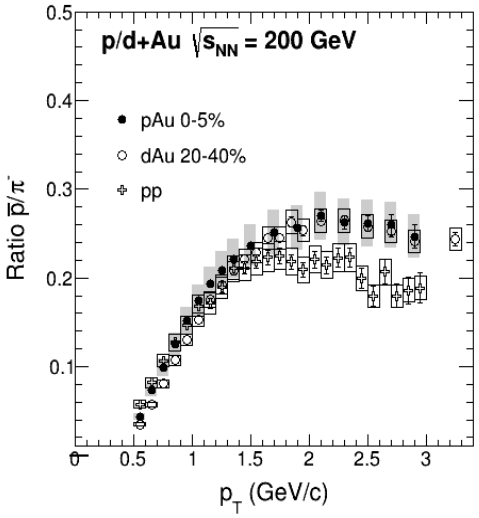

Figure 4.11: $\bar{p}/\pi^-$ ratio in p+Au 0-5% and d+Au 20-40% [16]

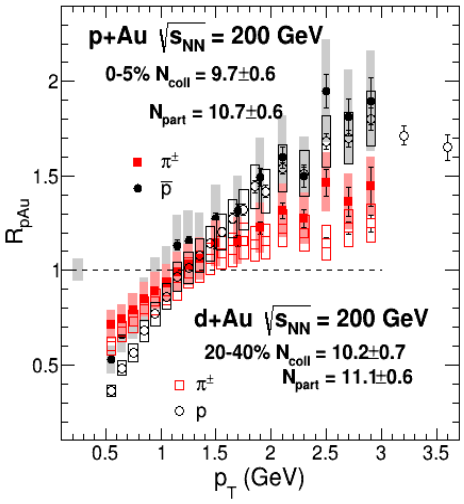

Figure 4.12: $R_{p/d+Au}$ in p+Au 0-5% and d+Au 20-40% [16]

4.5 Comparison to dAu Collisions

Since pAu collisions and dAu collisions are very similar, we want to see how the spectra results differ in these two collisions systems. We choose 0-5% centrality in p+Au collisions and 20-40% centrality in d+Au collisions since they have similar N_{coll} and N_{part}. The N_{coll} and N_{part} in 0-5% pAu collisions are 9.7±0.6 and 10.7±0.6, in 20-40% d+Au collisions are 10.2±0.7 and 11.1±0.6; which are pretty similar. Figure 4.11 and 4.12 shows the comparison of anti-proton pion ratio and nuclear modification factor in p+Au and d+Au collisions. Both the anti-proton to pion ratio and the nuclear modification factor overlap with each other for pAu measurements and dAu measurements. This is within expectations since pAu and dAu collisions are very similar with each other and if they have same number of binary collisions they should have very similar results.

4.6 Comparison to Theory Models

In this section, we will compare our results to some hydrodynamics models, basically the SONIC model [33] and superSONIC model [41], also the hadron transport model: A Multi-Phase Transport Model [34], which does not implement the hydrodynamics at the early times

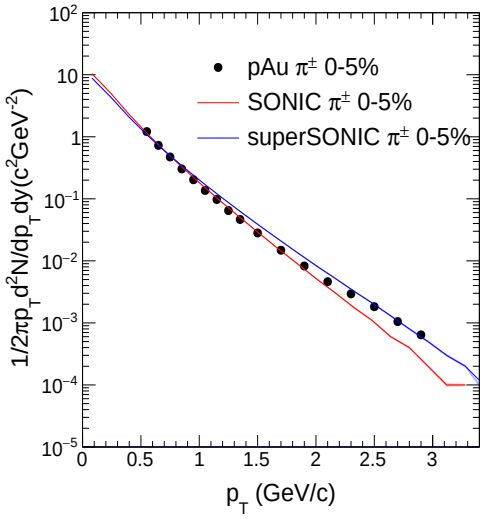

Figure 4.13: Invariant yield of pions in pAu collisions at $\sqrt{s_{NN}}$ = 200 GeV in comparison with SONIC and superSONIC model

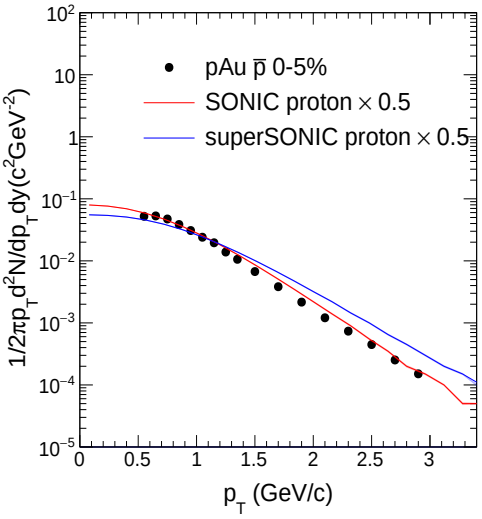

Figure 4.14: Invariant yield of anti-proton in pAu collisions at $\sqrt{s_{NN}}$ = 200 GeV in comparison with SONIC and superSONIC model

of the collision. The superSONIC model is a super-hybrid model that combines pre-equilibrium dynamics with viscous fluid dynamic evolution and late-stage hadronic rescatterings.

Figure 4.13 and figure 4.14 shows the comparison of pion and anti-proton spectra from data and SONIC, superSONIC model. One thing to notice here is that the proton spectra from the model is scaled by a factor of 0.5, which is due to the reason the correctly implementing proton annihilation in the hadron cascade is not solved yet and the best way is to scale it down by a factor of 2. We can see from this figures that the shape of the spectra between model and data agrees pretty well, the yield starts to diverge at high p_T. The fact that hydro models describe the data well at low p_T but fails at high p_T may indicate that an hot dense liquid (QGP) is formed during the collision and as the ball expands the temperature drops and hydro models no longer work. This can also be seen at the anti-proton over negative pion ratio shown in figure 4.15. From this figure we see the data and model agrees at p_T below 1.5 GeV and have a big difference above that.

Figure 4.16 and 4.17 shows the comparison of pion and proton spectra from 0-5% between the AMPT model. From these figures we see the model is not very good at predicting the yield of

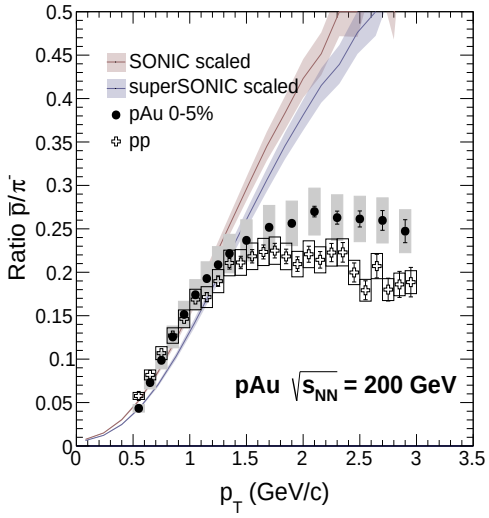

Figure 4.15: Ratio of invariant yield of anti-proton to negative pion in pAu collisions at $\sqrt{s_{NN}}$ = 200 GeV in comparison with SONIC and superSONIC model

the particles. One thing to notice is for the proton spectra, the flattening of the spectra at low p_T is not predicted by the AMPT model, which is a signature of the formation of a fluid. However, as seen in figure 4.18, the proton over pion ratio shows some similarity to the data. The AMPT model captures the trend of the ratio, that is the ratio increases from low to mid p_T, and then decreases from mid to high p_T. This is mainly due to the implementation of hadronazation by recombination in the AMPT model, which is missing in the SONIC and superSONIC models. The success of AMPT capturing the trend of the proton pion ratio may indicate that when quarks are formed into hadrons, recombination model is a very import mechanism that governs the formation of hadrons, at least at mid p_T region.

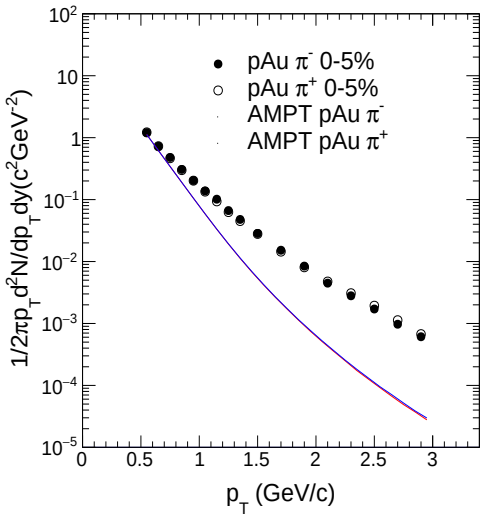

Figure 4.16: Invariant yield of pions in pAu collisions at $\sqrt{s_{NN}}$ = 200 GeV in comparison with AMPT model

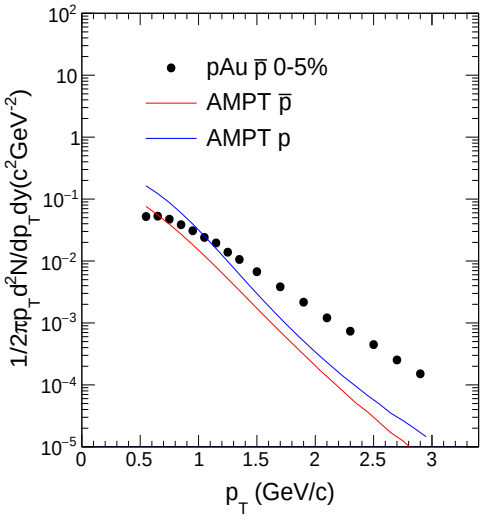

Figure 4.17: Invariant yield of anti-proton in pAu collisions at $\sqrt{s_{NN}}$ = 200 GeV in comparison with AMPT model

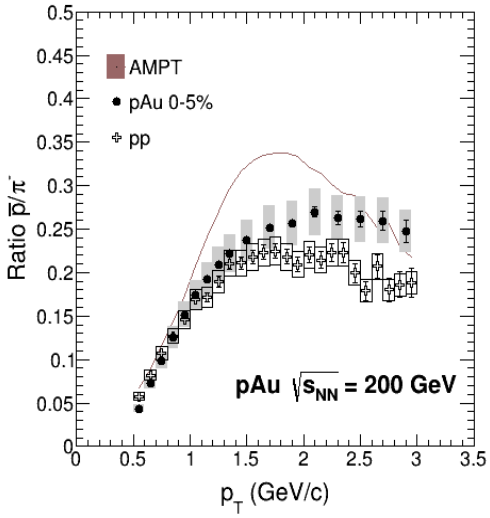

Figure 4.18: Ratio of invariant yield of anti-proton to negative pion in pAu collisions at $\sqrt{s_{NN}}$ = 200 GeV in comparison with AMPT model

Chapter 5

Conclusion and Future Work

5.1 Conclusion

We have measured the identified particle elliptic flow and the invariant yield of pions and anti-protons in pAu collisions at $\sqrt{s_{NN}}$ = 200 GeV. The results were compared with hydrodynamic models (SONIC and SuperSONIC) and a parton transport model (AMPT). We find that the hydrodynamic models provide a good description of the data at low p_T (below 1.5 GeV/c) where the dominant hadron production mechanism is through soft interactions. The hydrodynamics predictions deviate from that data at higher p_T, over-predicting the anti-proton to pion ratio and failing to capture the particle species dependence in the elliptic flow. These trends are well described by the AMPT model, which predicts the mass-splitting in the elliptic flow and the shape of the anti-proton to pion ratio, although it does not describe correctly the absolute values of $v_2(p_T)$ or the invariant yields. We find that hadron formation via quark recombination, as implemented in AMPT, is important for describing the particle species dependence in the yield ratios and elliptic flow. The success of hydrodynamics models may indicate the formation of QGP at the early times of the collision, which give more evidence for the formation of QGP in small systems.

5.2 Future Work

The motivation for this thesis work was to provide data from multiple observables in order to test the hypothesis of QGP formation in small systems. With the measurements of elliptic flow and identified particle spectra, we now have flow data in p+Au, d+Au, and ^{3}He+Au collisions at $\sqrt{s_{NN}}$ = 200 GeV, and data on identified particle spectra and nuclear modification factors in p+Au, and d+Au collisions in several centrality selections. It is possible to compare different collision systems in event classes that have similar average number of participating nucleons and binary nucleon-nucleon collisions. A Bayesian analysis of data from Au+Au collisions and these three small systems following Ref. [10] would be useful to understand the underlying physics

processes. If the small systems and large systems can be described by the same set of parameters simultaneously, this may indicate that the flow behavior in small systems and large systems has the same origin, which will give more evidence that QGP can also be formed in small systems.

REFERENCES

[1]Wikipedia. Standard Model Wikipedia. *Wikipedia*, 2020.

[2]Aprahamian et al. Reaching for the horizon: The 2015 long range plan for nuclear science. Oct 2015.

[3]Tapan K Nayak. Heavy ions: Results from the Large Hadron Collider. *Springer*, 79, Oct 2012.

[4]K. Adocx et al. Suppression of Hadrons with Large Transverse Momentum in Central Au+Au Collisions at $\sqrt{s_{NN}}$ = 130 GeV. *Phys. Rev. Lett.*, 88, Dec 2001.

[5]S. S. Adler et al. Identified charge particle spectra and yields in Au+Au Collisions at $\sqrt{s_{NN}}$ = 200 GeV. *Phys. Rev. C.*, 69, Mar 2004.

[6]J. Adams et al. Particle-Type Dependence of Azimuthal Anisotropy and Nuclear Modification of Particle Production in Au + Au Collisions at $\sqrt{s_{NN}}$ = 200 GeV. *Phys. Rev. Lett.*, 92, Feb 2004.

[7]Scomparin E. Armesto, N. Heavy-ion collisions at the Large Hadron Collider: A review of the results from Run 1. *Eur. Phys. J. Plus*, Mar 2016.

[8]S. Chatrchyan et al. Observation of long-range, near-side angular correlations in pPb collisions at the LHC. *Phys. Lett. B*, 718, Jan 2013.

[9]A. Adare et al. Quadrupole Anisotropy in Dihadron Azimuthal Correlations in Central d+Au Collisions at $\sqrt{s_{NN}}$ = 200 GeV. *Phys. Rev. Lett.*, 111, Nov 2013.

[10]J. Scott Moreland et al. Bayesian calibration of a hybrid nuclear collision model using p-Pb and Pb-Pb data at energies available at the CERN Large Hadron Collider. *Phys. Rev. C.*, 101, Feb 2020.

[11]H. Hahn et al. The RHIC design overview. *Nucl. Instrum. Meth. A*, 499, Sep 2003.

[12]Qiao Xu. Observation of Collective Behavior in High-Multiplicity Proton-Gold Collisions with PHENIX at RHIC. *Ph.D. thesis, Vanderbilt University*, Mar 2018.

[13]M. Allen et al. PHENIX inner detectors. *Nucl. Instrum. Meth. A*, 549, Sep 2003.

[14]Sergey Butsyk. PHENIX Drift Chamber operation principles. *PHENIX Collaboration, Focus seminar*, Jan 2003.

[15]H. Masui. PHENIX Focus Time of Flight. *PHENIX Collaboration, Focus seminar*, Jan 2003.

[16]Ronald John Belmont. Measurement of Identified Hadrons in AuAu and dAu Collisions at $\sqrt{s_{NN}}$ = 200 GeV. *Ph.D. thesis, Vanderbilt University*, Dec 2012.

[17]Webmaster Illustrator. The Physics Hypertextbook. *The Physics Hypertextbook*, Oct 2020.

[18]R. L. Mills C. N. Yang. Conservation of Isotopic Spin and Isotopic Gauge Invariance. *Phys. Rev.*, 96, Oct 1954.

[19]Sheldon L. Glashow. Partial-symmetries of weak interactions. *Nuclear Physics*, 22, Feb 1961.

[20]Steven Weinberg. A Model of Leptons. *Phys. Rev. Lett.*, 19, Nov 1967.

[21]Wilke van der Schee Wit Busza, Krishna Rajagopal. Heavy Ion Collisions: The Big Picture and the Big Questions. *Annual Reviews*, 68, Oct 2018.

[22]C. Aidala et al. Creation of quark-gluon plasma droplets with three distinct geometries. *Nature Physics*, 15, Dec 2019.

[23]O. Philipsen E. Laermann. Lattice QCD at Finite Temperature. *Annual Review of Nuclear and Particle Science*, 53, Dec 2003.

[24]K. Adcox et al. Formation of dense partonic matter in relativistic nucleus-nucleus collisions at RHIC: Experimental evaluation by the PHENIX collaboration. *Nucl. Phys. A*, 757:184–283, 2005.

[25]Collective Flow and Viscosity in Relativistic Heavy-Ion Collisions, author = Ulrich Heinz, Raimond Snellings. *Annual Review of Nuclear and Particle Science*, 63, Oct 2013.

[26]Matgorzata Anna Janik Panagiota Foka. An overview of experimental results from ultra-relativistic heavy-ion collisions at the CERN LHC: Hard probes. *Reviews in Physics*, 1, Nov 2016.

[27]Jean-Yves Ollitrault. Anisotropy as a signature of transverse collective flow. *Phys. Rev. D.*, 46, July 1992.

[28]Betty Abelev et al. Long-range angular correlations on the near and away side in p–Pb collisions at $\sqrt{s_{NN}}$ = 5.02 TeV. *Phys. Lett. B*, 719, Feb 2013.

[29]G. Aad et al. Observation of Associated Near-Side and Away-Side Long-Range Correlations in $\sqrt{s_{NN}}$ = 5.02 TeV Proton-Lead Collisions with the ATLAS Detector. *Phys. Rev. Lett.*, 110, May 2013.

[30]C. Aidala and others. Measurement of long-range angular correlations and azimuthal anisotropies in high-multiplicity p+Au collisions at $\sqrt{s_{NN}}$ = 200 GeV. *Phys. Rev. C.*, 95, Mar 2017.

[31]A. Adare et al. Measurement of Elliptic and Triangular Flow in High-Multiplicity ^{3}He+Au Collisions at $\sqrt{s_{NN}}$ = 200 GeV. *Phys. Rev. Lett.*, 115, Oct 2015.

[32]A. Adare et al. Measurement of Long-Range Angular Correlation and Quadrupole Anisotropy of Pions and (Anti)Protons in Central d+Au Collisions at $\sqrt{s_{NN}}$ = 200 GeV. *Phys. Rev. Lett.*, 114, May 2015.

[33]Paul Romatschke. Particle spectra and HBT radii for simulated central nuclear collisions of C+C, Al+Al, Cu+Cu, Au+Au, and Pb+Pb from $\sqrt{s_{NN}}$=62.4-2760 GeV. *Eur.Phys.J.C*, Feb 2015.

[34]Zi-Wei Lin et al. Multiphase transport model for relativistic heavy ion collisions. *Phys. Rev. C*, 72, Dec 2005.

[35]J. Novak et al. Determining fundamental properties of matter created in ultrarelativistic heavy-ion collisions. *Phys. Rev. C.*, 46, Mar 2014.

[36]Scott Pratt and Giorgio Torrieri. Coupling Relativistic Viscous Hydrodynamics to Boltzmann Descriptions. *Phys. Rev. C.*, 82, Oct 2010.

[37]K. Adcox et al. Formation of dense partonic matter in relativistic nucleus-nucleus collisions at RHIC: Experimental evaluation by the PHENIX Collaboration. *Nucl. Phys. A*, 757, Aug 2005.

[38]R.M. Yamamoto et al. The PHENIX detector magnet subsystem. *IEEE Transactions on Magnetics*, 32, July 1996.

[39]K. Adcox et al. PHENIX central arm tracking detectors. *Nucl. Instrum. Meth. A*, 499, Sep 2003.

[40]Brian Love. The Design, Implementation and Performance of the PHENIX Time-of-Flight West Detector. *M.S. thesis, Vanderbilt University*, May 2009.

[41]Paul Romatschke. Light-Heavy Ion Collisions: A window into pre-equilibrium QCD dynamics? *Eur.Phys.J.C*, Feb 2015.